UNIVERSIDAD COMPLUTENSE DE MADRID
FACULTAD DE CIENCIAS MATEMÁTICAS

TESIS DOCTORAL

Mathematical modeling of cognitive processes with applications in neuroscience and robotics

Modelización matemática de procesos cognitivos con aplicaciones en neurociencia y robótica

MEMORIA PARA OPTAR AL GRADO DE DOCTOR

PRESENTADA POR

Carlos Calvo Tapia

Directora

Valeriy Makarov Slizneva

Madrid

PhD Program in Mathematical Engineering, Statistics, and Operations Research

Universidad
Complutense de Madrid

Universidad
Politécnica de Madrid

MATHEMATICAL MODELING OF COGNITIVE PROCESSES WITH APPLICATIONS IN NEUROSCIENCE AND ROBOTICS

MODELIZACIÓN MATEMÁTICA DE PROCESOS COGNITIVOS CON APLICACIONES EN NEUROCIENCIA Y ROBÓTICA

Doctoral Thesis
Carlos Calvo Tapia

Supervisor
Valeriy Makarov Slizneva

Facultad de Ciencias Matemáticas

2019

UNIVERSIDAD COMPLUTENSE MADRID

DECLARACIÓN DE AUTORÍA Y ORIGINALIDAD DE LA TESIS PRESENTADA PARA OBTENER EL TÍTULO DE DOCTOR

D./Dña. Carlos Calvo Tapia,
estudiante en el Programa de Doctorado IMEIO,
de la Facultad de Ciencias Matemáticas de la Universidad Complutense de Madrid, como autor/a de la tesis presentada para la obtención del título de Doctor y titulada:

Mathematical modeling of cognitive processes with applications in Neuroscience and Robotics

y dirigida por: Valeriy Makarov Slizneva

DECLARO QUE:

La tesis es una obra original que no infringe los derechos de propiedad intelectual ni los derechos de propiedad industrial u otros, de acuerdo con el ordenamiento jurídico vigente, en particular, la Ley de Propiedad Intelectual (R.D. legislativo 1/1996, de 12 de abril, por el que se aprueba el texto refundido de la Ley de Propiedad Intelectual, modificado por la Ley 2/2019, de 1 de marzo, regularizando, aclarando y armonizando las disposiciones legales vigentes sobre la materia), en particular, las disposiciones referidas al derecho de cita.

Del mismo modo, asumo frente a la Universidad cualquier responsabilidad que pudiera derivarse de la autoría o falta de originalidad del contenido de la tesis presentada de conformidad con el ordenamiento jurídico vigente.

En Madrid, a 30 de agosto de 2019

Fdo.: 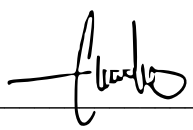

Esta DECLARACIÓN DE AUTORÍA Y ORIGINALIDAD debe ser insertada en la primera página de la tesis presentada para la obtención del título de Doctor.

I've heard it said
that people come into our lives
for a reason,
bringing something we must learn.
And we are led
to those who help us most to grow
if we let them
and we help them in return.
Well, I don't know
if I believe that's true,
but I know I'm who I am today
because I knew you.

— Stephen Schwartz, *Wicked*

Agradecimientos

En primer lugar quiero dar las gracias a mis directores de tesis, Valeri Makarov y José Antonio Villacorta. Por concederme la oportunidad de trabajar a su lado desde el primer día, como un miembro más del gran equipo que forman. Por dejarme mirar un poco más allá de las matemáticas. Y por hacerme entender que la redacción de esta memoria no debía ser el objetivo de mi etapa de doctorado, sino el resultado de cinco años creciendo a su lado como científico.

Desde luego, gracias a mis padres. Por empeñarse en sacrificarse para darme todo lo mejor. Y por su apoyo incondicional. También a mi hermano. Por ser la primera persona que me enseñó a escribir códigos en Matlab, aunque ahora él no entienda ni el encabezado de los aquí incluyo.

No me olvido de mis compañeros. Los que conocí hace ya más de diez años cuando pisé por primera vez la que ahora es mi segunda casa. Gracias por darle sentido a estudiar una carrera que aunque ahora está de moda, por aquel entonces requería de cierto aporte de locura innata para escogerla. A los que me habéis acompañado durante mi etapa de doctorado, gracias por compartir alegrías, angustias, éxitos y miserias. Por esperarme para comer juntos cuando el puto robot quería ponerme a dieta. En especial, gracias a mi fiel compañera de despacho. Por enseñarme que, pese a que cuesta encontrarlas, existen mentes brillantes que saben disfrutar de la vida.

Gracias también a todos los que durante estos años han formado parte de mi otra vida. A los equipos de *La voz humana*, de *24 horas en la vida de una mujer*, de *Anastasia* y de *Taller de corazones*. De no ser por el aire fresco que me aporta trabajar con ellos, esta tesis nunca habría llegado a escribirse.

A mis amigos no matemáticos, que son muchos y muy buenos, gracias por haber seguido queriendo estar a mi lado, sobre todo cuando para planificar cualquier quedada había que buscar un finde libre a tres meses vista por mi culpa.

Por último, a quien al leer la dedicatoria impresa en la anterior hoja se haya sentido aludido por los versos prestados, gracias.

Contents

Abstract / *Resumen*

Mathematical modeling of cognitive processes with applications in Neuroscience and Robotics

Evolution has shaped living beings equipping them with a set of cognitive abilities to perceive the external world in an abstract way, in order to survive in their specific environments and hence perpetuate the species. In particular, the nervous system and, ultimately, the brain have been developed to provide animals and humans with the capability of interacting with complex time-changing environments by allowing them to make sophisticated decisions in real time. This ability is paramount for survival but, paradoxically, the neural mechanisms and functional processes supporting it are poorly understood.

This thesis proposes the mathematical modeling of essential cognitive mechanisms that allow an individual to understand different time-changing situations to interact with them in an optimal, versatile, and robust way. Following a bottom-up approach, the content of the present work pursues two main aims. First, we deal with the issue of Imitation, a preeminent form of learning commonly used by children and adults, and also observed in many species. It enables the transfer of information between down generations without the need for genetic inheritance. Here we will study the cognitive processes behind imitation learning, and propose a mathematical formulation of the underlying mechanisms, as well as we will detail their applications in Robotics, insofar as they can bring light to the paradigm of *Learning from Demonstration*. This form of learning is especially useful in the first stages of life. However, once a certain level of autonomy is reached, the individual experiences a second phase of learning, used to acquire the remaining relevant cognitive skills, which complete its adaptation to the environment. Taking the brain as a model, the second goal of this work is the study of mathematical models describing the abilities exhibited by cognitive beings to cope autonomously with dynamic, i.e. time changing, situations. From the point of view of Artificial Intelligence, this aim can be summarized in a simple but fundamental question: how can we make a humanoid robot navigate and manipulate objects in the way as a cognitive agent would do, that is, reaching its goals and avoiding undesired interactions, as collisions? Imitation learning is addressed here from the perspective of synchronization between dynamical systems modeling neural networks. The proposed model considers learning relationships between two

independent agents that respond to different sequential orders given by two decoupled neural networks. The information transfer is implemented resorting to mathematical control theory, through learning rules that change the local couplings in the learner network according to the dynamics of the teacher. On top of testing the model through numerical simulations, we also experimentally validate our theoretical results in two mobile robotic platforms, playing roles of teacher and learner. The teacher, driven by a fixed neural network, moves along a pre-designed complex trajectory, whereas the learner is prompted to tune itself according to the introduced learning model. We show that after a few demonstrations of the implemented teacher's pattern, the learner is finally able to replicate the exhibited trajectory.

The theory of cognition developed in this thesis proposes that main basic cognitive abilities needed for survival in time-changing environments, such as navigation and manipulation, arise as different aspects of a single dynamic process, the so-called time compaction. According to this theory, a perceived dynamic situation is transformed by our brain into an internal static representation: the so-called Generalized Cognitive Map or GCM, which contains all the information required by the brain to act accordingly. This abstraction can be artificially obtained in a discrete reaction-diffusion system of equations with appropriate boundary conditions. In this thesis we use the theory of time compaction to unify fundamental aspects of cognition under a single concept, capable of being mathematically analyzed and memorized, artificially implemented, and experimentally validated in robotic platforms, in scenarios of real-time navigation and manipulation.

Modelización matemática de procesos cognitivos con aplicaciones en Neurociencia y Robótica

A lo largo de su evolución los seres vivos han ido adquiriendo un conjunto de habilidades cognitivas que les permite percibir el mundo externo de una manera abstracta, con el propósito de sobrevivir en entornos específicos y perpetuar la especie. En particular, el sistema nervioso y en última instancia el cerebro se han desarrollado para que animales y humanos sean capaces de interactuar con entornos dinámicos complejos y puedan así tomar decisiones precisas en tiempo real. Esta capacidad es primordial para la supervivencia pero, paradójicamente, los mecanismos neuronales y procesos funcionales involucrados son todavía una incógnita.

Esta tesis propone la modelización matemática de procesos cognitivos esenciales que permiten a un individuo comprender diferentes situaciones dinámicas para interactuar con el entorno de una manera óptima, versátil y robusta. El contenido de este trabajo persigue dos objetivos principales. Primero abordaremos el tema de la imitación, una forma preeminente de aprendizaje comúnmente utilizada por niños y adultos y presente también en muchas especies. Permite la transferencia de información entre generaciones sin necesidad de modificaciones genéticas hereditarias. Estudiaremos los mecanismos cognitivos que hay detrás de los procesos de aprendizaje por imitación, así como sus aplicaciones en Robótica, en la medida en que puedan arrojar luz al conocido como Learning from Demonstration Paradigm. *Esta forma de aprendizaje es especialmente útil en las primeras etapas de desarrollo. Una vez se alcanza cierto nivel de independencia el individuo experimenta una segunda fase de aprendizaje autónomo, del cual se sirve para adquirir el resto de habilidades cognitivas relevantes que completan su adaptación al medio. Tomando el cerebro como modelo, el segundo objetivo de este trabajo es la búsqueda de una descripción matemática de las habilidades que muestran los agentes cognitivos cuando hacen frente a situaciones dinámicas. Desde el punto de vista de la Inteligencia Artificial, este objetivo puede resumirse en una simple pregunta: ¿cómo podemos diseñar un robot humanoide que se desplace y desenvuelva como lo haría un agente cognitivo, es decir alcanzando sus objetivos sin colisionar con otros agentes de su entorno?*

El aprendizaje por imitación se aborda aquí desde la perspectiva de la sincronización de redes neuronales. El modelo propuesto considera una relación de aprendizaje entre dos agentes independientes que responden a diferentes órdenes secuenciales dadas por dos redes neuronales desacopladas. La transferencia de información se implementa a través de reglas de aprendizaje que, apoyándose en una variable de control y en un mecanismo de adataptación de grafos, consiguen modificar los acoplamientos locales en la red del alumno de acuerdo con la dinámica observada en el profesor. Además de probar el modelo a través de simulaciones numéricas, también se ha validado experimentalmente haciendo uso de dos plataformas robóticas móviles ejerciendo roles de profesor y alumno. El profesor, conducido por una red neuronal fija, describe una trayectoria compleja prediseñada, mientras que el alumno debe adaptar la suya propia, inicializada aleatoriamente, de acuerdo al modelo de aprendizaje

establecido. Demostramos que, tras unas pocas observaciones del patrón de movimiento implementado en la red del profesor, el alumno acaba replicando la trayectoria deseada.

La teoría de cognición desarrollada en este trabajo propone que las habilidades cognitivas básicas necesarias para la supervivencia en entornos dinámicos, tales como la navegación y la manipulación, surgen como diferentes aspectos de un solo proceso dinámico, conocido como compactación del tiempo. Según esta teoría nuestro cerebro transforma cualquier situación dinámica percibida en una representación interna estática, que llamamos Mapa Cognitivo Generalizado. Esta abstracción, que puede concebirse matemáticamente a través de la integración de un sistema de reacción-difusión con condiciones de contorno adecuadas, contiene toda la información requerida por el cerebro para actuar en consecuencia de manera apropiada. El trabajo desarrollado se apoya en la teoría de la compactación del tiempo para unificar diferentes aspectos fundamentales de la cognición bajo un único concepto, capaz de ser matemáticamente analizado y memorizado, implementado artificialmente y validado experimentalmente en escenarios reales de navegación y manipulación.

Introduction

Nature has endowed living beings with a set of cognitive abilities that allow them to perceive the external world in an abstract way, with the purpose of making specific decisions to survive in their environments. The biggest challenge faced by the brain is the understanding of our reality, in order to properly interact with it. It is therefore reasonable to think that due to the huge amount of information it involves, sophisticated neural mechanisms are required to support these functions.

The presence of time is the major source of complexity when our brain must understand the surrounding world. In fact, one of the central currents of thought in Neuroscience argues that the evolution of the nervous system in nature is due to its adaptation to time-changing environments [1]. In this sense, the presence of time could explosively increase the amount of processed information. However, even the simplest mammals deal with all this information in a fast and reliable way. This means that there exist neural mechanisms that offer an unknown and qualitatively different information processing than those proposed today in the literature on Artificial Intelligence. Unraveling these processes will make a breakthrough with a profound scientific impact, both in terms of Fundamental Science, with regard to expanding our knowledge about the brain and its mechanisms, and in terms of its application to Robotics and Artificial Intelligence, since the implementation and replication of such processes in artificial agents could provide them with cognitive abilities similar to those exhibited by humans.

Motivation and goals

The brain is the most sophisticated system of the known universe. It harbors our consciousness and has the ability to perceive and understand the vastness of the external world. The brain is essentially made up of neurons. There are on the order of 10^{11} neurons in the adult human brain, connected to each other through about 10^{14} synaptic contacts. The brain exhibits an overwhelming complexity at a structural and functional level, which confers it amazing capabilities that we are still far from understanding. However, all this sophistication and complexity arise driven by a single premise: survival [1].

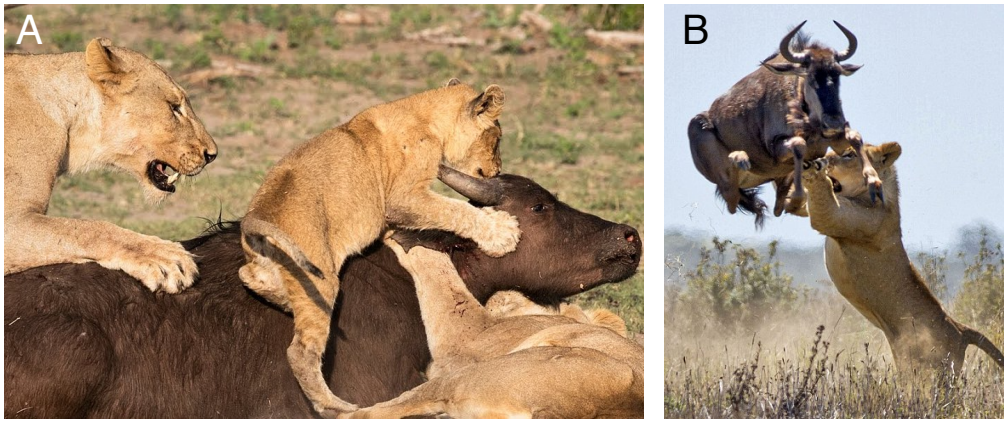

Figure 1: Evolution has shaped living beings with the purpose of survival in specific environments and hence perpetuate the species. **A)** Social learning. Animals learn from other animals, especially in the first stages of life. **B)** Autonomous interaction with the environment. Individual learning provides the brain with relevant cognitive skills needed to interact with the time-changing real world and hence to survive.

Social learning is a powerful brain process known to impact the success and survival of humans and non-human animals alike [2]. Animals learn from other animals, especially during their first stages of life (Fig. 1A). This phenomenon is well established across numerous species and contexts, from fish learning mating sites by following others [3], to meerkats teaching pups to handle scorpions [4]. Mimicking complex actions and strategies from more experienced individuals can provide animals with a shortcut to adaptive behavior, minimizing the costs and risks of individual exploration [5] and, consequently, maximizing the possibilities of survival. Once some level of autonomy is achieved, there exists evidence that a second phase of individual learning takes place [6], in order to provide the brain with relevant cognitive skills that complete its adaptation (Fig. 1B). This second stage supposes an autonomous learning in the sense that there is no referents beyond the experience itself. It endows the individual with complementary cognitive capabilities required to interact with the real world, in order to ultimately perpetuate the species.

This thesis proposes the mathematical modeling of different cognitive processes that allow an individual to understand different time-changing situations to interact with it in an optimal, versatile, and robust way. The project has been developed based on previous results of our research group, Cogneubotics [7, 8, 9, 10], and aims to progress in the search for a theoretical framework that unifies the different perspectives under which cognition is studied.

The content of this work can be neatly separated in two main parts. First, we deal with the issue of *Imitation*, a preeminent form of learning commonly used by children and adults, and also observed in many species. It allows for the transfer of information between individuals and down generations without the need for genetic inheritance [11]. Here we will study the cognitive mechanisms behind the imitation learning processes, as well as its applications in Robotics, insofar as they can bring light to the paradigm of Learning from Demonstration.

The second aim of the present work is focused on *Basic Cognition*, a way of autonomous interaction with the environment, and can be summarized in a simple question: how could we achieve a cognitive robot capable to navigate and manipulate like a human being would? This ambitious objective implies not only to provide the robot with abilities to interact safely with humans and other cognitive agents (free-collision navigation, versatile and precise manipulation, etc.), but moreover to create a cognitive basis for memorizing such interactions, learn from them, classify and structure them as coherent experiences, etc.

To this extent, a bottom-up approach has been carried out. First, each essential cognitive process intended to be treated is presented in a synthetic way: a mathematical formulation of the fundamental concepts is then proposed to offer operational definitions with which to start to make progresses in objective terms. The next step is to establish dynamic relationships between these concepts, essentially found through nonlinear differential equations, control theory, adaptive algorithms, etc. The analytical and numerical study of these systems finally allows characterizing the modeled problem, offering experimentally testable predictions which ultimately are implemented in real mobile robotic platforms.

Imitation learning

Social learning is widely observed in many species. Less experienced agents copy successful behaviors exhibited by more experienced individuals. Nevertheless, the dynamical mechanisms behind this process remain largely unknown. Robot Learning from Demonstration (LfD), also known as Imitation Learning and Apprenticeship Learning, is a paradigm for enabling robots to autonomously perform new tasks. The main principle of robot LfD is that end-users can teach robots new tasks without programming. In a tradicional scenario, a human programmer would have to reason in advance and code a robot controller that is capable of responding to any situation the robot may face, no matter how unlikely. In contrast, LfD allows the end-user to 'program' the robot simply by showing it how to perform the task: no coding required. Then, when failures occur, the end-user needs only to provide more demonstrations [12]. C.L. Nehaniv and K. Dautenhahn [13] phrased the problems faced by LfD in a set of key questions: *What to imitate?*, *How to imitate?*, *When to imitate?*, *Whom to imitate?* To date, only the first two questions have been really addressed.

While learning from demonstration, an agent (human or robot) first has to isolate essential motor motifs from the movement of another more experienced agent (e.g., *move right*, *turn left*, etc.). Then it must be able to compose a meaningful behavior from these motifs. In this thesis we will study mechanisms of replication of the connectivity patterns by learning in chains of network motifs. To tackle the problem we adopt a use case approach. As a testbed we consider an asymmetric Lotka-Volterra model with global inhibitory couplings among neurons [14, 15]. Thus, each network motif in the learning process exhibits Winner-Less Competition (WLC) dynamics (a heteroclinic circuit connecting saddle equilibria, see, e.g., [14, 16, 17]) and acts as a teacher for the next motif in a chain. In Chapter 1 we will show that, under appropriate training, a chain of network motifs with three coupled neurons each

can progressively "copy" connectivity patterns, allowing synchronization. In Chapter 2 the proposed model will be improved, generalized to arbitrary number of neurons per motif, and finally validated on two real mobile robotic platforms, playing roles of teacher and learner.

Autonomous interaction with the environment

Cognitive skills required for coping with dynamic environments are mandatory to survive, as revealed by their ubiquity even in the simplest animals [9]. However, its mathematical description and implementation in artificial agents remain a challenge. In fact, according to Moravec's paradox, postulated in the 1980s, high-level abilities (as conversation capabilities, mathematical skills, etc.) require little computational resources in comparison with low-level sensory and motor skills, which require extraordinary computational efforts. An autonomous robot capable of operating and interacting with humans must, on the one hand, understand the environment in terms of "what is going on" and "how can I deal with it" ("consciously"), and on the other, memorize experiences and learn from the successful ones to make use of them later automatically ("subconsciously").

A classic example is the motor ability developed by a mobile agent (human being, animal) to achieve a specific goal in a dynamic environment. Such skill requires the rapid and reliable generation of flexible decisions not only taking into account the current state of the environment and the agent, but also inferring their future states [8]. The theory of cognition developed in the second part of this thesis proposes that main basic cognitive abilities needed for suvival in time-changing environments, such as navigation and manipulation, arise as different aspects of a single dynamic process, according to which a perceived dynamic situation is transformed by our brain into an internal static representation, called Generalized Cognitive Map (GCM) or Compact Internal Representation (CIR). This abstraction contains all the information required by the brain to act accordingly, structured in such a way that the memorization and learning of each faced situation arises naturally, allowing to establish complex relationships between different experiences (similarity, interpolation, clusterization, modularity, etc.). Therefore, the theory of GCMs constitutes an ideal theoretical framework that unifies fundamental aspects of cognition under a single concept, capable of being mathematically analyzed, artificially implemented (Chapter 3), and experimentally validated in scenarios of real-time navigation (Chapter 4) and manipulation (Chapter 5). In addition, when compacting the temporal dimension, GCMs are likely to be easily memorized. In this regard, results presented in Chapter 6 constitute a basis for emergence of episodic memory in ensembles of single neurons.

State of the art

Throughout the last decades the study of the phenomenon of cognition has been approached from multiple disciplines. Biology [18], Neuroscience [19], Robotics [20] or Psychology [21]

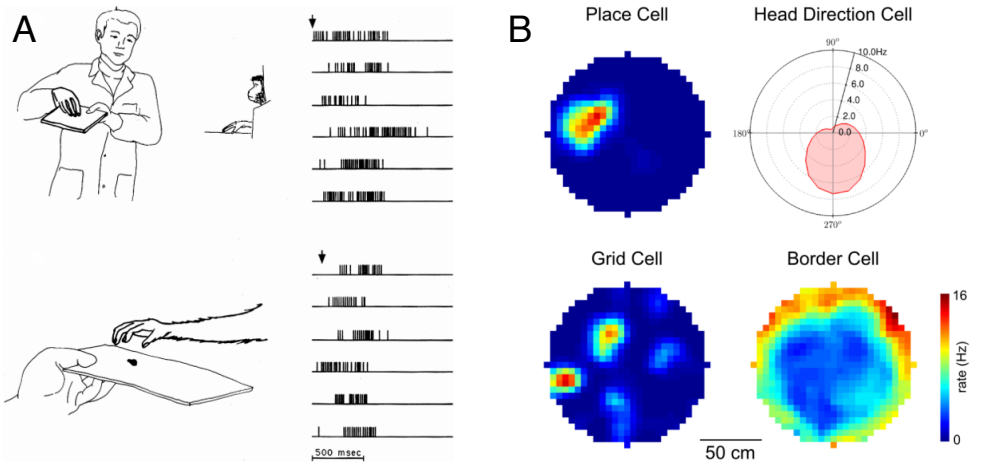

Figure 2: A) Example of a mirror neuron selectively discharging during observation of a grasping movement done by the experimenter (top) and during monkey grasping movements (bottom). Arrows denote the onset of the movement. Six trials are shown for each condition. Retrieved from [24]. **B)** Some results about electrical activity in the rat's brain. Examples of four different cell types in the hippocampus (place cell) and entorhinal cortex (head direction cell, grid cell and border cell). The activity of each cell was recorded while a rat explored a large open field and their spatial (or directional) tuning curve is plotted. Retrieved from `https://kloostermanlab.org/research/spatial-code/`.

have provided complementary perspectives to the same problem. However, the knowledge about the mechanisms involved in cognitive processes related to the versatile and effective decisions observed in living beings is very limited. Nowadays, the need for a common language that allows the convergence and integration of these disciplines into a single framework is becoming increasingly evident, leading to global advances in our understanding of cognition.

Regarding our knowledge about the brain mechanisms involved in the learning from demonstration, electrophysiological studies suggest that the so-called mirror neurons play a fundamental role [22, 23]. Mirror neurons represent a distinctive class of cells that discharge both when the monkey executes a motor act and when it observes another individual (a human being or another monkey) performing the same or a similar motor act [24] (Fig. 2A). Neurophysiological (EEG, MEG, and TMS), and brain-imaging (PET and fMRI) experiments provided strong evidence that a fronto-parietal circuit with properties similar to the monkey's mirror neuron system is also present in humans [25]. In order to recognize an action, the activation of the mirror circuit is essential to provide the observer with a real experiential comprehension of the observed action. From this perspective, mirror neurons could represent a 'core mechanism"from which other functions branched off. One of these is imitation, that is the ability to replicate an observed action already present in the observer motor repertoire or to learn a new motor action. The mirror neuron system, by providing motor copies of the observed actions, appears to be the ideal mechanism for imitation. Indeed there is clear evidence that mirror neuron system is involved both in immediate repetition of actions done by others [26] and in imitation learning [27].

Here the concept of mirror neuron has been taken as a starting point to present an approach to fast social-like learning of complex motor behaviors. The proposed model allows synthesizing behaviors in a neural network of a learning agent by observation of the dynamics of a teacher. From the dynamical systems viewpoint the social learning is reduced to the problem of copying, in terms of synchronization, ordered in time patterns of neuronal activity from one experienced agent to another, novel one. The learner should be able to adjust its network couplings by only observing the teacher dynamics, which leads to synchronization of the behaviors.

Concerning spatial cognition, i.e. those brain mechanisms involved in the processing of time-invariant scenarios, modern science has witnessed significant progresses. A large number of studies showed a crucial role of the hippocampus, a part of mammalian limbic system, in spatial memory. The hippocampus is necessary for navigation to target places using distal cues [28], discrimination of places [29], or discrimination of an object's location [30]. Several cell types within the medial temporal lobe have been detected in the past few decades that serve to create a mental representation of the environment, known as a cognitive map [31]. Recent studies suggest that a certain cell type in rodent hippocampus encoding the position of the own animal in the space, known as place cells [32], might also encode sufficient information for spatial representation of conspecifics [33, 34]. Nonetheless, and despite their critical importance, neuronal ensembles that specifically code the particular position of an object have begun to be described very recently, but these are accessible objects. i.e. elements that can be reached and explored by the animal [35]. Nonetheless, for survival in the real world, any animal and human receives the most important information from the part of the environment immediately inaccessible (the position of a prey or predator, the car that can hit us, etc.). Therefore, this line of research is essential to understand the neurobiological mechanisms involved in the processing of our spatiotemporal world.

In this thesis the challenge of understanding the functional bases of spatiotemporal cognition required to interact with the world is addressed by merging time and space in a single functional framework through the hypothesis of Prediction-for-CompAction (PfCA) [7]. The hypothesis integrates the conceptual bases of spatial cognition with specific mechanisms dealing with the time dimension and offers an efficient cognitive mechanism to cope with dynamic environments. According to this paradigm, a dynamic situation is internally represented as a static Generalized Cognitive Map (or GCM), which results from the spatial arrangement of the predicted interactions among the elements in the environment. GCMs emerge as a generalization of the cognitive maps known in Neuroscience. These cognitive maps are created from the activity of certain neuronal populations that encode information related to the position of the subject (place cells), position and size of objects (boundary cells), distances (grid cells), etc. [36, 37] (Fig. 2B). The concept of cognitive map appears as internal representations of static environments, and has been widely used in robotics [20] as an attempt to reproduce the structure and functionality of real neural networks in artificial systems. However, as with the animals themselves, this approach has only been valid in static environments, clearly showing insufficient in dynamic situations. In fact, today the study of methods and algorithms that allow autonomous robots to move safely and versatilely in

dynamic environments is one of the most active research fields in robotics.

The confirmation of time compaction predictions has a twofold deep impact in Neuroscience. On the one hand, it shows that time compaction is a novel cognitive mechanism likely invariant in mammals (since it was recently described in humans [38]). On the other hand, it suggests that time compaction generalizes (to time-changing environments) the 2014 Nobel-awarded theory of cognitive maps developed in the context of static (time invariant) environments. Therefore, the breakthroughs presented in this thesis open new venues to study how our brain processes, understands, memorizes and learns the reality.

1 | Synchronization in neural networks

Complex large-size biological, ecological, and engineering networks can be frequently decomposed into relatively small network *motifs*, i.e. network patterns that occur significantly more frequently than in a random graph. Then, the study of the network structural properties can be addressed through the investigation of universal classes or building blocks of recurrent network motifs [39]. Network motifs have been found in transcription networks in organisms from bacteria to humans [40], in brains [41] and in social networks [42], among others. How one network motif can dynamically replicate the internal structure and the behavior of another one is an open problem.

Recently a strong effort has been made to develop efficient algorithms for discovering and classifying motifs in complex networks [43, 44]. The synchronization of oscillatory activity in networks of neural networks is usually implemented through coupling the state variables describing neuronal dynamics. In this chapter we introduce another but complementary mechanism based on a learning process with memory [45, 46]. A driver network motif, acting as a teacher, exhibits winner-less competition (WLC) dynamics [14], while a driven motif, a learner, tunes its internal couplings according to the oscillations observed in the teacher. We show that under appropriate training the learner motif can dynamically copy the coupling pattern of the teacher and thus synchronize oscillations with the teacher.

Then, we demonstrate that the replication of the WLC dynamics occurs for intermediate memory lengths only. In a unidirectional chain of N motifs coupled through teacher-learner paradigm the time interval required for pattern replication grows linearly with the chain size, hence the learning process does not blow up and at the end we observe phase synchronized oscillations along the chain. We also show that in a learning chain closed into a ring the network motifs come to a "consensus", i.e. to a state with the same connectivity pattern corresponding to the mean initial pattern averaged over all network motifs.

1.1. Introduction

From a dynamical systems point of view, an analysis of the time evolution of network motifs is considerably a more difficult problem than the analysis of their structure. In this context, the problem of synchronization in an n-node sub-graph has shown significant relation to the relative abundance of certain motifs [47]. The emergence of polyrhythmic dynamics of motifs has been found in small inhibitory-excitatory networks [48]. However, a general understanding of how local motif dynamics is integrated into global network behaviors is far from its end.

Traditionally, synchronization of oscillations in network systems involves transmission of signals (energy) from one network element to another. For example, in neural networks synaptic couplings may convey electrical or chemical signals from one motif to another, which frequently promotes synchronization [49]. However, synchronization can also be achieved through a learning process. In this case there is no direct link between two networks. Instead, the information transfer is attained through observation of the teacher dynamics and by consecutive tuning of the connectivity pattern in the learner. Although such kind of synchronization is abundant in real world (e.g. children can learn movements shown by a teacher), its study from a dynamical systems point of view has attracted relatively little attention.

It has been shown that oscillations in network systems can emerge from a stable heteroclinic channel [50, 51]. In a neural network consisting of more than two competing neurons with unbalanced inhibitory connections, one may observe a situation when each neuron sequentially becomes a winner (i.e. strongly activated) for a limited time interval and then another neuron takes over the leadership. Dynamically such an operating mode, called winner-less competition (WLC), occurs in a vicinity of heteroclinic trajectories connecting saddle equilibria in a loop. Under certain conditions, the heteroclinic loop can be stable and then in the presence of a weak noise the trajectory will wander from one saddle to another [14, 16, 17].

In this chapter we propose a learning rule which allows one neural network, acting as a teacher, to impose the same heteroclinic circuit in another "learner" network. As a result, in the learner there appear WLC oscillations synchronized in phase with the oscillations of the teacher. We study how the information on the connectivity structure is replicated in a chain of network motifs. The proposed learning rule includes memory effects, i.e. the learner integrates over time the incoming information. We then provide conditions necessary for replication of the connectivity patterns in a learning chain of network motifs and also describe a "consensus" behavior on a ring.

1.2. Model dynamics: Synchronization by learning

Figure 1.1A shows the architecture of a network motif composed of three recurrently coupled neurons. For the sake of simplicity we assume that the coupling strengths β are hard coded (i.e. fixed), while $\alpha = \{\alpha_k\}_{k=1}^3$ can be changed. Further on we will consider a unidirectional

chain of such motifs (Fig. 1.1A). At the beginning the couplings α are arbitrary distributed among network motifs, and hence the motifs exhibit different dynamics. The purpose of learning is to replicate the coupling pattern α from the teacher and synchronize oscillations along the chain.

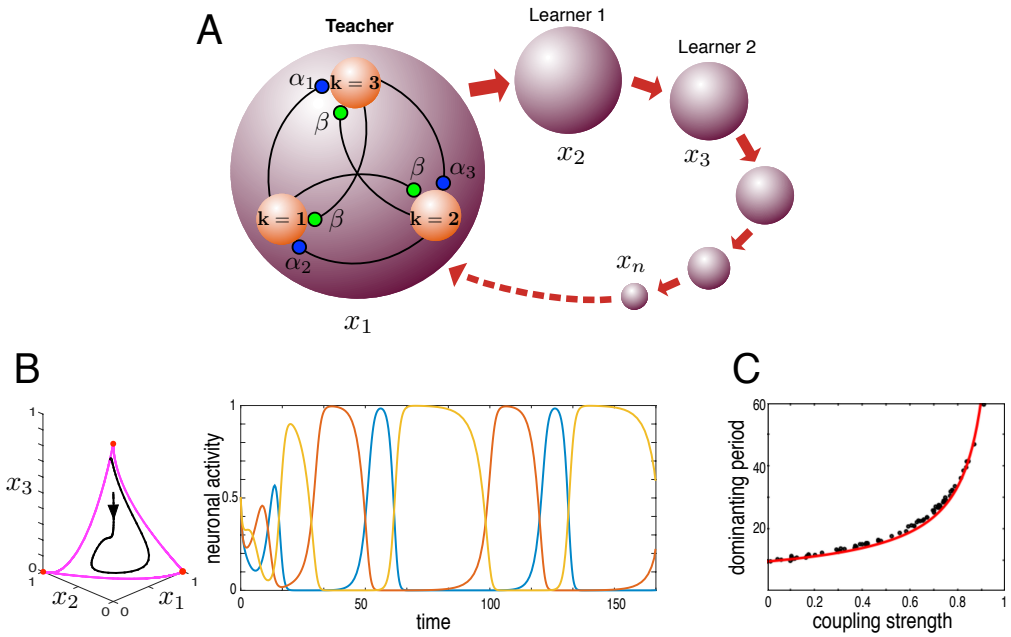

Figure 1.1: The model. **A)** Network motifs consist of three recurrently coupled neurons each. Motifs are linked in a unidirectional learning chain. No direct coupling among the state variables exists. Instead, learner n adjusts its connectivity pattern to that of motif $n-1$ and thus synchronizes oscillations. If the last motif is linked to the first one we get a ring chain without leader. **B)** Winner-less dynamics in the phase space of a single motif with $\alpha = (0{,}1, 0{,}6, 0{,}8)$ (left) and time evolution of the neuronal activity (right). Blue, red, and yellow curves correspond to neurons 1, 2, and 3, respectively. **C)** The period of dominant activity p versus the corresponding coupling strength, α_k

1.2.1. Heteroclinic circuit: Winner-less dynamics

The network of motifs is organized by the teacher-learner principle. The governing equation of the teacher is given by the generalized Lotka-Volterra system

$$\dot{x} = x \odot (1 - \rho x) + \eta(t), \tag{1.1}$$

where $x(t) \in \mathbb{R}^3_+$ describes the activation state of three neurons at time t (Fig. 1.1B, left, black trajectory), $\odot$ stands for the Hadamard product, $\eta(t) \in \mathbb{R}^3$ is a Gaussian uncorrelated white noise with the mean 2e-5 and the standard deviation 1.5e-3, and the matrix $\rho \in \mathcal{M}_{3\times3}(\mathbb{R}_+)$ accounts for local couplings among the neurons:

$$\rho = \begin{pmatrix} 1 & \alpha_2 & \beta \\ \beta & 1 & \alpha_3 \\ \alpha_1 & \beta & 1 \end{pmatrix}.$$

Given that the following conditions are satisfied

$$\alpha_k < 1 < \beta, \quad \prod_{k=1}^{3}(1-\alpha_k) < (\beta-1)^3, \tag{1.2}$$

it has been shown [52] that in the system (1.1) there exists a globally stable heteroclinic circuit (Fig. 1.1B, left, in pink). Further on we will assume that $\beta > 2$ ($\beta = 2{,}8$ in numerical simulations). Then, condition (5.8) will be satisfied whenever $\alpha_k < 1$. For the sake of clarity, we will use double notation: index k will be used for all intra-motif variables, whereas index n will denote the motif number in the learning chain.

Figure 1.1B (left) shows a typical example of a trajectory in the phase space of Eq. 1.1 imposed by a heteroclinic circuit connecting equilibrium points $(1,0,0)$, $(0,0,1)$, and $(0,1,0)$. The trajectory quickly approaches the heteroclinic circuit and we observe stable WLC-type oscillations in the network (Fig. 1.1B, right). Numerical simulation shows (1.1C, black dots) that the time intervals during which the activity of the k-neuron prevails over the others, $\{t \geq 0 : x_k(t) > \max_{i \neq k} x_i(t)\}$, increase with the magnitude of the corresponding coupling α_k. The length of these intervals can be estimated [15] by approximating the model 1.1 in a vicinity of a saddle equilibrium. It has been shown that the period follows the law:

$$p(\alpha_k) = \frac{p_0}{1+\log 2}\frac{1+\log(2-\alpha_k)}{1-\alpha_k}, \tag{1.3}$$

where is the period when $\alpha_k \to 0$. Figure 1.1C shows the data fit with $p_0 = 9{,}57$. For further calculations it is worth noting that $p(\cdot)$ is a strictly increasing function.

1.2.2. Synchronization by learning

Let us now consider a learning chain of network motifs (Fig. 1.1A). Since the learning is unidirectional, we can consider a pair teacher-learner, i.e. motifs n and $n-1$ will be referred to as a learner and a teacher, respectively.

Definition 1.1. *Under phase synchronization by learning we understand the situation when independently on the teacher coupling pattern α_{n-1} and the initial conditions $x_{n-1}(0)$, $x_n(0)$, and $\alpha_n(0)$, after some transient the following inequality is satisfied:*

$$|\phi_{n-1}(t) - \phi_n(t)| < M, \tag{1.4}$$

where ϕ_{n-1} and ϕ_n are the oscillatory phases in the teacher and in the learner, respectively, and M is a constant.

Without loss of generality, we can assume that each teacher motif has a fixed coupling structure. At the beginning, the connectivity pattern in the learner $\alpha_n(0)$ is taken arbitrary from the uniform distribution over $(0,1)^3$. Then the purpose of learning is to "copy" the coupling structure and consequently to synchronize oscillations in the learner with the teacher.

Remark 1.1. *Since the teacher network cannot change the learner state $x_n(t)$ directly, but through the coupling strengths $\alpha_n(t)$ only, during the learning we expect:*

$$\lim_{t\to\infty} \|\langle\alpha_n\rangle_T(t) - \alpha_{n-1}\|_2 = 0, \tag{1.5}$$

where

$$\langle u\rangle_T(t) = \frac{1}{T}\int_{t-T}^{t} u(s)\,\mathrm{d}s$$

denotes the time averaging operator over period T. Then, fulfillment of (1.5) ensures (4.2). In numerical simulations the learning will be deemed finished if the norm in (1.5) falls below a tolerance value $0 < \delta \ll 1$ for some t^*.

1.2.3. Learning rule

We will employ a Hebb-like rule for learning. First, we introduce a functional:

$$g(u(t)) = u(t) \odot \frac{1}{\tau}\int_{t-\tau}^{t} u(s)\,\mathrm{d}s, \tag{1.6}$$

where $\tau \geq 0$ is a constant describing the memory length. The function $g(x_{n-1})$ represents the cumulative activity of the neurons in the teacher network. Then, we can introduce the following learning rule:

$$\dot{\alpha}_n = \epsilon[g(x_{n-1}) - g(x_n)], \tag{1.7}$$

where $\epsilon > 0$ is the learning rate and the term in brackets is the error function described as teacher forcing based on the classical delta rule [53].

Remark 1.2. *Definition 1.1 allows for a non-zero phase shift between the teacher and the learner motifs. Thus, in general the learning error $E = g(x_{n-1}) - g(x_n)$ can be an oscillatory function of time, even at $t \to \infty$. Therefore, we will say that the learning given by equation (1.7) is successful if $\lim_{t\to\infty}\langle E\rangle_T(t) = 0$.*

1.3. Effect of memory on synchronization

Further on we will assume that the learning rate is small enough, $\epsilon \ll 1$. Then, the coupling strengths in the learner are slow functions of time $\alpha_n = \alpha_n(\epsilon t)$. Therefore, on time scales proportional to $1/\epsilon$ the state variable, $x_n(t)$, follows the standard WLC dynamics

Theorem 1.1

Given that $\tau = 0$, the learning process 1.7 converges to a manifold

$$rP(\langle\alpha_n\rangle_T) = p_0 P(\alpha_{n-1}), \tag{1.8}$$

where $P(\nu) \equiv (P_1, P_2, P_3)^T$, $P_k = p(\nu_k)$, and $0 < r < \|P(\alpha_{n-1})\|_\infty$ is a parameter.

Proof of Theorem 1.1. Since α_n is a slow function of time, we apply an averaging method to Eq. 1.7. For the first order approximation we can write $\alpha_n = \gamma_n + \epsilon\Phi_n(t, \gamma_n)$, where Φ_n is an oscillatory function and $\gamma_n(t)$ satisfies

$$\dot{\gamma}_n = \epsilon \left(G(\alpha_{n-1}) - G(\gamma_n)\right), \tag{1.9}$$

where

$$G(\nu) = \frac{1}{T(\nu)} \int_0^{T(\nu)} g(u(s))\mathrm{ds}, \tag{1.10}$$

$T(\nu) = \sum_{k=1}^3 p(\nu_k)$ is the period of oscillations in a network motif with couplings ν, and u is the activity of its neurons. For $\tau = 0$ we get [15] $T(\nu)G(\nu) = c_0 P(\nu)$, where c_0 is a constant of order unity. Thus, by denoting $R(\nu) = P(\nu)/T(\nu)$, the system 1.9 can be written as:

$$\dot{\gamma}_n = \epsilon c_0 \left(R(\alpha_{n-1}) - R(\gamma_n)\right). \tag{1.11}$$

This system has a one-dimensional equilibrium manifold: the set of $\bar{\gamma} \in \mathbb{R}^3$ verifying $rP(\bar{\gamma}) = p_0 P(\alpha_{n-1})$, which for $\epsilon \to 0$ provides 1.8. Let us now introduce a Lyapunov function:

$$V(t) = \frac{1}{2}\|F(\alpha_{n-1}, \gamma_n(t))\|_2^2,$$

where $F(\alpha, \gamma) = \epsilon c_0 \left(R(\alpha) - R(\gamma)\right)$. Then, we have

$$\frac{\mathrm{dV}}{\mathrm{dt}} = -\frac{1}{T(\gamma_n)^4} F(\alpha_{n-1}, \gamma_n(t))^T J(\gamma_n(t)) F(\alpha_{n-1}, \gamma_n(t)),$$

where the Jacobian matrix is given by

$$J(\nu) = \begin{pmatrix} (P_1 - T(\nu))P_1' & P_1 P_2' & P_1 P_3' \\ P_2 P_1' & (P_2 - T(\nu))P_2' & P_2 P_3' \\ P_3 P_1' & P_3 P_2' & (P_3 - T(\nu))P_3' \end{pmatrix},$$

with $P_k' = p'(\nu_k) > 0$ (Fig. 1.1C). The matrix J has the following eigenvalues:

$$\lambda_1 = 0, \qquad \lambda_{2,3} = \frac{a \pm \sqrt{a^2 - 4c}}{2},$$

where $a = \sum_{i=1}^3 P_i' \left(T - P_i\right) > 0$ and $c = \sum_{i_1 \neq i_2 \neq i_3} P_{i_1} P_{i_2}' P_{i_3}' > 0$. Thus, $\mathcal{R}(\lambda_{2,3}) > 0$ and hence J is a semi-positive definite matrix in the sense that $\mathrm{dV}/\mathrm{dt} \leq 0$. Therefore, $F(\alpha, \gamma(t)) \to 0$ and consequently the manifold 1.8 is globally stable, which concludes the proof ■

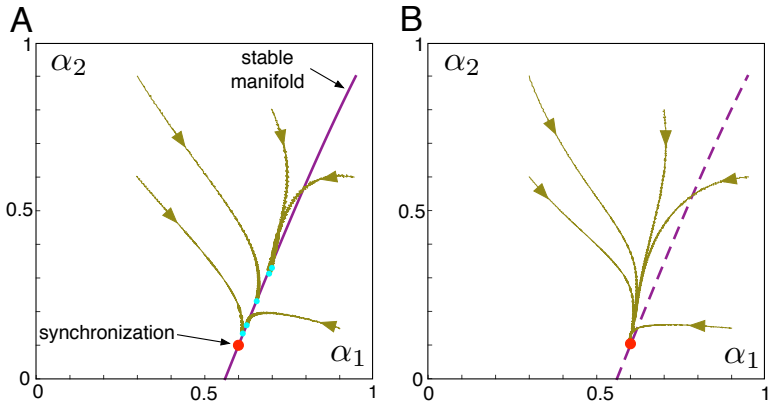

Figure 1.2: Convergence of the learning process. Projection of trajectories of the system (1.6) to the plane (α_1, α_2) is shown. **A)** For $\tau = 0$ there exists a globally stable manifold (purple curve) that attracts all trajectories (cyan circles mark final points). Phase synchronization corresponds to the red point. **B)** For $\tau = 18$ the manifold disappears and all trajectories converge to the red point that warrants synchronization.

The memory time constant τ plays a significant role. Theorem 1.1 shows that the learning process (1.7) converges to a globally stable one-parametric manifold for $\tau = 0$. To illustrate such behavior, we simulated the learning process in a chain of two network motifs: a teacher and a learner.

Figure 1.2A shows five examples of trajectories converging to a stable manifold in the phase space of the learner couplings ($\tau = 0$). For visual clarity, we show the projection to the plane (α_1, α_2). Thus, the learning leads to a mismatch in the connectivity structure, which in turn causes synchronization failure.

Introducing memory in the learning rule ($\tau > 0$), we can achieve exact replication of the coupling structure by the learner. For intermediate values of the memory constant, the previously mentioned manifold is destroyed and the learning process converges to the coupling structure of the teacher [15]. Figure 1.2B illustrates numerical experiments similar to those discussed above, but now for $\tau = 18$. We observe convergence of the coupling strengths to α of the teacher. Consequently, phase synchronization of oscillations in the learner with the teacher is achieved.

1.4. Replication of coupling structure in a chain

In Section 1.2 we discussed synchronization in a chain of two network motifs. Those results can be extended on a chain with arbitrary number of motifs.

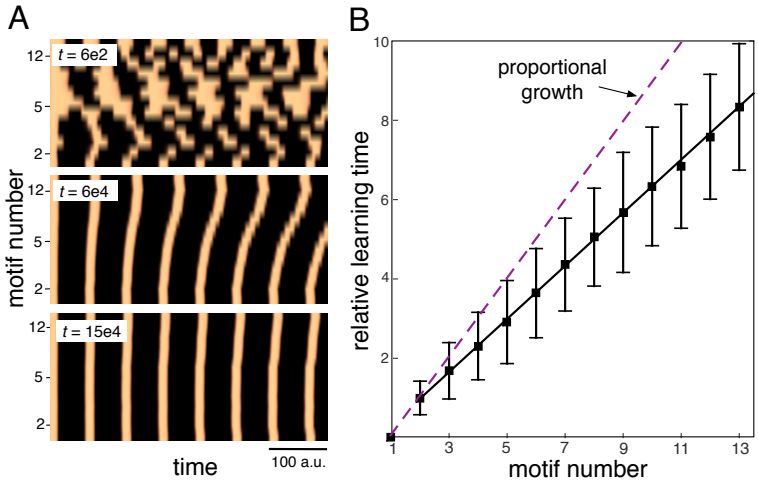

Figure 1.3: Replication of motifs in a chain. **A)** Short epochs of oscillations of the first neuron along the chain of motifs (color corresponds to the value of $x_1(t)$): at the beginning (top), after some time (middle) and at the end (bottom) of learning. **B)** Relative time of learning along the chain T_n/T_1

.

Figure 1.3A shows a representative example of learning in a chain of 13 motifs (to facilitate visual inspection in each panel we set initial phases of all motifs to zero). At the beginning, we set arbitrary $\alpha_n(0)$, $n > 1$, from uniform distribution, and hence we observe completely asynchronous oscillations in the chain (Fig. 1.3A, top). Then, due to learning the coupling strengths converge in a chain to the teacher (first motif) $\alpha_{13} \to \alpha_{12} \to \ldots \to \alpha_2 \to \alpha_1$ (Fig. 1.3A, middle and bottom).

Thus, for intermediate values of the memory constant, τ, all motifs are able to replicate the connectivity structure of the teacher. Moreover, the learning occurs gradually, i.e. more distal motifs require longer time to synchronize their activity with the teacher.

To estimate the synchronization time we performed a Monte Carlo test repeating simulations 20 times with arbitrary initial conditions $\alpha_n(0)$, $n = 2, 3, \ldots, 13$. Figure 1.3B shows the mean relative learning time, i.e. the ratio of the learning time of the n-th motif to the learning time of the first learner. The learning time grows linearly following the low $T_{n+1} = T_n + bT_1$, $n = 2, 3, \ldots$, where $b = 0{,}67$ is the growth ratio. Note that starting from the second motif the replication time is around $2/3$ of the learning time required by the first learner.

1.5. Consensus on a ring of network motifs

We now consider a chain closed into a ring, i.e. the last motif drives the first one (see Figure 1.1A). Then, there is no dedicated teacher and each network motif acts as a local teacher for

the next motif in the ring. In this case, the following result proofs that independently on the initial conditions all motifs come to a state with the same connectivity pattern, corresponding to the mean initial values averaged over all network motifs.

Theorem 1.2

In a ring of network motifs of length $N \geq 2$ governed by the learning process 1.7, for each motif $m = 1, \ldots, N$ we have

$$\lim_{t\to\infty} \alpha_m(t) = \frac{1}{N} \sum_{n=1}^{N} \alpha_n(0), \tag{1.12}$$

independently on the initial conditions $x_n(0)$, $\alpha_n(0)$, $n = 1, \ldots, N$.

Proof of Theorem 1.2. Equation 1.7 with periodic boundary conditions has an integral of motion

$$\frac{\mathrm{d}}{\mathrm{dt}} \sum_{n=1}^{N} \alpha_n(t) = 0. \tag{1.13}$$

Assuming that all couplings α_n converge,

$$\lim_{t\to\infty} \alpha_n(t) = \tilde{\alpha} \quad \forall n = 1, \ldots, N.$$

Thus, together with 1.13,

$$\sum_{n=1}^{N} \lim_{t\to\infty} \alpha_n(t) = N\tilde{\alpha} = \sum_{n=1}^{N} \alpha_n(0)$$

and Eq. 1.12 follows ■

Figure 1.4 illustrates the phenomenon of self-organization in a learning ring of 25 network motifs. Initially the connectivity patterns in all motifs were set random. Then, the learning without leader led to a consensus.

1.6. Conclusions

In this chapter we have proposed a model for learning heteroclinic circuits in networks of neural networks. The model is composed of a teacher and learner networks. At the beginning all networks implement winnerless competition dynamics through wandering around heteroclinic circuits with arbitrary dominant periods. Then, the purpose of learning is to synchronize oscillations in the learner with the teacher by tuning the coupling strengths in the learners.

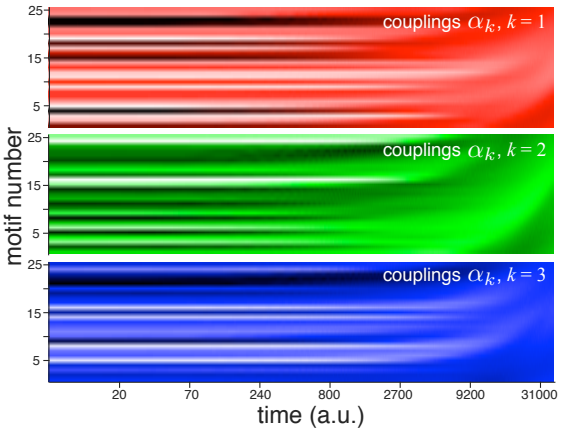

Figure 1.4: Consensus behavior in a ring of 25 network motifs (red, green, and blue colors code the couplings of the corresponding neurons in different motifs).

The information transfer between the networks is implemented through a learning rule that changes local couplings in the learner according to the dynamics of the teacher. Thus, no direct influence of the teacher to the state variables of the learner exists. Instead the learner just "observes" the teacher and tunes itself to replicate the teacher structure. Such a mechanism of synchronization differs significantly from much more common models of synchronization based on couplings among state variables describing the system dynamics [39, 40, 47, 49].

The learning rule proposed in our model includes an integral operator, which implements a memory effect during the learning. We have shown that in the absence of memory the process of learning converges to a point in a stable one-parametric manifold. Existence of the attractive manifold leads to synchronization failure. Nevertheless, for intermediate values of the memory length the manifold can be destroyed and only a single equilibrium point survives, which ensures synchronization.

We have also shown that under appropriate training a chain of learner motifs can progressively "copy" the connectivity pattern of the teacher network motif. In average the time interval required for pattern replication grows linearly with the chain size. Thus, the learning process does not blow up and at the end we observe phase synchronized oscillations along the whole chain of network motifs. Besides, we have shown that in a learning chain closed into a ring the network motifs always come to a "consensus", i.e. to a state with the same connectivity pattern obtained by averaging the initial patterns of all network motifs in the ring. We foresee that the reported mechanism of learning can be useful for replication of scenarios of cognitive navigation in dynamic environments [54].

2 | Learning from demonstration

Learning from demonstration is widely observed in many species. Less experienced agents copy successful behaviors exhibited by more experienced individuals (Fig. 2.1). Nevertheless, the neuronal dynamical mechanisms underlying this paradigm remain largely unknown. While learning, an agent first have to isolate essential motor actions (motifs) from the observed performance, to compose meaningful actions later. In this chapter we propose an approach that allows synthesizing behaviors in a neural network of a learner agent by simply observing the dynamics of a teacher [55].

Figure 2.1: Diferent examples of learning from demonstration in Nature.

The approach first assume that a complex behavior can be decomposed into a sequence of n motor motifs. Then a neural network capable of activating motor motifs in a given sequence can drive an agent. To account for $(n-1)!$ possible sequences of motifs in a small neural network we employ the winner-less competition (WLC) dynamics [14]. We then consider a teacher-learner situation: one agent exhibits a complex movement, while another one aims at mimicking the teacher's behavior. Despite the huge variety of possible motif sequences we show that the learner, equipped with the provided learning model, can rewire "on the fly" its synaptic couplings in no more than $(n-1)$ learning cycles and converge exponentially to the durations of the teacher's motifs.

To validate the model, we tested the algorithm on two robotic platforms (Pioneer 3DX),

one playing the role of a teacher and the other as a learner. Experimental results show that indeed the learner is capable of copying the teacher's behavior composed of six motor motifs in few learning cycles. The reported mechanism of learning is general and can be used for replicating different functions, including, for example, sound patterns or speech.

2.1. Introduction

Social or imitation learning through transferring information from an experienced agent to a naive one is widely observed, especially in primates and humans [56]. It relies on adopting successful actions of others and plays a fundamental role in development and communication. Electrophysiological studies suggest that the so-called mirror neurons take place in imitation learning [22, 23]. Yet the neuronal dynamical mechanisms underlying such a learning remain largely unknown.

Learning a task from scratch, i.e., without any prior knowledge is a complicated problem [57]. Humans rarely attempt to do it. Instead, they usually extract chains of movement primitives from instructions and demonstrations by other humans. Such a paradigm should be also implemented in future completely autonomous robots [58], which will facilitate their social acceptance [59].

While learning, an agent (human or robot) first has to isolate essential *motor motifs* from the movement of another more experienced agent (e.g., "move right", "turn left", etc.). Then it must be able to compose a meaningful behavior from these motifs. Thus, the social learning is an example of a sequential solving of an inverse and then a forward problems. Given n motifs one can build-up $(n-1)!$ different behaviors (e.g., for $n = 10$ we get 362880). At the first glance, such an explosive complexity may appear prohibitive for learning in small neural networks.

Here we present an approach to fast social-like learning of complex motor behaviors from an arbitrary number of motor motifs. It allows synthesizing behaviors in a neural network of a learning agent by observation of the dynamics of a teacher in no more than $(n-1)$ learning cycles. Such a linear (*vs.* factorial) growth of the learning time is reasonable for many applications.

The inverse problem, i.e., the segmentation of complex movements into a sequence of primitives is similar to the problem of discovering network motifs in neural networks [40], which relies on statistical analysis of graphs. To segment movement trajectories Stulp and colleagues [60] proposed to use a clustering method with principal component analysis. However, even in common situations such an approach requires a huge number of demonstrations and may become unfeasible [61]. Another approach reduces the segmentation problem to a sequential recognition of movements and comparing them to a library of motor motifs [62]. Given that the library exists, this approach permits quite efficient sequencing. For the sake

of simplicity, in our work we take a motif library for granted.

The forward problem can be conventionally subdivided into two tasks: 1) implementation of certain motifs (e.g., moving a hand from one point to another [63]), and 2) synthesis of complex behaviors from motor motifs. The first task can be approached by constructing dynamic movement primitives (DMP) [64]. A DMP is given by a dynamical system with a single or multiple attractors and several parameters that are adjusted to account for the trajectory exhibited by an experienced human. The DMP approach is based on the optimal control and in the case of relatively small number of degrees of freedom can be scaled to multiple but similar demonstrations, which produces more flexible solutions [65].

The second task is usually approached from the paradigm of predictive control and optimization of trajectories [66, 67]. We, however, explore the complementary but different question: How can a small neural network reproduce and learn one of $(n-1)!$ behaviors? From the dynamical systems viewpoint the social learning can be reduced to the problem of copying, in terms of synchronization, of ordered in time patterns of neuronal activity from one experienced agent to another, novel one. Although the general "hardwired" architectures of the teacher's and learner's networks can be the same, their intrinsic dynamics defining the activity patterns can differ significantly due to multistability. Then the learner should be able to adjust its network couplings by only observing the teacher dynamics, which leads to synchronization of the behaviors [15].

To tackle the problem here we adopt a use case approach. As a testbed we consider the generalized Lotka-Volterra model with global inhibitory couplings among neurons [14, 15]. Biological neural networks usually exhibit high asymmetry in the coupling patterns [68, 69], i.e., reciprocal connections between neurons i and j may differ significantly. Earlier it has been shown that this can be crucial for establishing temporal associations [70, 71]. It also enables maintaining gaits in locomotion, retrieving ordered items from memory, and codification of information in population bursts [72, 73]. An asymmetric Lotka-Volterra model can exhibit the so-called winner-less competition (WLC) behavior, which occurs in a vicinity of a stable heteroclinic loop connecting saddle equilibriums (see, e.g., [14, 16, 17]). Then, in the presence of a weak perturbation (e.g., noise, for detail see [74] and references therein) a trajectory can wander in the phase space from one saddle to another, thus implementing a particular temporal pattern of neuronal excitation. This provides extremely rich behaviors even in small-size neural networks (see, e.g., [14, 75, 76]).

In this chapter we propose a learning algorithm capable of copying the behavior of one WLC neural network to another. Then we consider a teacher-learner social-like situation. A teacher exhibits a complex behavior consisting of a sequence of motor motifs (one of $(n-1)!$) with specific durations. Another agent, a learner, aims at mimicking the behavior. Despite the behavior complexity grows extremely rapidly with n, we show that the learning algorithm allows the learner to rewire "on the fly" the synaptic couplings in no more than $(n-1)$ learning cycles and to converge exponentially fast to the durations of the teacher's motifs. We then validate the model on mobile robots.

2.2. Motor motifs and behaviors

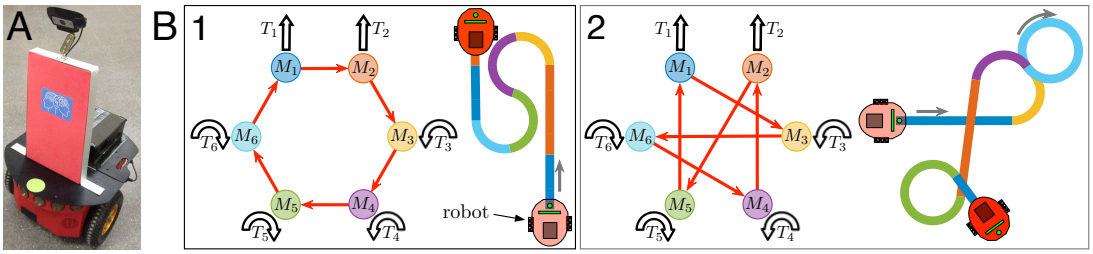

Figure 2.2: Implementation of motor behaviors as sequences of motor motifs. **A)** A Pioneer 3DX mobile robot used in experiments. **B)** Two examples of the robot's behaviors defined by graphs of six motor motifs (see main text). Depending on the order of the motifs and their durations the robot can move along different trajectories (color codifies the active motif).

Our first goal is to provide a neural network architecture that would enable a robot (Fig. 2.2A, for details see [77]) to perform a series of simple motor actions or motifs. Then a complex motor behavior can be "programmed" as a sequence of simple motifs. For illustration we select the following:

$\mathbf{M_1}$: Go straight during time interval T_1.

$\mathbf{M_2}$: Go straight during time interval T_2.

$\mathbf{M_3}$: Turn left during time interval T_3.

$\mathbf{M_4}$: Turn left during time interval T_4.

$\mathbf{M_5}$: Turn right during time interval T_5.

$\mathbf{M_6}$: Turn right during time interval T_6.

For the sake of simplicity, in the description of the motifs we did not specify the linear robot velocity, the radii of turns, etc. These parameters will be essential in Section 2.5. Inclusion of similar motifs (e.g., M_1 and M_2) improves the robot flexibility and complexity of possible behaviors. Note also that the number and variety of motifs can be easily increased (with 6 motifs we can implement up to 120 behaviors).

We can now connect the selected motifs in a graph and thus implement a complex behavior. Figure 2.2B shows two examples of graphs and the corresponding behaviors of the robot. In the first case we selected the cyclic sequence (Fig. 2.2B.1): $M_1 \to M_2 \to M_3 \to M_4 \to M_5 \to M_6 \to M_1 \to \cdots$, which generates a zigzag-like trajectory. In the second case the sequence was (Fig. 2.2B.2): $M_1 \to M_3 \to M_6 \to M_4 \to M_2 \to M_5 \to M_1 \to \cdots$, which generates a more evolved trajectory.

Our second goal is to achieve a social-like learning of behaviors. We thus assign one "more experienced" robot as a teacher. The teacher knows how to reproduce some complex behavior

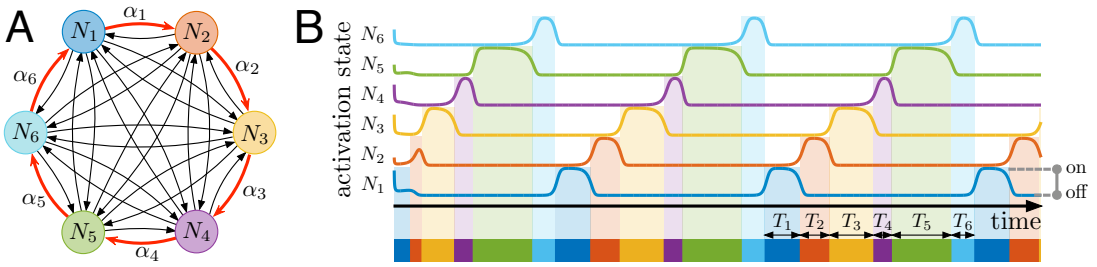

Figure 2.3: Behavior driving neural network. **A)** Schematic representation of the neural network (example for $n = 6$). All neurons (circles) are mutually coupled by inhibitory synapses (black and red links). Red links mark couplings $\alpha = (0{,}6, 0{,}5, 0{,}7, 0{,}1, 0{,}8, 0{,}3)^T$ that define the activation sequence $N_1 \to N_2 \to N_3 \to \cdots$, corresponding to the graph of motor motifs shown in Figure 2.2B.1. The coupling strength of black links is equal to 2. **B)** WLC dynamics generated by the network. Each neuron switches between on (active) and off (inactive) states. Bottom colored stripe shows the activation intervals $T_1, \ldots, T_6$ of the corresponding neurons determined by α.

given by a graph, similar to those shown in Figure 2.2B. Another robot, a learner, at the beginning cannot replicate the teacher's behavior. Its neural network is initialized randomly and hence generates an arbitrary behavior (e.g., go straight or make circles). Then the learner has to learn: 1) the teacher's graph of motifs and 2) the time intervals $T_1, \ldots, T_n$ of all motifs.

2.3. Neural network driving behaviors

Let us now provide a neural network model capable of driving a single robot, i.e., implementing all possible graphs of motor motifs $M_1, \ldots, M_n$ with the corresponding time intervals $T_1, \ldots, T_n$.

We consider a neural network consisting of $n \geq 3$ globally coupled neurons (Fig. 2.3A, $n = 6$). Activation of neuron i during time interval T_i evokes the motor motif M_i and hence the robot performs the corresponding motor action while the neuron stays active. Thus, we separate the physical implementation of each motor motif from the decision-making provided by the behavior driving neural network. This enables employing the same dynamical principles for controlling different platforms and behaviors.

To describe a sequence of motor motifs (Fig. 2.2B) corresponding to a sequence of activations of neurons (Fig. 2.3A), it is convenient to introduce a directed cycle graph $G = (V, E)$ of length $n = |V|$, with the following vertices and edges (circles and red arrows in Figure 2.2B):

$$V = \{1, \ldots, n\}, \quad E = \{(i, j) \in V \times V : \ i \to j\}. \tag{2.1}$$

Then every posible closed circuit of activation of neurons can be defined in terms of the

adjacency or *pathway matrix*:

$$W = (w_{ij})_{i,j=1}^{n}, \quad w_{ij} = \begin{cases} 1 & \text{if } (j,i) \in E \\ 0 & \text{otherwise.} \end{cases} \tag{2.2}$$

In Eq. (2.2) $w_{ij} = 1$ corresponds to a situation when in the motor sequence after motif j goes motif i. Note that $\deg^+(v) = \deg^-(v) = 1$ for all $v \in V$, therefore W is an orthogonal permutation matrix.

There exist $(n-1)!$ different complete cyclic sequences represented by hamiltonian cycles over V. Thus, even in a relatively small graph there can exist a huge number of possible cycles and hence motor behaviors.

To describe the network dynamics implementing sequences of motor motifs, we use the Lotka-Volterra equation generalized to an arbitrary number of neurons $n \geq 3$ [14, 15]:

$$\dot{x} = x \odot (1_n - \rho_\alpha x) + \epsilon\, 1_n, \tag{2.3}$$

where $x(t) \in [0,1]^n$ is the activation state of the neurons resembling their firing rates, $\odot$ stands for the Hadamard product, $1_n = (1, 1, \ldots, 1)^T$, ϵ is a small constant ($0 < \epsilon \ll 1$), and $\rho_\alpha \in \mathcal{M}_{n\times n}(\mathbb{R}_+)$ is the interneuron coupling matrix describing global (all-to-all) synaptic links among the neurons. Moreover, since all elements of ρ_α are positive, the couplings among neurons are inhibitory, i.e., activation of one neuron depresses the activity of the others.

Earlier it has been shown that if the matrix ρ_α satisfies appropriate conditions, then the network exhibits a winner-less competition behavior [52]. In particular, to satisfy the conditions we can set the connectivity matrix to (see [15] for details):

$$\rho_{ij} = \begin{cases} 1 & \text{if } i = j \\ \alpha_j & \text{if } w_{ij} = 1 \\ 2 & \text{otherwise,} \end{cases} \tag{2.4}$$

where $\alpha_j \in (0,1)$. Then in Eq. (2.3) with $\epsilon = 0$, there exists an attracting heteroclinic circuit visiting in a cycle n saddles, each of which corresponding to activation of one neuron [52]. Such a cycle is defined by the pathway matrix W and corresponds to the graph G (Fig. 2.2B). Since the heteroclinic circuit is structurally unstable, any small perturbation ($\epsilon > 0$) leads to an emergence of a stable limit cycle in the vicinity of the destroyed heteroclinic loop, which is the only attractor implementing a WLC behavior.

Figure 2.3B illustrates an example of the WLC dynamics. For the sake of visual clarity we have implemented the simplest excitation circuit: $N_1 \to N_2 \to N_3 \to N_4 \to N_5 \to N_6$ corresponding to the graph shown in Figure 2.2B.1. Loosely speaking, at each time instant only one neuron is on and it inhibits the activity of other neurons until another neuron "switches" on and the process repeats. The duration of the on-state of neuron j is an increasing function of α_j, which tends to infinity if $\alpha_j \to 1$ [15]. Thus, we can individually control the time intervals of all motifs.

Therefore, playing with the pathway matrix W we can select one of the $(n-1)!$ sequences of activation of the neurons (and hence the graph of motor motifs), while choosing $\alpha = (\alpha_1, \ldots, \alpha_n)^T$ we can set the temporal extension of activation for each neuron (and hence the time intervals $T_1, \ldots, T_n$ for all motifs). Thus, the model (2.3) satisfies our needs and offers an extremely flexible way for generating a variety of motor behaviors.

2.4. Fast learning of behaviors in a teacher-learner framework

Let us now consider a social-like situation with two agents: an experienced robot (a teacher) and a naive one (a learner). The teacher has a well-trained neural network (2.3), which allows reproducing some complex behavior (see, e.g., Figure 2.2B). As we have shown in Section 2.3 the teacher's behavior is completely defined by the pathway matrix W_x (subindex x refers to the teacher) and the vector α.

The dynamics of the neural network driving the learner is given by:

$$\dot{y} = y \odot (1_n - \rho_\gamma y) + \epsilon\, 1_n, \tag{2.5}$$

where $y(t) \in [0,1]^n$ is the activation state of the neurons and $\rho_\gamma(t)$ is the coupling matrix with entries $\gamma \in \mathbb{R}^n_+$ [counterpart of α in Eqs. (2.3) and (2.4)]. At the beginning the learner has an arbitrary pathway matrix W_y and the time interval vector γ. Thus, the dynamics of the learner can differ significantly from the dynamics of the teacher. Then the learner's goal is to learn the teacher's behavior and reproduce it.

2.4.1. Learning time intervals

Let us first assume that the learner "knows" the pathway matrix W_x, i.e., the graph of motor motifs of the teacher. However, the time intervals of the motifs $(T_1, \ldots, T_n)$ given by α in the teacher and by $\gamma(t)$ in the learner are unknown. Thus, we have:

$$W_y(t) = W_x, \quad \gamma(0) \neq \alpha. \tag{2.6}$$

Note that the initial values $\gamma(0)$ are taken from a random distribution and we can even have a situation with $\gamma_j(0) \geq 1$ for some $j \in V$. In such a case the WLC conditions are not satisfied and the network evolves to an equilibrium state, and hence the learner either stays still or performs a single motor motif.

The learner aims at replicating the teacher's behavior, i.e., $y(t)$ for $t > t' > 0$ must repeat in some sense the behavior of $x(t)$. To proceed further let us introduce two essential definitions.

Definition 2.1. *Under the learning of a temporal pattern we understand a situation when a learner, sharing the same pathway matrix with the teacher ($W_y = W_x$), independently on*

the initial conditions $x(0)$, $y(0)$, $\gamma(0)$, *can tune its synaptic couplings* $\gamma(t;x)$ *in such a way that*

$$\lim_{t\to\infty}\gamma(t;x)=\alpha. \tag{2.7}$$

We note that condition (2.7) implies that the learner will eventually succeed in reproducing the temporal sequence shown by the teacher:

$$\lim_{t\to\infty}(x(t)-y(t-t^*))=0_n, \tag{2.8}$$

where t^* is some phase lag. This happens because for a fixed (stationary) $\gamma\in(0,1)^n$ the WLC model (2.5) has a single structurally stable attractor. Thus, given (2.7) at $t\to\infty$ the learner and the teacher will have the same stable limit cycle in their phase spaces. Then, the phase lag t^* in (2.8) corresponds to a delay in movement along the limit cycle of the teacher and of the learner.

Definition 2.2. *We say that the learning of a temporal pattern is exponentially fast if*

$$\|\gamma(t)-\alpha\|_2\le Me^{-\kappa t},\quad \forall t\ge 0$$

for some constants $M>0$ *and* $\kappa>0$.

We note that exponential convergence as opposed to mere asymptotic one ensures robustness of the learning process.

Learning rule and exponential convergence

Following the adaptive system approach [78, 79] we now postulate the learning rule:

$$\gamma(t)=\gamma_0+W_y^T(\theta(t)-(x(t)-x_0)), \tag{2.9}$$

where $\theta(t)\in\mathbb{R}^n$ is the control variable obeying:

$$\dot\theta=x\odot(1_n-\rho_\gamma x)+\epsilon\,1_n,\quad \theta(0)=0. \tag{2.10}$$

Note that learning rule (2.9), (2.10) does not depend on the direct knowledge of the teacher's internal parameters α and even of the own behavior of the learner $y(t)$, but it is fully based on the observation of the teacher's dynamics $x(t)$. Thus, the learning can be "mental", i.e., without motor execution.

For further calculations it is convenient to introduce the quadratic term:

$$p(t)=W_y^Tx(t)\odot x(t). \tag{2.11}$$

Then we can formulate the following result.

Theorem 2.1

Under the learning rule (2.9), (2.10), the learner learns exponentially fast any temporal pattern exhibited by the teacher. Moreover, assuming that the teacher exhibits a stable T-periodic pattern (i.e., $x(t+T) = x(t)$), we have the following estimate for the convergence exponent:

$$\kappa = \min\{\langle p_j \rangle\}, \quad \langle p \rangle = \frac{1}{T}\int_{t_0}^{t_0+T} p(t)\,\mathrm{d}t. \tag{2.12}$$

Proof of Theorem 2.1. First let us recall that the common operation of multiplication of matrices has a higher priority then the Hadamard operations. Now deriving (2.9) and using Eqs. (2.3), (2.10) we obtain:

$$\dot{\gamma} = -W^T(x \odot (\rho_\gamma - \rho_\alpha)x). \tag{2.13}$$

Then we observe that $(\rho_\gamma - \rho_\alpha)x = W((\gamma - \alpha) \odot x)$. Substituting this to (2.13) we get:

$$\dot{\gamma} = -W^T x \odot (\gamma - \alpha) \odot x. \tag{2.14}$$

Therefore,

$$\frac{d(\gamma - \alpha)}{dt} = -p \odot (\gamma - \alpha), \tag{2.15}$$

where $p \in \mathcal{C}(\mathbb{R}, [0,1]^n)$, given by (2.11), is a function of time completely defined by the dynamics of the teacher. Integrating (2.15) we obtain:

$$\gamma(t) - \alpha = (\gamma_0 - \alpha) \odot e^{-\int_0^t p(\tau)d\tau}. \tag{2.16}$$

Since $x(t) = 0$ is not a solution of (2.3) and hence $x(t) > 0$ under a WLC dynamics, there exists $\kappa > 0$ such that $p(t) \geq \kappa$, which ensures the exponential convergence: $\|\gamma(t) - \alpha\| \leq \|\gamma_0 - \alpha\| e^{-\kappa t}$. If $x(t)$ is periodic, then a lower bound for κ is given by (2.12) ■

Numerical simulations

Let us now illustrate Theorem 2.1 and the learning abilities of the proposed learning rule. For the sake of visual clarity we built 3-neuron networks for the teacher and the learner. We then assigned three motor motifs: M_1 - move right, M_2 - turn left, and M_3 - turn right. The teacher's sequence of motor motifs was set by selecting the pathway matrix:

$$W_x = \begin{pmatrix} 0 & 1 & 0 \\ 0 & 0 & 1 \\ 1 & 0 & 0 \end{pmatrix}. \tag{2.17}$$

It imposes the motif sequence $M_1 \to M_3 \to M_2 \to \cdots$. The time interval vector was set to: $\alpha = (0{,}2, 0{,}6, 0{,}8)$, i.e., $T_1 < T_2 < T_3$. Then we set the initial values of the learner's couplings $\gamma(0) = (1{,}6, 0{,}1, 2{,}3)$. Note that in this case $\gamma_{1,3} > 1$ and hence the learner cannot exhibit a WLC dynamics at the beginning. We now numerically integrate the model (2.3), (2.5), (2.9), (2.10) and by using $x(t)$ estimate the convergence exponent (2.12): $\kappa = 0{,}0134$.

Figure 2.4 illustrates the learning process. As expected the couplings $\gamma(t)$ converge exponentially to α (Figs. 2.4A, 2.4B). Step-like changes occur when the corresponding component of $p(t)$ goes through its maximum. This happens in time intervals when the excitation passes from one neuron to another. At the beginning the learner does not follow a WLC dynamics, neuron 3 (turn right) stays active for a long time interval (Fig. 2.4C, $0{,}3T \lessapprox t \lessapprox 1{,}8T$, where T is the oscillation period). Nevertheless, once all γ_j enter the region $(0, 1)$ (Fig. 2.4A, $t \approx 1{,}5T$) the learner starts generating a WLC behavior that finally synchronizes with the teacher's dynamics (Fig. 2.4C, $t \gtrapprox 2T$).

Figure 2.4D shows simulations of the robots' movements driven by the neural networks (see also Figure 2.2B). The teacher performs a zigzag movements. Since the time interval T_3 corresponding to motif M_3 (turn right) is the longest, the robot exhibits a tendency to turn right (Fig. 2.4D, teacher). At the beginning the learner has neuron 3 activated (Fig. 2.4C, $0{,}3T \lessapprox t \lessapprox 1{,}8T$) and hence it performs circular movements (Fig. 2.4D, learner). Then, however, it synchronizes with the teacher and replicates its behavior.

2.4.2. Learning a sequence of motor motifs

Let us now consider the general case. At the beginning the learner starts from an arbitrary orthogonal matrix $W_y(0) \in \mathcal{M}_{n\times n}(\{0, 1\})$, such that $W_y(0) \neq W_x$. Then $W_y(0)$ induces a wiring in the graph of motor motifs different from that of the teacher, i.e., $E_y \neq E_x$.

Without loss of generality we can assume that the teacher exhibits a T-periodic dynamics:

$$x(t) = x(t + T), \tag{2.18}$$

with a given pathway matrix W_x and a coupling vector α. Following the derivation similar to the proof of Theorem 2.1 we obtain the following equation describing the dynamics of the learner's couplings:

$$\dot{\gamma} = -p \odot \gamma + q, \tag{2.19}$$

where p is defined by (2.11) and

$$q = W_y^T x \odot \left[2x - (2 - W_y^T W_x \alpha) \odot W_y^T W_x x\right]. \tag{2.20}$$

Then from (2.19) we get

$$\gamma(t) = (\gamma_0 + g(t)) \odot f(t), \tag{2.21}$$

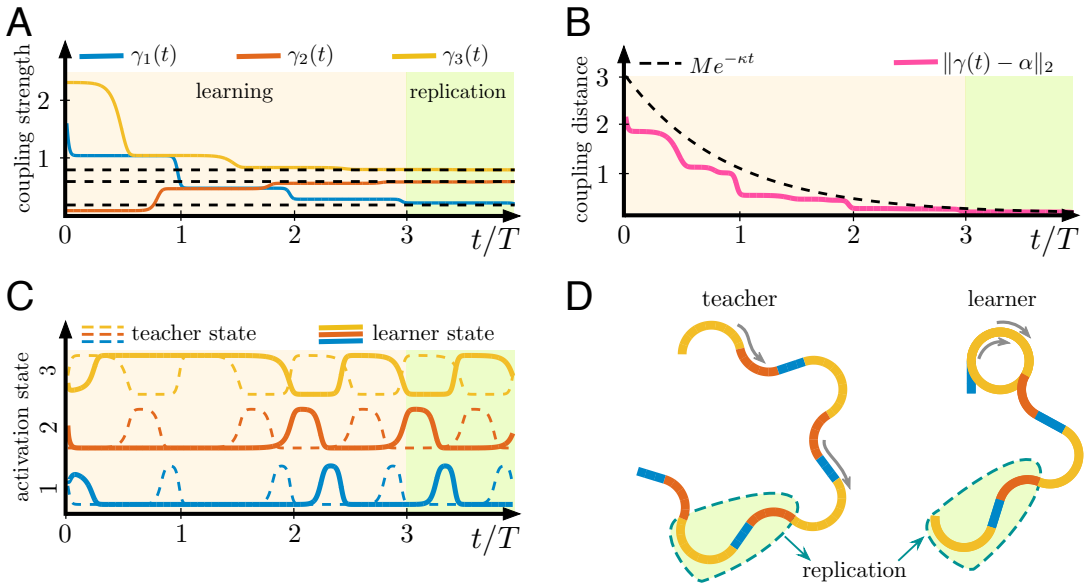

Figure 2.4: Representative example of exponentially fast learning of temporal patterns. **A)** Dynamics of the coupling strengths of the learner, $\gamma(t)$, (solid curves) converging to the corresponding couplings of the teacher, α (dashed lines). **B)** Exponentially fast convergence of the couplings. **C)** Synchronization (with a time shift) of oscillations in the learner with the teacher. **D)** Simulation of the robots' movements. The teacher (left) performs zigzag movements, while the learner (right) at the beginning moves in a circle, but after two learning cycle it starts replicating the teacher's behavior (color coding is the same as in C).

where

$$f(t) = e^{-\int_0^t p(\tau)\,\mathrm{d}\tau}, \quad g(t) = \int_0^t q(\tau) \oslash f(\tau)\,\mathrm{d}\tau, \tag{2.22}$$

where $\oslash$ stands for the Hadamard division. We note that $f(t)$ is a strictly positive function and $\gamma(t)$ does not now converge to α, but oscillates due to $W_y \neq W_x$.

Criterium of successful learning

For a successful learning (Def. 1), the pointwise limit of $\gamma(t+kT)$ (see also (2.33)) for $k \to \infty$ must be equal to α, regardless the value of t. However, in general it is an oscillating function given by (2.21). We then introduce the following mean squared deviations $e_j : \mathbb{R}^2 \to \mathbb{R}$:

$$e_j(\delta) = \frac{1}{2}\Big\langle \big(\delta_1 - (\gamma_j - \delta_2 f_j)\big)^2 \Big\rangle, \quad \forall j \in V, \tag{2.23}$$

where $\delta = (\delta_1, \delta_2)^T$ and $\langle\cdot\rangle$ denotes the time averaging operator over the period T. Note that for a given δ the learner can evaluate (2.23) along the trajectory, i.e., it is an observable variable.

We can now find the minimum of e_j by evaluating the gradient ∇e_j and the Hessian matrix:

$$\mathcal{H}(e_j) = \begin{pmatrix} 1 & \langle f_j \rangle \\ \langle f_j \rangle & \langle f_j^2 \rangle \end{pmatrix}. \tag{2.24}$$

We observe that $\det(\mathcal{H}) = \mathrm{Var}[f_j] > 0$. Thus, e_j is convex and reaches the global minimum at $\nabla e_j = 0$. Solving this equation, we get the coordinates of the minimum:

$$\delta_j^* = \mathcal{H}^{-1} \begin{pmatrix} \langle \gamma_j \rangle \\ \langle \gamma_j f_j \rangle \end{pmatrix} = (\langle \gamma_j \rangle - \beta_j \langle f_j \rangle, \beta_j)^T, \tag{2.25}$$

where $\beta_j = \mathrm{Cov}[\gamma_j, f_j]/\mathrm{Var}[f_j]$. In other words, δ_j^* is composed of the intercept and slope values of linear regression of γ_j over f_j.

Given this observation we can formulate the following result.

Theorem 2.2

Let neuron $i \in V$ be the successor of neuron j in the learner's sequence of motor motifs, i.e. $(j, i) \in E_y$. Then

$$(j, i) \in E_x \Leftrightarrow e_j(\delta_j^*) = 0. \tag{2.26}$$

Equation (2.26) provides a criterium that enables an indirect inferring on the structure of the pathway matrix W_x in the teacher by the learner by evaluating the error $e(\delta_j^*)$. For further calculations it is convenient to introduce two constants:

$$A = f(T) \in (0, 1)^n, \quad B = g(T) \in \mathbb{R}^n, \tag{2.27}$$

where f, g are given by (2.22), and T is the oscillation period of the teacher's pattern. These constants A and B are completely determined by the teacher's dynamics and the pathway matrix of the learner, W_y.

Lemma 2.1

Let T be the period of the teacher's pattern $x(t+T) = x(t)$. Then, under the learning rule (2.19),(2.20) we have

$$\gamma(t + kT) = \gamma(t) - (1_n - A^{\circ k}) \odot (\gamma_0 - A \odot B \oslash (1_n - A)) \odot f(t), \tag{2.28}$$

where $(\cdot)^{\circ k}$ stands for the Hadamard k-th power.

Proof. We notice that $p(t)$ [see Eq. (2.11)] is T-periodic and thus

$$\int_0^{t+kT} p(\tau)\,\mathrm{d}\tau = k\int_0^T p(\tau)\,\mathrm{d}\tau + \int_0^t p(\tau)\,\mathrm{d}\tau.$$

Therefore,

$$f(t+kT) = A^{\circ k} \odot f(t). \tag{2.29}$$

Then, $q(t)$ [see Eq. (2.20)] is also T-periodic, which together with (2.29) yields

$$g(t+kT) = \sum_{l=0}^{k-1} \int_{lT}^{(l+1)T} q(\tau) \oslash f(\tau)d\tau + \int_{kT}^{kT+t} q(\tau) \oslash f(\tau)d\tau = \\ = B \odot \sum_{l=0}^{k-1} A^{\circ -l} + A^{\circ -k} \odot \int_0^t q(\tau) \oslash f(\tau)d\tau. \tag{2.30}$$

Now by substituting (2.29) and (2.30) into (2.21) we get

$$\gamma(t+kT) = \gamma_0 \odot A^{\circ k} \odot f(t) + B \odot \sum_{l=1}^{k} A^{\circ l} \odot f(t) + \gamma(t) - \gamma_0 \odot f(t) = \\ = \gamma(t) - \left((1_n - A^{\circ k}) \odot \gamma_0 - B \odot \sum_{l=1}^{k} A^{\circ l} \right) \odot f(t). \tag{2.31}$$

Finally, since $A \in (0,1)^n$ we can evaluate the geometric series:

$$\sum_{l=1}^{k} A^{\circ l} = A \odot (1_n - A^{\circ k}) \oslash (1_n - A), \tag{2.32}$$

which yields (2.28) ■

Corollary 2.1

Given the sequence

$$\{\gamma(t+kT) : 0 \le t < T\}_{k=1}^{\infty} \subset \mathcal{C}\left([0,T), \mathbb{R}^n\right),$$

there exists a constant vector $C \in \mathbb{R}^n$ such that

$$\lim_{k\to\infty} \gamma(t+kT) = \gamma(t) - C \odot f(t) \quad \forall t \in [0,T) \tag{2.33}$$

Proof. Since $A \in (0,1)^n$, $\lim_{k\to\infty} A^{\circ k} = 0$. Then denoting $C = \gamma_0 - A \odot B \oslash (1_n - A)$ and applying Lemma 2.1 we arrive to (2.33) ■

Proof of Theorem 2.2. On the one hand, given that $(j,i) \in E_x \cap E_y$ and taking into account Eq. (2.16) we get

$$\gamma_j(t+kT) = \alpha_j + (\gamma_j(0) - \alpha_j)\, f_j(t+kT) \tag{2.34}$$

and thus

$$\lim_{k\to\infty} \gamma_j(t+kT) = \alpha_j. \tag{2.35}$$

Then by Corollary 2.1 there exists $C_j \in \mathbb{R}$ such that

$$\gamma_j(t) = \lim_{k\to\infty} \gamma_j(t+kT) + C_j f_j(t) = \alpha_j + C_j f_j(t). \tag{2.36}$$

Thus, by choosing $\delta_j^* = (\alpha_j, C_j)^T$ we obtain $e_j(\delta_j^*) = 0$. This δ_j^* matches the obtained from (2.25).

On the other hand, if $e_j(\delta_j^*) = 0$ then

$$\gamma_j(t) = \delta_{j1}^* + \delta_{j2}^* f_j(t) \;\Rightarrow\; \dot{\gamma}_j(t) = \delta_{j2}\dot{f}_j(t). \tag{2.37}$$

Now, we notice that $\delta_{j2}^*\dot{f}_j = -p_j\delta_{j2}^* f_j = -p_j(\gamma_j - \delta_{j1}^*)$ and thus

$$\dot{\gamma}_j(t) = -p_j(t)\gamma_j(t) + q_j(t), \tag{2.38}$$

where $q_j(t) = p_j(t)\delta_{j1}^*$. Let $l \in V$ be the predecessor of $i \in V$, i.e., $(l,i) \in E_x$. From Eq. (16) we get:

$$q_j(t) = 2p_j(t) + (\alpha_l - 2)x_i(t)x_l(t). \tag{2.39}$$

Now comparing the expressions for q_j we get

$$x_l(t) = \frac{\delta_{j1}^* - 2}{\alpha_l - 2} x_j(t), \tag{2.40}$$

which yields $l = j$, $\delta_{j1}^* = \alpha_j$ and thus the i-th rows of the pathway matrices W_x and W_y are the same ■

Iterative adjustment of W_y

Based on Theorem 2.2 we propose an iterative scheme to adjust the pathway matrix of the learner, W_y. For further calculations, it is convenient to introduce the discrete time k, such that the time-line is divided into intervals:

$$I_k = [(k-1)T, kT), \quad k = 1, 2, \ldots \tag{2.41}$$

We also denote:

$$x_k = x(kT),\ \theta_k = \theta(kT),\ \gamma_k = \gamma(kT). \tag{2.42}$$

The learner starts with a random orthogonal matrix $W_y[0]$ and the time interval vector γ_0. Then in each interval I_k we have the matrix $W_y[k-1]$ that defines the structure of the coupling matrix $\rho_{k-1}(\gamma)$. The dynamics of the learner ($t \in I_k$) is given by:

$$\begin{cases} \dot{y} = y \odot (1 - \rho_{k-1}(\gamma)y) + \epsilon\, 1_n \\ \dot{\theta} = x \odot (1 - \rho_{k-1}(\gamma)x) + \epsilon\, 1_n \\ \gamma = \gamma_{k-1} + W_y^T[k-1](\theta - \theta_{k-1} - x + x_{k-1}). \end{cases} \tag{2.43}$$

We now find δ_j^* using (2.25) and then evaluate $e_j(\delta_j^*)$ from (2.23). By applying Theorem 2.2 (i.e., detecting j such that $e_j(\delta_j^*) \neq 0$) we find edges in the graph G_y that should be rewired (they do not appear in G_x). After rewiring we get new matrix $W_y[k]$. This procedure is repeated for $k = 1, 2, \ldots$. Thereby, we obtain a sequence of the matrices $\{W_y[k]\}$.

Below we will propose an algorithm of the network rewiring that ensures:

$$W_y[k] = W_x \quad \forall k \geq k^* > 0, \tag{2.44}$$

where $k^* < n$, i.e., the number of steps required to find W_x grows no more than linearly with the number of motor motifs, n. Thus, the learner can learn rapidly the pathway matrix of the teacher. Then, according with Theorem 2.1, the learner also learns the time interval vector α exponentially fast.

2.4.3. Learning algorithm

Summarizing the above mentioned results we propose the following algorithm of learning.

$\mathbf{S_0}$: Initialize the parameters: 1) Select the initial permutation $\sigma : V \to V$, $\sigma = (1, 2, \ldots, n)$; 2) Select random γ_0; 3) $\theta_0 \leftarrow 0$; 4) $k \leftarrow 0$; 5) $\Omega \leftarrow V$.

$\mathbf{S_1}$: While $\Omega \neq \emptyset$ repeat:

1. $k \leftarrow k + 1$
2. Set $W_y[k-1] = (w_{ij})_{i,j=1}^n$, where

$$w_{ij} = \begin{cases} 1 & \text{if } \ i = \sigma(j) \\ 0 & \text{otherwise} \end{cases} \tag{2.45}$$

3. Integrate (2.43) over I_k by using the coupling matrix ρ_{k-1} given by $W_y[k-1]$.
4. Find δ_j^* and $e_j(\delta_j^*)$ from (2.23)–(2.25).

5. Set $\Omega = \{j \in V : e_j(\delta_j^*) \neq 0\}$ and label its elements in ascending order $\Omega = \{\omega_1, \ldots, \omega_m\}$, with $\omega_k < \omega_{k+1}\ \forall k < m$.
6. For each $i \in \{1, \ldots, m\}$ update the permutation $\sigma(w_i) \leftarrow \sigma(w_{i^+})$, where

$$i^+ = \begin{cases} i+1 & \text{if } i < m \\ 1 & \text{if } i = m \end{cases} \tag{2.46}$$

$\mathbf{S_2}$: Using the last W_y (note, that now $W_y = W_x$) apply the learning rule (2.9), (2.10) for $t \geq kT$.

The learning time of the proposed algorithm is given by the following theorem.

Theorem 2.3

The iterative learning process described at step $\mathbf{S}_1$ of the algorithm converges in $(n-1)$ iterations at most.

Proof of Theorem 2.3. First we note that the cardinality of the graph is $|G| = n$. Thus, each vertex of degree 1 can be connected to only one of $(n-1)$ vertices.

Now we observe that at each learning cycle the changes in σ (item 6) induces a rewiring in the network that takes into account the ascending order established in Ω (item 5). This method ensures an exhaustive sequential search: each vertex tests all possible connections (at most, $n-1$) through different edges in the graph. Once the tested successor matches the teacher's network, the node will be excluded from Ω at the next step, after evaluating the corresponding e_j function (item 4) ■

Thus, the learning time grows linearly with the number of neurons, while the number of possible behaviors grows extremely fast, as factorial.

Let us now illustrate the algorithm numerically. We built two neural networks with 13 neurons each (a teacher and a learner) and selected a random pathway matrix, W_x, for the teacher. Then we initialized the learner (step $\mathbf{S}_0$) and started the algorithm. Figure 2.5 illustrates the process of learning of the connectivity matrix W_y (step $\mathbf{S}_1$).

At the beginning there exists $4{,}79 \times 10^8$ possible graphs of the motor motifs (panel "all possible connections"). At the first iteration (lasting one period of the teacher's behavior) the learning algorithm identifies that the link going from neuron 7 to neuron 8 exists in the teacher, while the others defined by $W_y[0]$ do not (Fig. 2.5, Iteration 1). Thus, we keep the link $7 \to 8$ and change the others ($\mathbf{S}_1$, item 6 of the algorithm). Then a new wiring is set up and we repeat the calculations over the second period of the teacher's behavior. Within Iteration 2 the learner find two more correct links: $10 \to 12$ and $3 \to 5$ (Fig. 2.5, Iteration 2).

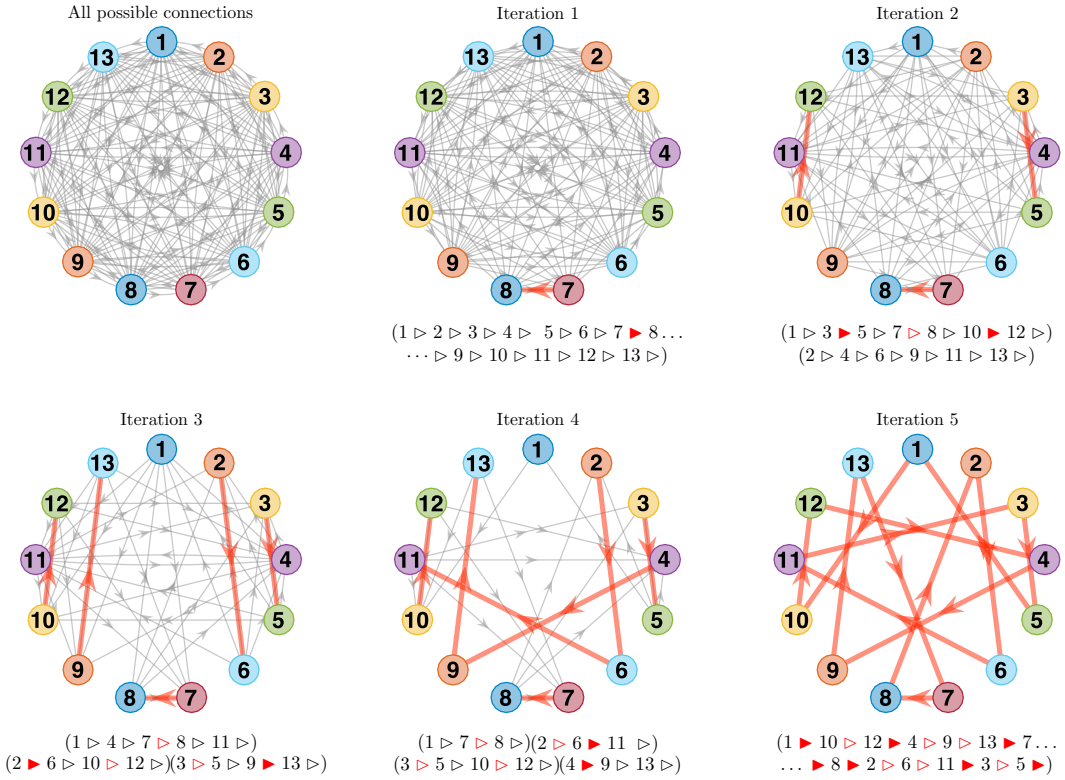

Figure 2.5: Representative example of dynamical learning of the teacher's graph $1 \to 10 \to 12 \to 4 \to 9 \to 13 \to 7 \to 8 \to 2 \to 6 \to 11 \to 3 \to 5 \to \cdots$ defining the sequence of motor motifs in the teacher's behavior. First panel shows in gray all possible connections. Iterations from 1 to 5 show correctly identified connections in red and the remaining ones in gray. A legend below each panel shows the learner's graph. Filled red triangles correspond to newly identified connections, open red triangles mark previously identified connections, and open black traingles label wrong connections.

In the following three iterations the learner gets to learn all connections $1 \to 10 \to 12 \to \cdots$. Thus, it was able to learn the teacher's sequence out of $4{,}79 \times 10^8$ possible cases in only five iterations or demonstrations of the teacher's behavior.

Then in step $\mathbf{S}_2$ the time intervals of the motor motifs (the values of γ) converge exponentially (Theorem 2.1). Note that this process does not depend on the number of motifs. Thus, the time interval required to learn a complex motor behavior grows linearly with the complexity of the behavior (i.e., with the number of motifs).

2.5. Experimental validation

Let us now test experimentally the proposed learning model. We equipped two robotic platforms (Pioneer 3DX, Adept Mobilerobotics, linear sizes l×w: $45{,}5 \times 38{,}1$ cm, Fig. 2.2A) with

neural networks consisting of $n = 6$ neurons. The network dynamics had been implemented in Matlab (Mathworks) running on an on-board Intel NUC PC connected to the platform through a COM interface. One platform played the role of a teacher (with a predesigned complex motor behavior), while the other one was designated as a learner with the driving network randomly initialized.

In both platforms we implemented six motor motifs provided in Section 2.2. The linear robot velocity was set to 10 cm/s and the radii of turns to 17 cm. These parameters were chosen to fit the robot's behavior within the available arena (8×3.5 m). During all experiments the robots' behavior was recorded by a wide-angle zenithal USB camera. The geometric distortions of the actual position of the robots in the arena (due to projection) were corrected by applying an appropriate transformation.

The neural network dynamics of the teacher has been translated into motor commands by

$$i(t) = \arg\max\{x_j(t)\}_{j=1}^{6}, \tag{2.47}$$

where $i(t) \in \{1, 2, \ldots, 6\}$ is the number of the motor motif performed by the robot at time instant t. The same mechanism has been used to drive the learner.

The pathway matrix W_x, defining the coupling matrix ρ_α, and hence the sequence of the motor motifs of the teacher, was selected such that it reproduced the graph shown in Figure 2.2B.2 (i.e., $M_1 \to M_3 \to M_6 \to M_4 \to M_2 \to M_5$). The values of α were set in such a way that the durations of the motor motifs were $T_1 = 7{,}0$ s, $T_2 = 7{,}1$ s, $T_3 = 4{,}1$ s, $T_4 = 4{,}1$ s, $T_5 = 9{,}4$ s, $T_6 = 11{,}0$ s. Then, during one period $T = \sum T_i = 42{,}7$ s the teacher exhibited a behavior similar to that shown schematically in Figure 2.2B.2. Figure 2.6A shows the teacher's trajectory corresponding to five repetitions of the motor pattern. The robot repeats the behavior shown in Figure 2.2B.2 and produces a complex "flower"–like trajectory (Fig. 2.6A).

The neural network of the learner was initialized at random (W_y and γ were arbitrary chosen). Then the learning algorithm (Sect. 2.4.3) has been activated and the robot started moving. Figure 2.6B shows the robot trajectory. At the beginning the robot performed quite chaotic movements, only partially reproducing the teacher's motor pattern. However, after three periods the learner was able to capture completely the pathway matrix W_x (i.e., $W_y(t) = W_x$ for $t > 4T$) and started repeating the teacher pattern quite reliably. Then, the values of γ were also tuned (exponentially fast) and finally the learner was able to reproduce the teacher's behavior faithfully.

To quantify the difference between the trajectories performed by the robots we introduced the following metric:

$$D(t) = \min_{\tau \in [0,T]} \left[\frac{1}{T} \int_{t-T}^{t} |c_T(s) - c_L(s-\tau)|^2 \, \mathrm{d}s \right]^{\frac{1}{2}}, \tag{2.48}$$

where c_T and c_L are the curvatures of the teacher's and learner's trajectories, respectively,

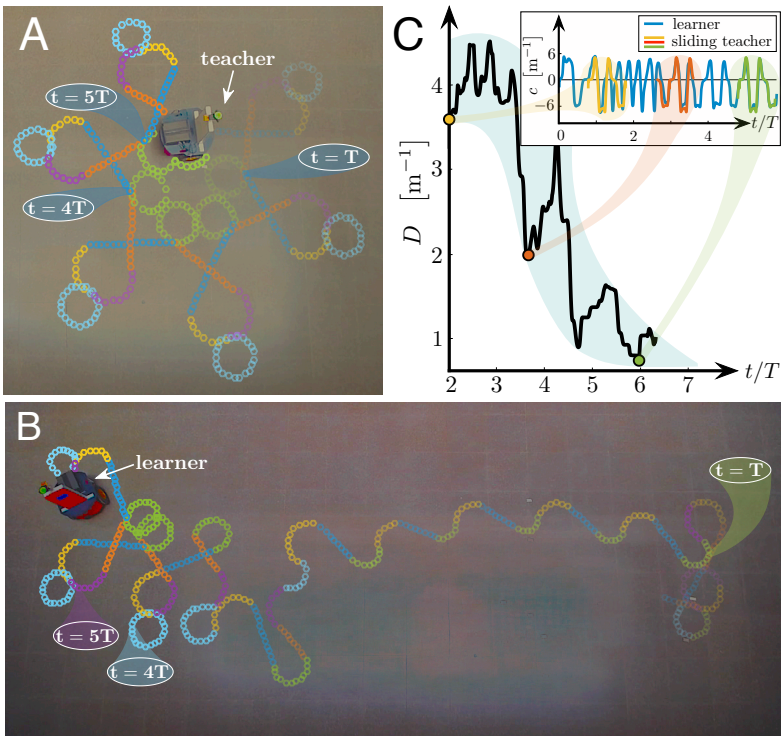

Figure 2.6: Experimental validation of learning. **A)** Robot-teacher implements the behavior composed of six motor motifs shown in Figure 2.2B.2. The brightness of colors corresponds to time (the brighter, the closer to the present). **B)** Trajectory of the robot-learner. At the beginning it differs significant from the teacher's behavior. However, in only three cycles the robot learns the sequence of turns and then two more cycles are needed for final adjustment of the coupling strengths. Eventually the learner replicates almost exactly the behavior of the teacher. **C)** Quantification of the learning error (2.48), defined as the distance between trajectories of the teacher and learner. Inset illustrates the trajectory curvature of the learner (blue curve) with superimposed curvatures of the teacher in three time windows marked by circles of different colors. The level of coincidence increases with time.

evaluated by:

$$c(t) = \frac{\tilde{x}'(t)\tilde{y}''(t) - \tilde{y}'(t)\tilde{x}''(t)}{(\tilde{x}'(t)^2 + \tilde{y}'(t)^2)^{3/2}}, \tag{2.49}$$

where $(\tilde{x}(t), \tilde{y}(t))$ is the parametric robot trajectory captured by the video camera. Since the linear robot velocity is constant, curvature (2.49) describes uniquely the robot trajectory on a 2D plane. We also note that the metric (2.48) is invariant with respect to the translational and rotational symmetries, and the phase lag in the learner [see Eq. (2.8)]. Thus, the introduced metric fulfills all requirements for a distance measure between two trajectories.

Experimentally acquired trajectories are not precise due to a number of reasons, starting form errors in the odometry [77], identification of the robot position, and ending by the distortions produced by the camera. Thus, to evaluate the metric (2.48) we upsampled the

trajectories shown in Figures 2.6A and 2.6B and denoised the data by a continuous wavelet approach [80]. Figure 2.6C shows the dynamics of the distance between the trajectories of the teacher and the learner. As expected the distance strongly oscillates at the beginning due to rewiring and changes of γ, but then decreases and approaches a stationary level, defined by measurement and motor noise. Thus, the learner robot can indeed adapt "on the fly" the wiring of its decision-making network and mimic the movements of the teacher.

2.6. Conclusions

Cognitive learning of motor behaviors is a complicated problem even for humans. In this work we have proposed an efficient mechanism for dynamical learning in neural networks. In a social-like situation a teacher (mobile robot in experiments) can exhibit a complex behavior consisting of a sequence of n motor motifs (simple motor actions). There exists $(n-1)!$ motif combinations. Moreover, all motifs have specific durations that also play an important role in formation of the final motor pattern. Thus, the complexity and variety of the behaviors available to an agent grow extremely rapidly with n. This posses two problems: 1) How can a small neural network implement such a variety of different behaviors? and 2) How can a learner (i.e., another neural network) copy the unique behavior of the teacher starting from random initial conditions?

To implement a motor behavior (e.g., to drive a robot-teacher) we have proposed to link n neurons with n motor motifs. Then an excitation of a given neuron evokes the execution of the corresponding motif. This approach allows separating the "behavioral" neural network from the motor executive part. Thus, the network dynamics does not depend on specific motor motifs and physical properties of the agent, and hence can be easily transferred to other technical devices. To avoid contradicting commands in such an architecture, two neurons cannot be activated simultaneously. This property has been achieved by employing the winner-less competition paradigm [14, 16].

Using the motor motif approach a learner has to solve two tasks: 1) Find the teacher's graph of motifs (i.e., the pathway matrix), and 2) Adjust the durations of motifs (i.e., the coupling strengths). To deal with the second task earlier we provided a neural network model that enabled learning of the activation times [15, 46]. However, to reproduce the teacher's behavior it was necessary to begin simulation from appropriate initial conditions (although rather general). Besides, the learning required long time. Here we have introduced a novel learning rule and proved its exponentially fast convergence independently on the initial conditions (Theorem 1). We note that the learning rule does not depend on the learner's state variable. Thus, during the learning the motor implementation of the behavior is not necessary. Therefore, the agent can simply "observe" the teacher without moving itself. Such a "silent" learning can be observed in humans and also in artificial cognitive agents [54].

The learning of the pathway matrix is based on the dynamic evaluation of the fitness of the

interneuron couplings over the learner's trajectory. We have provided a rigorous approach (Theorem 2) that enables network rewiring "on the fly". Such a rewiring requires at most $(n-1)$ iterations of the algorithm for the complete convergence (Theorem 3). Thus, the learning time grows only linearly with the number of motor motifs. In a numerical simulation with networks of $n = 13$ neurons we observed that the learner could find the teacher's pathway matrix (one out of $4{,}79 \times 10^8$ possible) in five steps only.

Thus, the provided approach enables fast learning in social-like situations. To validate it, we tested the algorithm on mobile robots. First, we implemented six motor motifs (go straight, turn left, etc.) as executable commands. These motifs can be considered as "genetically" programed primitives available to a roving robot. Then we implemented neural networks in two robots and designated one of them as a teacher and the other as a learner. The teacher has been programed to reproduce a complex flower-like trajectory, while the learner was set at random. Then the learner started to learn the teacher's trajectory. At the beginning its movements were quite chaotic. However, after few cycles the learner has successfully "copied" the teacher's behavior.

The reported mechanism of learning is quite general and can be used for replication of different behaviors on different platforms. Moreover, the behaviors need not to be motor. For instance, one can also think about replication of sound patterns or speech. It may also serve as a linker connecting different scenarios and behaviors during cognitive navigation [81].

3 | Navigation in time-changing environments: The time compaction

Evolution has shaped living beings under a single premise: survival. In particular, the nervous system and, ultimately, the brain have been developed to provide animals and humans with the capability of interacting with complex dynamic environments by allowing them to make sophisticated decisions in real time, e.g. when a prey needs to avoid a predator or when someone drives a car in the traffic. This ability is paramount for survival but, paradoxically, the neural mechanisms and functional processed supporting it are poorly understood.

The Prediction for CompAction (PfCA) paradigm postulates that dynamic situations are internally represented in the brain as static representations, removing temporal information by predicting and spatially structuring the possible interactions in the environment [81]. The recently introduced concept of Compact Internal Representation (CIR) offers static abstractions of the external world, called Generalized Cognitive Maps (or GCMs), for description of time-changing scenarios.

In this chapter we discuss implementation of a neural network that permits generation of GCMs. We present the application of this neural network to robot navigation in simulated time-evolving environments. Thus we show that this CIR-based network provides the agent with a reliable, fast, and flexible manner for dealing with dynamic situations.

3.1. Introduction

In the last decades diverse experimental findings provided insight into the neural mechanisms of cognition involved in interaction with *static* scenarios. It has been shown that animals for navigation in space use abstract representations of the environment named cognitive maps [82, 83]. The cognitive maps act as a GPS, containing critical information for understanding the perceived space, as subject location (place cells), objects obstructing free ways (boundary

cells) and space metric (grid cells), but also about how to move through such space [84]. This concept has been successfully applied to robotics for supporting cognitive navigation but mostly limited to static environments [20, 85].

However concerning cognition in time-changing scenarios, growing experimental evidence suggests that the neural structures generating cognitive maps (e.g. the hippocampus and medial prefrontal cortex) also participate in representation of dynamic situations. For instance, place cells coding the subject's position in space also encode speed, turning angle, and direction of moving objects [86]. At larger scale, chemical damage of the rat hippocampus impairs avoidance of moving obstacles, with no effect on other critical abilities [87]. Thus, in mammals, cognition of dynamic situations is built over cognitive maps and involves global network activity of entire brain areas.

Following experimental insight adaptive artificial cognitive maps partially solve the problem of internal representation of dynamic environments. However, their straightforward application may lead to explosive growth of the required calculation power (see e.g. [54] and references therein).

In order to generalize the cognitive maps to dynamic environments, here we propose an alternative approach, called Prediction-for-CompAction (PfCA) [7, 81]. PfCA postulates that when we process a dynamic situation our brain does not explicitly code the time dimension, but it extracts from the spatiotemporal information those critical events required for dealing with such situation (Fig. 3.1) and projects them to a static (spatial) map named Generalized Cognitive Map.

In the context of navigation, these critical events will be the possible collisions with obstacles, so according to PfCA our brain evaluates where such collisions could occur and transform them into *effective obstacles*, which are then structured as a Generalized Cognitive Map (GCM). It should be remarked that 1) in the ordinary cognitive maps the obstacles are real since the scenarios are static, and 2) in these static environments the GCMs are naturally reduced to the cognitive maps [7]. Therefore the GCMs would have the same properties than cognitive maps but for dynamic situations, so they would act as a dynamic GPS, providing us with the information required to understand a time-changing situation but also to interact with it (e.g. providing navigation trajectories).

3.2. Cognition through generalization of cognitive maps

Neural network implementation of cognition of static and dynamic situations may differ significantly. Nevertheless, the concept of compact internal representation (CIR) provides an elegant way to unify descriptions of both static environments and dynamic situations [7]. In this Section we conceptually address the problem of how cognition may emerge in a bio-inspired neural network and introduce the notion of Generalized Cognitive Maps.

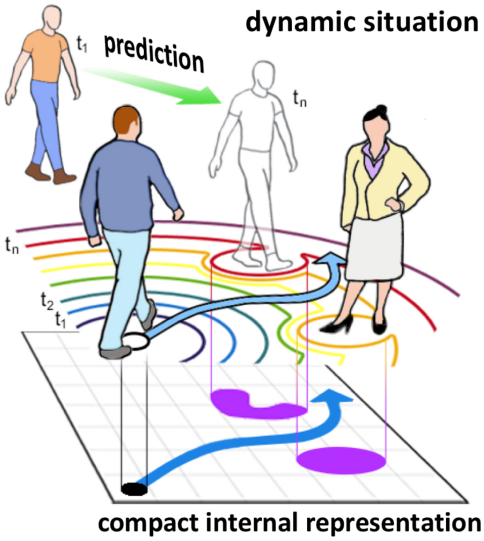

Figure 3.1: Prediction-for-CompAction paradigm as a cognitive basis for generating behaviors. The compact internal representation (CIR) is a static map containing the relevant information to cope with a dynamic situation. For instance, to walk safely in a crowd, the subject (forefront) predicts the behavior of the other pedestrians and simulates his own movements. Colored curves mark possible subject's positions at times $t_1, t_2, \ldots t_n$. Coincidences between such subject's virtual positions and the predicted locations of both moving and immobile pedestrians, correspond to potential collisions, represented as virtual static obstacles in the CIR (purple areas). Avoidance of such static obstacles ensures collision-free walking in the real dynamic situation (blue arrowed curves). Note, from the representation of the standing woman, that a static scene will be straightforwardly coded by its corresponding CIR.

3.2.1. Cognitive maps for static environments

Let us consider a situation sketched in Figure 3.2A. A walking humanoid agent comes across two obstacles: a human and a chair. The human and the chair stay immobile and therefore the agent is in a *static environment*. Then the navigation can be fulfilled by using standard cognitive maps (see e.g. [20]). A neural network implementation of this general concept is provided in [7].

In real space the chair occupies some space whereas the agent and the human are represented by their personal areas [88] (Fig. 3.2B, left panel). To represent "mentally" the real space we now introduce a 2D neural network, an $(n \times n)$-lattice of locally coupled neurons (Fig. 3.2B, right panel). This, so-called Causal Neural Network (CNN, Section 3.3.2), receives as an input the spatial configuration of the real space. In the network space

$$D = \{(i, j) : \quad i, j = 1, 2, \ldots n\} \tag{3.1}$$

the agent is reduced to a single neuron, while its dimension is properly added to the obstacles' dimensions, thus proportionally increasing their sizes [89].

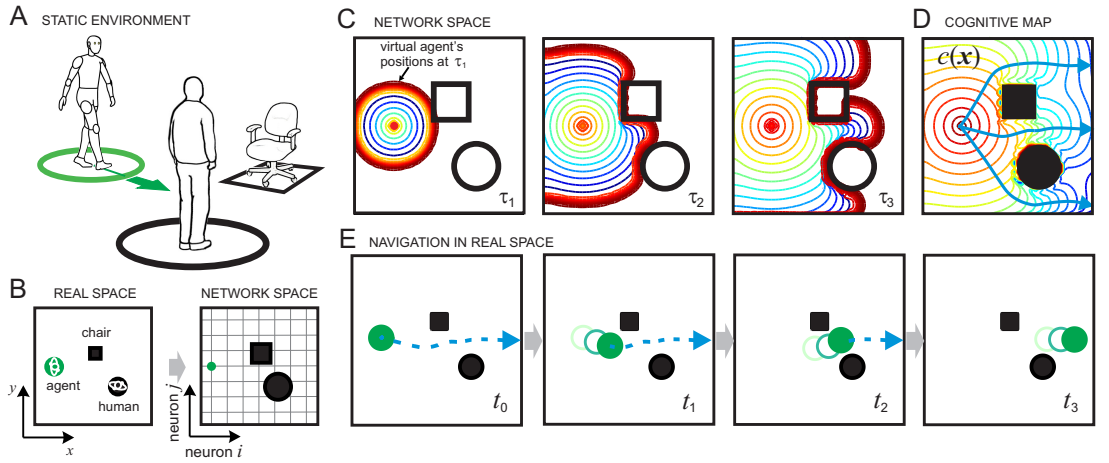

Figure 3.2: Cognition through GCMs in a *static environment*. **A)** A humanoid agent (green circle) walks avoiding collisions with a static human (black circle) and a chair (black square). **B)** The situation is mapped from the real space (left) to the network space (right) described by a 2D neural lattice. **C)** A wavefront propagating in the lattice simulates multiple agent's trajectories (three snapshots at mental time $\tau = \tau_{1,2,3}$). The front explores the environment and creates a gradient profile. **D)** Final cognitive map with effective obstacles (in black). Going up the gradient the agent can reach the target avoiding obstacles (blue arrowed lines). **E)** Example of navigation. The agent follows one of the possible trajectories (superimposed frames with increasing green intensity correspond to progressively increasing time instants).

In the network space D the agent has to create a cognitive map of the environment. It is fulfilled by virtual simulation of all possible agent's movements using a wave process. Since the agent can walk in any direction, its virtual positions (locations occupied by virtual agents) at the next time step will form a circle with the agent in the center (Fig. 3.2C). The radius of this circle will grow with time as virtual agents will move away from the center. Thus, the process of mental exploration of the environment can be described by a solitary wave propagating in the network outward the agent's initial position. The wavefront detects all obstacles, rounds them, and hence finds possible paths among them. We note that this is achieved efficiently, in one run independently on the complexity of the environment.

Each neuron (i, j) records the time instants c_{ij} when the wavefront passes through it. Thus, we create a 2D potential profile

$$c : D \to \mathbb{R} \tag{3.2}$$

or a cognitive map (Fig. 3.2D, contour curves). Going up the gradient ∇c (transversally from red to blue curves) the agent can follow one of the virtual trajectories (Fig. 3.2D, blue arrowed curves). These trajectories ensure collision-free walking in the real space. Figure 3.2E illustrates one of the possible ways of navigation in this static environment.

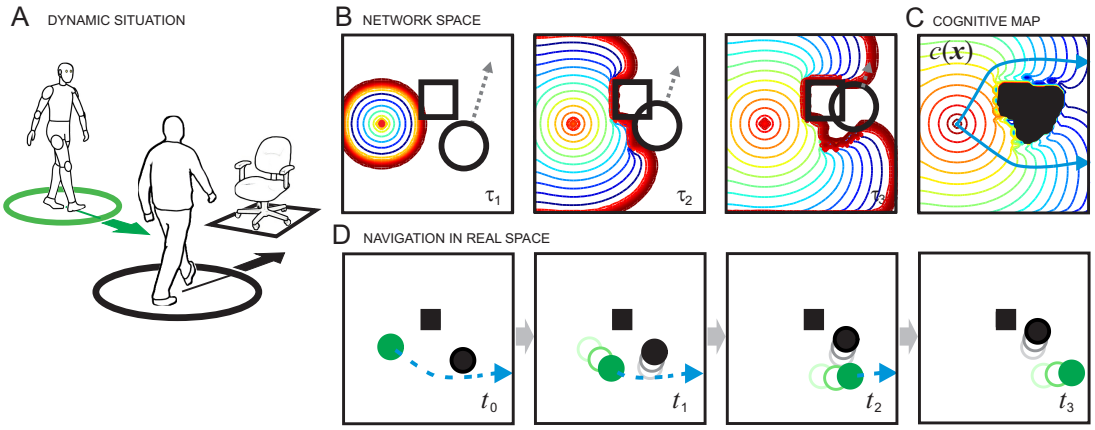

Figure 3.3: Cognition through GCMs in a *dynamic situation*. **A)** Same as in Figure 3.2A, but now the human walks towards the chair. **B)** Simulation of the agent's movements (wavefront) and matching them with obstacles' movements (human's trajectory, dashed line, is predicted by the TMNN). Collisions of the wavefront and virtual obstacles produce effective obstacles. **C)** Compact cognitive map (the time dimension has been compacted) with static effective obstacle (black). Going up the gradient (blue arrowed curves) ensures collision-free walking. **D)** Agent navigating in the real space.

3.2.2. Cognitive maps for dynamic situations

Figure 3.3A sketches a situation similar to that considered in Figure 3.2A. However, now the human is going towards the chair and therefore the agent is in a *dynamic situation*, which challenges standard cognitive maps.

The core of the Prediction-for-CompAction paradigm relies on two basic elements:

- Prediction of the movements of objects
- Simulation of all possible agent's trajectories

A special neuron network matches these processes and generates a GCM. Functionally this map is equivalent to a standard cognitive map, i.e. it is a static structure given by Eq. (3.2), which allows for tracing collision-free trajectories.

Prediction of object trajectory

To predict trajectories we use a dynamic memory implemented in a so-called Trajectory Modeling Neural Network (TMNN, see Section 3.3.1) [7, 8].

A trajectory of a moving object (e.g. of the human in Figure 3.3A) is a function of time $s : \mathbb{R} \to \mathbb{R}^2$ that can be approximated by a polynomial (similar to the spline method used

by [90]):

$$s(t) \approx s(0) + s'(0)t + \frac{s''(0)}{2}t^2. \tag{3.3}$$

The TMNN predicts future object's locations, $\tilde{\vec{s}}$, by iterating a linear map $(W^k \vec{s}_0)_{k\in\mathbb{N}}$, where W is a matrix describing couplings among neurons and $\vec{s}_0 = (s(0), s'(0), s''(0))^T$ is the vector of initial momenta of the object (i.e. position, velocity, and acceleration). Then

$$\tilde{\vec{s}} = \tilde{\vec{s}}(\tau; \vec{s}_0) \tag{3.4}$$

is the trajectory in the network space D and mental time $\tau = kh$, where h is the time step and $k \in \mathbb{N}$.

For correct predictions the TMNN must be trained, i.e. the connectivity matrix W must be properly tuned [7]. Once the learning is finished, the TMNN is ready to predict the movement of objects solely based on their positions acquired by the sensory system at the present ($t = 0$) and two time instants in the past ($t = -2h$ and $t = -h$). Such predictions are quite robust against sensory noise [54].

Simulation of agent's movements and matching them with predicted trajectories of objects

As in the static case the CNN simulates all possible movements of the agent by a wavefront (Fig. 3.3B). However, since now the human moves in the environment, his trajectory $\tilde{\vec{s}}(\tau)$ is predicted by the TMNN and expected future positions are fed to the CNN (compare Figures 3.2C and 3.3B). Collisions of the wavefront and virtual objects in the network space correspond to possible collisions of the agent with objects in the real space. In the CNN these locations delimit effective obstacles (Fig. 3.3B; Appendix 5.4.3).

Once the network space has been explored, the dynamic situation is represented as a static map (Fig. 3.3C):

$$c = c(\vec{x}; \tilde{\vec{s}}), \quad \vec{x} \in D \tag{3.5}$$

The mobile (human) and immobile (chair) objects are replaced by the corresponding effective obstacles (joint black area). The gradient profile (contour curves from red to blue) contains a virtually infinite set of pathways that can be followed by the agent (Fig. 3.3C shows two representative examples):

$$\vec{d} = \vec{d}(\vec{x}; \nabla c) \tag{3.6}$$

Note that by simply avoiding static effective obstacles in $c(\vec{x})$ the agent avoids collisions with the human and the chair. Thus, the selected trajectory can be converted to motor actions and the agent can navigate in the real space following the corresponding path, $d(t)$, (Fig. 3.3D).

Generalized cognitive maps extend the traditional concept of cognitive maps to time-changing situations. They compress spatiotemporal information about what and where may happen

into static structures. The decision-making scheme can be represented as a unidirectional chain:

$$s(t) \;\text{—}\; \tilde{\vec{s}}(\tau) \;\text{—}\; c(\vec{x}) \;\text{—}\; \vec{d}(\vec{x}) \;\text{—}\; d(t) \tag{3.7}$$

We note that at first glance the situation presented in Figure 3.3A may be considered delusively simple. Some geometric-based methods could provide solutions to this path planing problem [18]. However, in the presence of several moving objects the problem becomes practically unsolvable for geometric algorithms or they would provide suboptimal solutions. Indeed, any trajectory deviation caused by avoidance of the first obstacle will induce changes in the configuration of possible collisions with the second obstacle, etc. Thus, the calculation diverges. Nevertheless, our neural network approach efficiently resolves navigation problems of practically arbitrary complexity[1].

3.3. Neural networks implementing time compaction

As briefly explained in the previous section, a GCM is generated by a causal neural network (CNN) that receives as an input locations of all objects in the arena predicted by the trajectory modeling neural network (TMNN). The joint network dynamics forms effective static elements (e.g. effective objects) and a potential field c in the network space D, which constitute a generalized cognitive map. Then the map can be used to trace trajectories to a target (including moving). We note that any object or place in the environment can be assigned as a target.

3.3.1. Trajectory Modeling Neural Network

The TMNN implements a dynamic memory [53]. It models object trajectories by quadratic polynomial (see Eq. (3.3)). Then in 2D space we have two components $s(t) = (x(t), y(t))$ modeled by two TMNNs. Each TMNN consists of three recurrently coupled neurons with external input $\xi(k) \in \mathbb{R}^3$ and output $\eta(k+1) \in \mathbb{R}^3$, where $k = 0, 1, 2, \ldots$ is the discrete *mental* time [7]. The TMNN dynamics is given by

$$\eta(k+1) = \begin{cases} \xi(k), & \text{if } |\xi(k)| > \delta \\ W\eta(k), & \text{otherwise} \end{cases} \tag{3.8}$$

where $W \in \mathcal{M}_{3\times3}(\mathbb{R})$ is the coupling matrix and δ is the tolerance constant ($\delta = 10^{-6}$). The TMNN operates in two phases: learning and prediction. Under learning, the TMNN receives at the input object trajectory $\xi(k) = (x(k), v(k), a(k))^T$, where $x(k)$, $v(k)$, and $a(k)$ are

[1] Examples, simulations, and videos are available at `http://www.cogneubotics.com/research.html`

the position, velocity, and acceleration of the object, respectively. Then the interneuronal couplings are updated according to:

$$W(k+1) = W(k)(I - \epsilon\xi(k-1)\xi^T(k-1)) + \epsilon\xi(k)\xi^T(k-1) \tag{3.9}$$

where $\epsilon > 0$ is the learning rate. Previously it has been shown that the learning process (3.9) converges, given that ϵ is small enough [7].

Once the learning is deemed finished, the TMNN can predict trajectories. The object initial moments $\xi(0) = (x(0), v(0), a(0))$ are sent to the TMNN for $k = 0$ and then $\xi(k) = 0$ for $k > 0$. On the output we get the predicted trajectory: $\eta(k) = W^k\xi(0)$.

3.3.2. Causal Neural Network

The CNN is a 2D lattice of FitzHugh-Nagumo neurons (80×80 cells in numerical experiments). The lattice dynamics is given by:

$$\begin{aligned} \dot{r}_{ij} &= q_{ij}\left(f(r_{ij}) - z_{ij} + d\Delta r_{ij}\right), \qquad (i,j) \in D \\ \dot{z}_{ij} &= \varepsilon(r_{ij} - 7z_{ij} - 2) \end{aligned} \tag{3.10}$$

where r_{ij} and z_{ij} are the membrane potential and recovering variable of the (i,j)-th neuron, respectively. Dots represent derivatives with respect to the mental time $\tau = hk$, Δ is the discrete Laplacian, and $f(r)$ is a cubic like nonlinear function. The system (3.10) is considered with Neumann boundary conditions. In numerical experiments we used $d = 0{,}2$, $\varepsilon = 0{,}04$, and $f(r) = (-r^3 + 4r^2 - 2r - 2)/7$. The function $q_{ij}(\tau)$ describes effective objects and will be discussed in Section 5.4.3.

At the beginning all cells are at rest ($r_{ij}(0) = z_{ij}(0) = 0$) except one. The neuron (i_a, j_a) corresponding to the agent's location has no dynamics $q_{i_a j_a} = 0$ and hence $r_{i_a j_a}(\tau) = r_{i_a j_a}(0) = 5$ for $\tau > 0$ (we remind that in the network space D the agent is reduced to a single cell).

3.3.3. Effective objects

The TMNN predicts movements of the obstacles and targets in the environment, while the CNN matches this information with the process of simulation of agent's movements.

A wavefront propagating from the agent position can be generated in the CNN (see Figure 3.3B). It switches cells to upstate. The time $\tau = c$ when the cell (i,j) crosses a threshold ($r_{ij}(c) = r_{\text{th}}$) is stored. Thus behind the wavefront we obtained a potential field $\{c_{ij}\}$ (see also Eq. (3.2)).

Let $\mathcal{B}(k)$ be a set of cells $\{(i,j)\} \in D$ occupied by obstacles and targets at the mental time k. Then we define the following iterative process:

$$\Omega(k) = \Omega(k-1) \cup \delta\Omega(k), \quad k = 1, 2, \ldots; \quad \Omega(0) = \emptyset \tag{3.11}$$

where

$$\delta\Omega(k) = \{(i,j) \in D : \quad r_{ij}(kh) \in [1,2], \quad (i,j) \in \mathcal{B}(k)\}$$

The set $\Omega(k)$ describes effective objects (obstacles and targets) in the network space D. It is dynamically created as the wavefront explores D. The set grows (i.e. $\delta\Omega(k) \neq \emptyset$) if the wavefront touches an object at $\tau = kh$. Then we define the function $q(\tau)$ in Eq. (3.10) as:

$$q_{ij}(\tau) = \begin{cases} 0, & \text{if } (i,j) \in \Omega(k) \\ 1, & \text{otherwise} \end{cases}$$

The cells in $\Omega(k)$ will exhibit no dynamics, i.e. the effective objects are *static* and the wavefront slips around them (Fig. 3.3B, panels $\tau_{2,3}$).

Once the exploration of D has been finished, the created CIR of the dynamic situation represents a Generalized Cognitive Map (Fig. 3.3C). It contains spatial relationships (a potential field c) structured by static effective objects. These effective objects contain critical information about possible collisions of the agent and obstacles (to be avoided) or targets (to be pursued).

3.3.4. Trajectory tracing

To obtain a trajectory we use the gradient descent method. Since the obtained map does not distinguish between obstacles and targets, we should designate one (or several) of the effective objects in the map to be a target. Then we start from some point at the effective target and go down the gradient $\gamma_{k+1} = \gamma_k - \nabla c$. The obtained trajectory ends at the agent's location (the deepest part of the potential). We note that by construction the potential $c(i,j)$ has no local minima and hence a solution always exists (Fig. 3.3C, arrowed curves).

3.4. Conclusions

Artificial cognition largely deals with the comprehension of relationships among elements in the environment. Nowadays the theoretical concept of cognitive maps, as a mean for understanding static situations, received strong experimental support [83]. However, in dynamic situations spatial relationships among objects evolve in time. Therefore, the corresponding cognitive map should also change in time, which contradicts the very concept of a map.

In this chapter first we discussed how the theory of compact internal representation [7] can generalize the concept of cognitive maps upon dynamic situations. The used neural architecture consists of two coupled neural networks. A recurrent neural network predicts positions of

the objects for $t > 0$. These data are mapped into the other 2D neuronal lattice that simulates what will happen if the agent takes this or that trajectory. A wavefront propagating over the lattice collides with objects provided by the first network and forms a static potential field surrounding "islands" representing the coincidences between agent and objects (Fig. 3.3). Thus, a dynamic situation can be "mentally" represented as a static structure similar to a classical map. We called this process Prediction-for-CompAction (PfCA). The obtained Generalized Cognitive Map or GCM enables navigation avoiding collisions both with moving and static obstacles. Besides, GCMs are more universal and independent of the context, in the sense that the neural network implementation makes no *a priori* distinction between obstacles and targets, and hence the same object can be assigned as a target or as an obstacle and the agent can plan a chasing or escaping actions.

4 Real-time generation of Generalized Cognitive Maps

In the previous chapter a wave-dynamics method has been proposed for building cognitive maps [7, 32, 91]. A wave front starting from the agent position virtually explores the environment and generates a so-called GCM [81]. Such an *egocentric* map contains information on possible collisions with obstacles in the Euclidean metric and can be used for planning multiple trajectories to multiple targets. Its drawback is the relatively high computational load, which stems from the modeling of a rather large 2D neural network. In short, the real-time performance of the model, essential when dealing with real robots, becomes unviable.

In this chapter we propose a model of an isotropic active medium based on traditional totalistic cellular automata (CA). CA are an efficient tool for simulating numerous wave phenomena in discrete media. However, their inherent anisotropy frequently contradicts the properties of modeled natural media and processes. Here we propose a computationally efficient isotropic CA with the standard Moore neighborhood. The model exploits a single postulate: the information transfer in an isotropic medium occurs at constant rate. To fulfill this requirement we introduce in each cell a local counter keeping track of the distance run by the wave from its source. This allows maintaining the wave velocity constant in all possible directions even in the presence of nonconductive local areas (obstacles) with complex spatial geometry. Then we illustrate the model on the problem of real-time building of cognitive maps used for navigation of a mobile robot. The isotropic property of the CA helps obtaining "smooth" trajectories and hence natural robot movement. The accuracy and flexibility of the approach are proved experimentally by driving the robot to a target avoiding collisions with obstacles.

4.1. Introduction

Simulation of different wave phenomena using cellular automata (CA) had its origins in the 1950s, when von Neumann, following the proposal made by S. Ulam, applied a fully discrete approach to describe the dynamics of spatially distributed systems. Later, due to the approach

simplicity and computational efficiency, CA have become widespread in different fields such as hydrodynamics [92], physical chemistry [93], microelectronics [94], material science [95], and biophysics [96], among others. In the last decades CA have also been proposed as an efficient tool for finding a path among two or more locations in a map or among vertices in a graph, a problem tightly related to studies of the algorithms for robot navigation in complex environments (for short review see, e.g., [97]).

Although important advances have been achieved, one of the main disadvantages of the standard CA resides in their intrinsic anisotropy. For example, a roving robot in a free space can move equally in any direction, while a CA may "prefer" some of them depending on the lattice geometry. Figure 4.1 shows canonical examples of the excitations generated by a point source (single-cell). In all cases the wavefront significantly deviates from a circular shape typically expected in natural systems and thus reveals the anisotropic structure of the CA. Note that the anisotropy comes both from the discrete nature of the lattice and from the local rules defining the cell states at each time step.

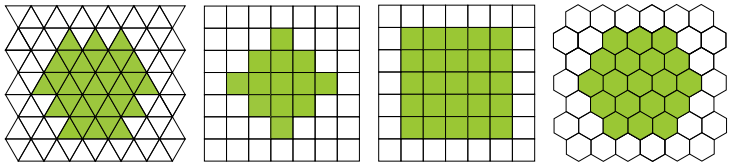

Figure 4.1: Canonical forms of wavefronts (left to right): in triangular, square with the von Neumann neighborhood, square with the Moore neighborhood, and hexagonal lattices. All waves deviate significantly from circular shape.

Attempts to overcome the CA anisotropy were made in numerous studies (see, e.g., [93, 98, 99, 100, 101]). In particular, Karafyllidis and Thanailakis [100] proposed a computationally efficient CA model for fast simulation of a forest fire, which involved global normalization (i.e., nonlocal knowledge). The model indeed reproduces a circular front, but its linear velocity decreases with time and it may not go through gaps among nonconductive local areas (obstacles). Later, Delorme and colleagues [101] showed that the circular wavefront in CA with binary states can be obtained with high-level algorithms only. Most of the recent works in this direction departure from the use of totalistic CA to automata with continuous state variables. Such models exploit the diffusion process (see, e.g., [93]) and/or the use of time delay [94] or virtually continuous time [102]. Then, the problem becomes similar to modeling reaction-diffusion processes by lattices of ordinary differential equations, known to produce circular fronts. Other methods employ extended Moore neighborhoods thus pushing the borders of local interactions in CA or make use of random variables, such as, e.g., random selection of neighboring cells [98, 103, 104]. Recently, Ortigoza [105] proposed an interesting approach, consisting in the use of a non-uniform triangular lattice. The method splits the space into finite elements and admits complex boundary conditions in problems focused on geographic applications. It has been shown that the model partially neutralizes the CA anisotropy. Nevertheless, designing an accurate and fast simulation by CA of the process of propagation of waves in isotropic media containing obstacles remains an open problem.

The applications of CA to the pathfinding problem range from the use of binary CA driven by simplistic rules [106, 107, 108] to modeling the foraging mechanism of slime mold [109]. Simple CA are attractive for the use in real-time tasks, but they usually exhibit significant pitfalls. For example, a non-Euclidian CA metric implies that the trajectory length cannot be directly assessed [106, 108]. This can cause a situation when a CA finds a suboptimal path. Besides, the commonly considered assumption that the agent has eight possible directions of motion on a square grid leads to unnatural low efficient robot movements [110, 111]. Furthermore, most of the recent works search for the shortest path by starting the excitation in CA from the target position (see, e.g., [106, 110, 111]). This has two drawbacks: i) the target must be *a priori* designated, which sometimes is unfeasible [112] and ii) single solution significantly reduces the agent flexibility. Meanwhile, an advanced cognitive robot capable of interacting with humans will demand diverse criteria to judge the optimality of solutions beyond the trajectory length [81, 113].

Our approach naturally avoids most of the above mentioned limitations. To gain speed we departure from the common approach of discretization of the reaction-diffusion equation. Instead, at the heart of the model there is an analogy with the well-known Huygens' principle, whereby every point of the medium reached by the wave becomes a source of a secondary circular wave. Thus, we use local information representing the distance of each cell to the closest source of excitation. However, as we will show below in the case of a CA, secondary sources may also appear at certain cells of contact of the wave with obstacles. The simplicity and efficiency of the basic equations allow applying this algorithm to real-time tasks. We then illustrate the model on a problem of controlling the navigation of a mobile robot through building cognitive maps. In contrast to other CA methods, our approach provides a variety of smooth (physically plausible) trajectories to the target, and the agent can choose among them according to the particular situation by optimizing the length, safety, or cooperation.

4.2. Model of isotropic totalistic CA

Let us now introduce a CA model and then provide evidence on its isotropic property, i.e., a constant velocity of the wave propagation in all directions.

4.2.1. Definitions

We simulate a CA on a two-dimensional square $(L \times L)$-lattice:

$$\Lambda = \{(i,j) \in \mathbb{N}^2 : \ 1 \leq i,j \leq L\}. \tag{4.1}$$

The state of each cell (i,j) at discrete time instants $t = 1, 2, \ldots$ is described by two discrete variables: $a_t(i,j) \in \{0, 1, \ldots, L^2\}$ and $z_t(i,j) \in \{0, 1, \ldots, L^2\}^2$ (the upper limit, L^2, corresponds to the number of cells in the lattice). $a_t(i,j)$ accounts for the cell activation (cell

(i, j) is activated if $a(i, j) > 0$ and not-activated otherwise) and keeps an information on the wave source that provoked the activity (see below), while $z_t(i, j)$ is an auxiliary counter that stores information on the propagation path to cell (i, j). The first component of $z_t(i, j)$ is the total number of steps performed to arrive to cell (i, j), whereas the second one is the number of diagonal steps among them (Fig. 4.2).

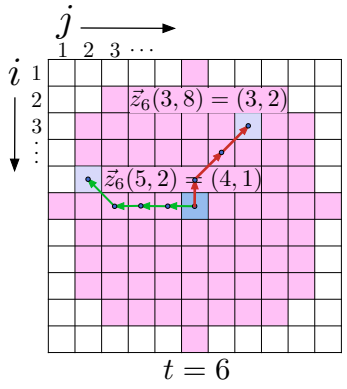

Figure 4.2: Example of calculation of the auxiliary variable z_t for $t = 6$ (the wave source is in the center of the lattice). Although several shortest paths may lead to the same target cell, they provide unique counter value.

At $t = 1$ the CA is initialized by activating one or several cells (initial sources):

$$a_1(i, j) = \begin{cases} 1 & (i, j) \text{ is initial source} \\ 0 & \text{otherwise,} \end{cases} \qquad (4.2)$$

$$z_1(i, j) = (0, 0), \quad \forall (i, j) \in \Lambda.$$

It allows modeling situations with multiple or/and spatially extended initial sources. Then we denote the set of the activated cells in the CA at time t by:

$$A_t = \{(i, j) \in \Lambda : \ a_t(i, j) > 0\}. \qquad (4.3)$$

A_1 thus corresponds to the set of initial sources. As we will see below, an activated cell cannot be deactivated and the number of the activated cells can only grow, thus $A_t \subseteq A_{t+1}$.

For further calculations we introduce the following sets:

- $B \subset \Lambda$ representing cells occupied by obstacles,
- $\Gamma \subset \Lambda$ corresponding to secondary wave sources (see below),
- $E_t = (\Lambda \backslash (A_t \cup B)) \cup \Gamma$ denoting the set of cells that can be activated ("empty" space).

The Moore neighborhood of a cell (i, j) can be defined as

$$M_{ij} = \{(k, l) \in \Lambda : \|(k - i, l - j)\|_\infty = 1\}. \qquad (4.4)$$

Note that in our case $(i,j) \notin M_{ij}$. Then for each cell (i,j) we define a map[1] $r_t : M_{ij} \to \mathbb{N}^2$

$$r_t(k,l) = \begin{cases} (0,0) & (i,j) \notin E_t \vee (k,l) \notin A_t \\ z_t(k,l) + (1, \mathbb{1}_{D_{ij}}(k,l)) & \text{otherwise,} \end{cases} \tag{4.5}$$

where $\mathbb{1}_{D_{ij}} : M_{ij} \to \{0,1\}$ is the characteristic (indicator) function of the diagonal neighborhood:

$$D_{ij} = \{(k,l) \in \Lambda : |k-i||l-j| = 1\} \subset M_{ij}. \tag{4.6}$$

Note that $\|r_t(k,l)\|_2$ have the meaning of the distance to the corresponding wave source for all activated cells in the Moore neighborhood of (i,j), thus providing possible values for $z_{t+1}(i,j)$. Then, among these values, we will choose an optimal one (see below).

4.2.2. Computational scheme

Without loss of generality, we can assume that the velocity of a wavefront is equal to one. Then t characterizes also the distance that the wave has overcome at a given time step and the rules for updating the CA state are as follows:

Step I: For each cell $(i,j) \in \Lambda \backslash B$:

1. Determine the set of cells from its Moore neighborhood that could *potentially* be sources of activation for the given cell (i,j):
$$W_t = \{(k,l) \in M_{ij} : t < a_t(k,l) + \|r_t(k,l)\|_2 \leq t+1\}.$$
2. Using W_t determine the cell transmitting excitation to (i,j):
$$(i_t^*, j_t^*) = \begin{cases} \operatorname{argmin}\{\|r_t(k,l)\|_2 : (k,l) \in W_t\} & W_t \neq \emptyset \\ (i,j) & \text{otherwise.} \end{cases}$$
3. Update the cell state:
$$a_{t+1}(i,j) = \begin{cases} t+1 & (i,j) \in \Gamma \wedge (M_{ij} \cap A_t) \neq \emptyset \\ a_t(i_t^*, j_t^*) & \text{otherwise.} \end{cases}$$
$$z_{t+1}(i,j) = \begin{cases} z_t(i,j) & (i,j) \notin E_t \backslash \Gamma \vee W_t = \emptyset \\ r_t(i_t^*, j_t^*) & \text{otherwise.} \end{cases}$$

Step II: Using definition (5.8) obtain the set of activated cells A_{t+1} from $\{a_{t+1}\}$.

Repeat Steps I and II in a loop until $t = T_{\max}$, where $T_{\max}$ is the first time instant when $A_{t+1} = A_t$ is satisfied.

[1] To avoid the notation overloading we omit the index (i,j) in definition (4.5).

4.2.3. Wave propagation in empty space

Let us now test the algorithm in an empty space (i.e., $B = \emptyset$). Due to the discreteness of the space, time, and state variables the wavefront in a totalistic CA may differ significantly from the circular one (Fig. 4.1). We then introduce the following measure of the wave "circularity"

$$C(t) = 1 - \frac{\Delta S(t)}{\pi(t-1)^2}, \tag{4.7}$$

where $\Delta S(t)$ represents the measure of the symmetric difference between the set of activated cells and a circle of the corresponding radius (Fig. 4.3, red area in inset; for convenience the cell spatial dimension is (1×1) a.u.). Thus, $C = 100\,\%$ corresponds to a perfect circle, while low values of C indicate strong deviation of the wavefront from a circular shape.

We then simulated the process of propagation of a wave generated by a point source (single cell). Figure 4.3 shows the measure (4.7) and examples of the wave shape obtained by the algorithm for $t = 2, 3, 5$, and 15. It can be observed that for each $t \geq 2$ the centers of all activated cells belong to the closed disk of radius $t - 1$. Thus, our algorithm maximizes the measure (4.7) for waves propagating with constant velocity and hence the proposed CA indeed models an isotropic medium.

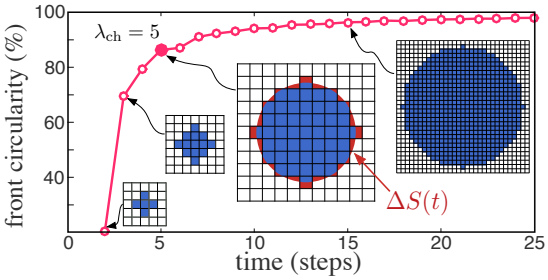

Figure 4.3: Evolution of the measure of the front circularity during propagation of a wave initiated by a point source. At $t = 5$ (thick red dot) the wavefront is considered round enough. This time instant defines the characteristic length scale λ_{ch} (see main text for details).

Insets given in Figure 4.3 also show that at the beginning the wavefront is far from a circle and consequently the circularity measure takes low values. At $t = 5$, C reaches the value of $87\,\%$, i.e., the wave can be considered circular enough, and then we observe some "saturation" ($C(6) = 88\,\%$). The same critical scale ($t = 5$) also appears when dealing with the secondary wave sources at obstacle boundaries (see below). This observation has an important implication. Let us recall an analogy with the geometric and wave optics. Since for $t < 5$ the wave is qualitatively different from a circle, its interaction with obstacles on such space scales (less than 5 cells) can differ significantly from the process of wave propagation in open space. Thus, we can introduce a characteristic spatial scale for totalistic CA: $\lambda_{\mathrm{ch}} = 5$ cells. In what follows, we will assume that the distance between adjacent obstacles is higher than λ_{ch}, i.e., we omit from consideration the effects of "interference" related to wave optics.

This model "granularity" should be taken into account in applications such as, e.g., robot navigation.

4.3. Secondary wave sources

The algorithm described in Section 4.2.2 includes a set of "extra" secondary wave sources Γ. They appear at certain cells of contact of the wave with obstacles, analogously to the well known Huygens' principle.

4.3.1. Isotropic CA in free space and front breaking at obstacles

Before defining this set, let us consider a wave propagating in the CA without secondary fonts, i.e., we assume $\Gamma = \emptyset$.

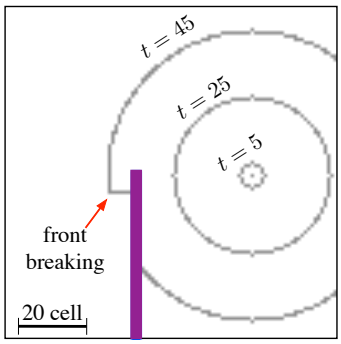

Figure 4.4: Example of a circular wave propagating in empty space ($t = 5$ and $t = 25$; for visual clarity only the wavefront was drawn) and the front distortion ($t = 45$) at contact with obstacle (magenta vertical strip) in the absence of secondary sources, i.e., assuming $\Gamma = \emptyset$.

Figure 4.4 illustrates the process of propagation of a wave in a CA with a single obstacle (magenta vertical bar). In empty space, i.e., before the contact with the obstacle, the wavefront is circular (measure (4.7) approaches $100\,\%$). Thus, once again the model indeed implements an isotropic medium. Nevertheless, interaction of the wavefront with obstacles may lead to unsatisfactory results. Depending on the obstacle curvature and characteristics of the wavefront at the moment of contact, the front shape may be distorted, causing the front "breaking" (Fig. 4.4, arrow).

The reason for breaking the front geometry while a wave bends an obstacle lies in the violation of the principle of causality. The updating of the cell states (Step I.3 of the algorithm) involves an implicit calculation of the distance to the original wave source, r_t. Eventually, this distance becomes distorted for certain cells that are "behind" the obstacle. In turn, this leads to a premature activation of these cells and disruption of the wavefront geometry.

4.3.2. Interaction of wave with obstacles: secondary wave sources

To get rid of the effect described in Section 4.3.1, we propose the concept of "additional secondary" wave sources, which is inspired by the Huygens' principle. Such sources appear at contact of the wavefront with certain cells on the obstacle boundary. As we show below the secondary sources prevent front breaking and thus we obtain correct wave propagation even in the presence of obstacles.

In what follows we will assume that each obstacle is a connected set of cells with a minimal "thickness" equal to two cells. To determine the cells corresponding to secondary sources (i.e., the set Γ) we provide the following algorithm:

1. Determine *potential* secondary sources. Cell (i, j) is a potential secondary source if
$$\mathrm{card}(B \cap M_{ij}) \leq 4, \quad (i, j) \in B.$$
2. Enumerate all potential secondary sources following counterclockwise along the obstacle boundary $\{(i, j)_q\}$, $q = 1, 2, \ldots, Q$. Then, define vectors:
$$(k_q, l_q) = (i, j)_{q+1} - (i, j)_q.$$
3. Define secondary sources. A cell $(i, j)_q$ is a secondary source if
$$\lambda_{\mathrm{ch}}(k_{q-1}l_q - k_q l_{q-1}) > \max\{0, k_{q-1}k_q + l_{q-1}l_q\}.$$

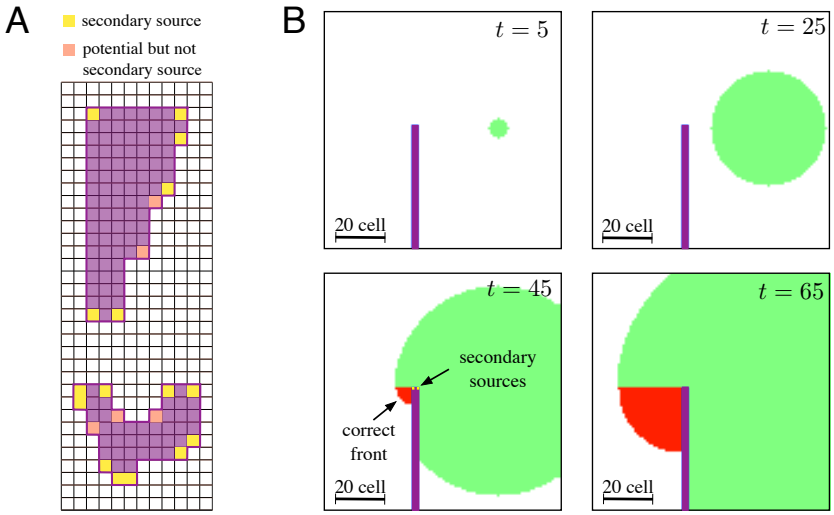

Figure 4.5: Secondary wave sources. **A)** Illustration of the algorithm determining secondary wave sources. Cells on the corners of the obstacle boundary are potential secondary sources (yellow and orange). Only yellow cells satisfy the condition (3) and consequently are assigned as secondary sources. **B)** Propagation of a circular wave and its correct interaction with obstacle (see Figure 4.4 for comparison) due to the presence of the secondary wave sources (arrow).

Condition (1) selects "vertices" of the obstacles, whereas condition (3) discards among them those cells that involve small enough change in the direction between vectors (k_{q-1}, l_{q-1}) and (k_q, l_q). The critical value is defined by the granularity constant λ_{ch} (see Section 4.2.3). Note, that this algorithm is applied only once. Then the set Γ is used in the computational scheme described in Section 4.2.2.

Figure 4.5A illustrates the process of identification of the secondary wave sources for two obstacles. On the first step the cells candidates to be secondary sources are determined (condition (1), yellow and orange cells). Then a part of them is assigned as secondary sources in agreement with condition (3) (yellow cells).

To illustrate the effect produced by the secondary wave sources on the wave propagation, we repeated the numerical experiment shown in Figure 4.4. Figure 4.5B shows the process of wave propagation in the presence of secondary wave sources. At the beginning ($t = 5$, $t = 25$) there is no difference with the previous calculation (see Figure 4.4). However, when the wave reaches the tip of the obstacle, one of the secondary sources is activated and generates a "secondary" wave (drawn in red in Figure 4.5B, $t = 45$). As a result, the wavefront keeps physically plausible geometry and we obtain a circular wave "behind" the obstacle, as expected.

4.4. Modeling wave interaction with complex obstacles

Let us now illustrate the process of wave propagation in a CA with multiple obstacles of different spatial geometries.

Figure 4.6 shows numerical simulation of a CA consisting of (400×400) cells. A wave, generated by a single initial source (Fig. 4.6, $t = 110$, arrow), propagates among four obstacles (drawn in blue). When touching obstacles new secondary sources are activated and the state variable, $a_t(i, j)$, of these cells receives the value corresponding to the time

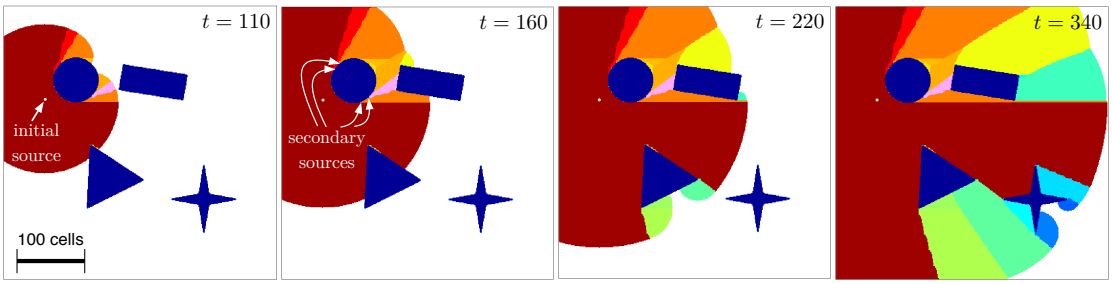

Figure 4.6: Wave propagation in an isotropic (400×400) totalistic CA with obstacles of complex geometry (painted in dark blue). The color from red to blue corresponds to parts of the wave generated by different secondary wave sources. Circle obstacle generates the highest number of secondary waves (most colorful part of the wave).

instant of activation. Each of the activated secondary sources (Fig. 4.6, $t = 160$, arrows) generates a new wave. Consequently all cells receiving activation from a certain secondary source inherit this new value of the state variable a. This mechanism of changing $a(i, j)$ enables simple visual tracing of the propagation of excitation in the lattice. We painted the wave in different colors in line with the wave sources generating the corresponding part of the wave. In particular, dark red color corresponds to cells whose activation can be traced back to the initial source, whereas colors from red to blue mark parts of the wave generated by secondary sources (Fig. 4.6, $t = 220$ and $t = 340$).

Analyzing Figure 4.6 we observe that the most complicated thing in terms of the number of secondary sources is the process of bending by the wave of the circle obstacle. This process involves seven secondary sources, while rounding rectangle requires three sources. Such a difference stems from the discrete nature of CA. Indeed, secondary sources appear on convex "corners" in the obstacle boundary (see Figure 4.5A). Although in a continuous medium a circle has no corners, its discrete representation in the lattice creates multiple corners (Fig. 4.3, insets). The other three obstacles (rectangle, triangle, and star) have simpler structures from the viewpoint of secondary sources. Therefore, the wave rounds such obstacles without exciting many secondary sources and we observe fewer color changes.

4.5. Application of CA to robot navigation

Let us now provide an example of a sensible application of the proposed CA model. As it has been mentioned in the introduction, the wave dynamics can be used for building cognitive maps, which in turn can be used for robot navigation (for details, see, e.g., [7, 81]).

Figure 4.7A illustrates an experimental setup consisting of a (255×345) cm arena simulating a corridor with obstacles (painted in orange). A wheeled robot, Pioneer 3DX (Adept Mobilerobotics, linear sizes (l×w×h): 45.5×38.1×23.7 cm), should cross the corridor avoiding obstacles and reach "exit" (blue strip). No direct route to the target is available.

To solve this task the robot was equipped with an onboard computer (NUC, Intel) with customary software packages written in Matlab (Mathworks). The computer was interfaced through WiFi connection to a zenithal camera and through a USB-COM adapter to the robot controllers driving the wheels.

The captured visual information (Fig. 4.7A) is preprocessed: the target, obstacles, and robot are detected and projected to the floor. Then the obtained abstract image of the situation is mapped into an (80×107) CA network (Fig. 4.7B). This network size (1 cell $\approx 3 \times 3$ cm) is a compromise between the computational load and navigation accuracy. Indeed, from the one hand side 3 cm is below $10\,\%$ of the robot size, which is a reasonable tolerance for motion of animated agents. From the other side, taking into account the linear robot velocity of 30-40 cm/s, we obtain that the robot advances 1 cell in less than 100 ms, which

is about the time necessary to process visual information. The robot also projects itself into the CA network. However, in the lattice space the robot occupies a single cell only (thick black dot in Figure 4.7B). Then, to maintain the balance, its real dimension is properly added to the obstacles (magenta *vs.* orange color), thus proportionally increasing their sizes. Such a procedure facilitates searching for possible robot movements since it allows tracing trajectories regardless the actual robot size and its positioning among obstacles [89].

Once visual information has been properly mapped into the CA, the robot simulates the exploration of the environment by a wave process (Fig. 4.7C). Note that this exploration is done in internal or "mental" time τ and due to the computational efficiency of the CA model it is fast enough. The wave starts from the robot position (single cell) and finds all possible gaps between obstacles, and finally reaches the target. A quite complex intermediate wave profile at $\tau = 70$ evidences nontrivial possibilities of solving the navigation problem.

Finally, the wave dynamics builds a cognitive map of the given situation (for details, see [7, 54]). The map is obtained by a local sum over time (Fig. 4.7D):

$$P_{ij} = \sum_{t=1}^{T_{\max}} \mathbb{1}_{A_t}(i,j). \tag{4.8}$$

Then, by the gradient descend method adapted to the discrete nature of CA we can trace several trajectories to the exit (target). Figure 4.7D shows four qualitatively different ways to reach the exit. The trajectory smoothness enables natural movement of the robot, not restricted to piecewise linear paths in eight direction commonly adopted in other works (see e.g., [106, 111]). The selection among different trajectories requires a motivation criterium

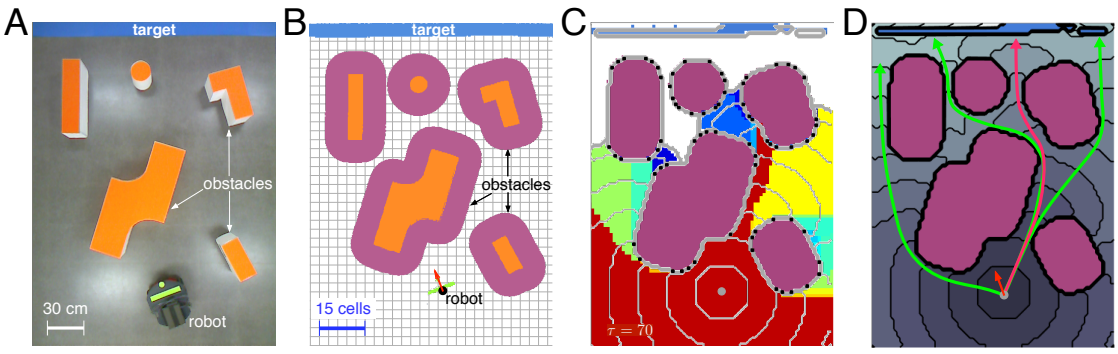

Figure 4.7: Application of CA to cognitive navigation. **A)** Experimental setup (top view). A wheeled robot (Pioneer 3DX) moves along a corridor to an exit (blue stripe) avoiding obstacles (orange). **B)** Abstract visual perception of the situation shown in (a) and its mapping on the CA lattice. The robot is represented as a black dot (occupies one cell in CA), whereas all obstacles are increased by the robot dimensions. Red arrow indicates the robot head direction. **C)** A snapshot (at $\tau = 70$, τ is the simulation or "mental" time of the robot) of the process of building a cognitive map in the CA model. Black dots in obstacle boundaries represent secondary wave sources. Colors show the wave origin (as in Figure 4.6). **D)** Cognitive map of the situation built by the CA and feasible trajectories (red one is the shortest). Contour lines show the configuration of the wavefront at different time instants.

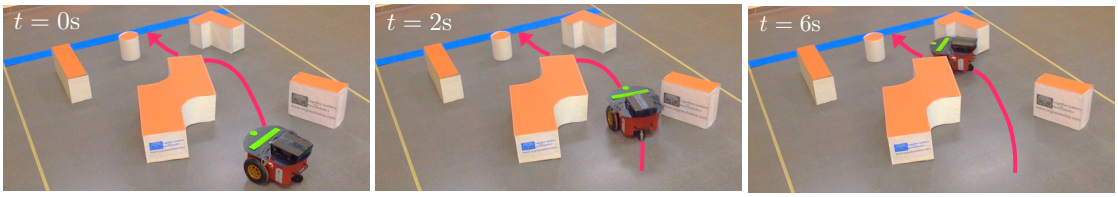

Figure 4.8: Three consecutive snapshots of the robot movement. The robot follows one of the trajectories found by the CA (red in Figure 4.7D). Thin yellow stripes delimit the "corridor" and blue stripe marks the "exit" (target). The video is available at: `http://www.cogneubotics.com/research.html`

and in general can be achieved by using a motivation neural network [114]. Here we choose the shortest way to the exit (Fig. 4.7D, red curve).

Once a trajectory has been obtained, the robot can perform specific motor commands and, if the cognitive map has been built correctly, it will reach the target avoiding collisions with obstacles. Since our agent is a differential wheeled robot, it requires angular velocities as input [115]. Thus, instead of advancing to the next cell in the path in one of the eight discretized directions, the robot uses a smooth trajectory built up from appropriate arcs. As a result the robot moves along a physically plausible path without sharp changes of the direction requiring "stop-and-go" movements. We note that the Pioneer 3DX embedded controller estimates the position of the robot in space (through odometry), which we used in a feedback loop to ensure precise positioning of the robot. This approach allows reaching an accurate execution of trajectories. To crosscheck the motor accuracy we estimated the deviation of the robot from a target point after following a trajectory of 6 m long. The error obtained on a circle trajectory was $2{,}9 \pm 1{,}4$ cm, while following an "8" shape trajectory it slightly increased up to $5{,}7 \pm 2{,}5$ cm, which is satisfactory for real-life applications.

Figure 4.8 shows three consecutive snapshots of the robot moving in the arena following the red trajectory shown in Figure 4.7D. It successfully avoids obstacles and reaches the exit, as expected.

In experimental conditions the process of building a cognitive map takes around 300 ms, which is close to the human reaction time [116]. Taking into account the linear robot velocity 30-40 cm/s (robot displacement < 15 cm), a cognitive map can be obtained in real-time. We then repeated experiments in several different environments including time evolving. Figure 4.9 shows an example of such a situation. At the beginning the robot constructs a cognitive map corresponding to the initial situation and starts moving to the target (Fig. 4.9A). However, on the go the situation changes drastically: the z-shape obstacle is rotated unexpectedly (Fig. 4.9B) and blocks the path to the target. As soon as the robot realizes (< 100 ms) that the situation has been changed and no way to the target is available, it slows down and builds a new cognitive map. New map provides new trajectory to the target and hence the robot makes a turn and successfully reaches the target (Fig. 4.9C).

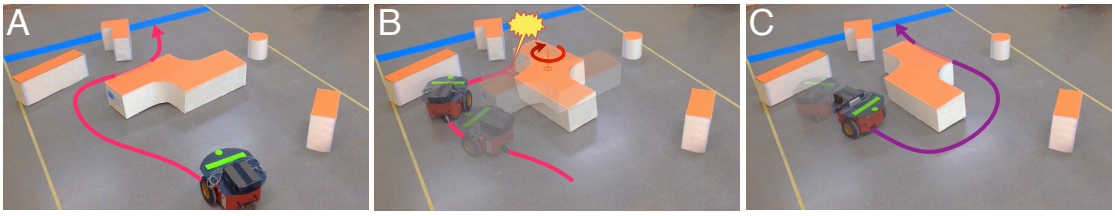

Figure 4.9: Robot navigation in drastically and unexpectedly changing environment. **A)** Initial situation. The robot builds a cognitive map and starts moving to the target (similar as in Figures 4.7 and 4.8). **B)** On the go the situation changes unexpectedly. The z-shape obstacle in the center of the corridor is rotated and blocks the robot path. The robot slows down and recalculates the cognitive map. **C)** New trajectory to the target is executed. The video is available at: `http://www.cogneubotics.com/research.html`

4.6. Conclusions

In this chapter we have proposed a model of a totalistic isotropic CA. It enables the simulation of the process of wave propagation in media with obstacles (areas not penetrable for waves). We note that our model differs significantly from other approaches. Earlier, similar results have been achieved with the use of CA described by continuous variables, simulating the diffusion equation (see e.g., [102, 117]). Instead of discretizing the Laplacian our model exploits a single postulate: "the information transfer in an isotropic medium occurs at constant rate". To achieve this property in a totalistic CA we introduced in each cell a local counter keeping track of the distance run by the wave from its source. This allowed maintaining the wave velocity equal in all directions. For correct interaction of waves with obstacles we introduced secondary wave sources in accordance with the Huygens' principle. Such sources appear at certain cells on the boundary of obstacles (at certain "vertices") and allow keeping physically plausible wavefront geometry. Numerical simulations have confirmed that indeed the proposed CA enables fast and correct modeling of the process of propagation of waves in isotropic media with complex spatial configurations.

Due to its minimalistic nature (simple local rules *vs.* extended Moore neighborhood used, e.g., in [98, 103]), our model is computationally efficient and it permits relatively simple hardware implementation on a chip, which may further increase the calculation speed [117, 118]. Thus, it can be useful for real-time tasks, such as, e.g., simulation of the heart muscle [119] or building cognitive maps to control mobile robots [54, 81]. To illustrate this ability we implemented the model on an onboard computer of a wheeled robot. The CA was used to build cognitive maps [91]. On the onboard computer this process lasted around 300 ms, independently on the complexity of the environment. This delay falls within the time scale of human reaction [116], which allows the robot to react promptly to unexpected changes in human environments [81, 113].

One of the important differences with other approaches (see, e.g., [106, 110, 111]) is the use of egocentric maps. The cognitive maps built by our model admit several alternative paths

(*vs.* the common approach searching for the shortest trajectory) and thus provide flexibility to accomplish the navigation task. Such an ability is an essential feature of cognitive agents. Then a robot can find optimal trajectories resembling human displacement, which is a must for pursuing the robots deployment in our daily life. In addition the egocentric algorithm does not require any *a priori* knowledge about the target. It just considers the perceived objects as entities, which can be reached or avoided according to the motivation and necessities of the agent. In this way the algorithm enables local and global robot navigation, increasing the versatility of the decision-making.

Real-time algorithms are for real world. To achieve natural, physically plausible robot movements we have payed much attention to the trajectory smoothness. This aspect, frequently overlooked by researchers (see, e.g., [107, 108, 110]), may significantly improve the robot performance in real-life scenarios. The pursued isotropic property of CA makes trajectories smooth up to the discreteness of the lattice. Then a complementary smoothing step eliminates the lattice granularity and facilitates the motor execution of trajectories. As a result the robot can advance naturally, avoiding sharp jumps, turns, and stop-and-go type of movement. Our experimental results have shown that: i) The robot equipped with the CA is able to build a cognitive map and when possible to find an optimal trajectory to a target (it may not exist). Then the robot successfully navigates to the target, smoothly avoiding obstacles. ii) If during the robot movement the situation is changed drastically, e.g., some obstacle changes position or another one appears unexpectedly and blocks the path, the robot is able to recalculate the map on the go. Then it selects another way to the target, and accomplishes the initial task[2].

[2]Videos are available at: `http://www.cogneubotics.com/research.html`

5 | Cognitive limbs for dynamic situations

Cognitive object handling and manipulation are vital skills for humans and future humanoid robots. However, the fundamental bases of how our brain solves such tasks remain largely unknown. In this chapter we provide a novel approach that describes the problem of limb movements in dynamic situations on an abstract cognitive level [63, 120]. The approach involves two main steps:

1. Transformation of the problem from the limb workspace to the so-called handspace, which represents the limb as a point and obstacles as objects of complex shapes.
2. Construction of a generalized cognitive map (GCM) in the handspace by a neural network simulating activation wave.

The GCM enables tracing a trajectory to a target that can be followed by the limb, which ensures collision-free movement and target catching in the workspace. We validate our approach by numerical simulations on an avatar developed for a humanoid robot Poppy and provide a robust scalable solution applicable to limbs with redundant number of degrees of freedom (DoF) [121].

5.1. Introduction

The effective and efficient object handling and manipulation are vital for humans' daily life. In this context the sensory-motor abilities ordinarily exhibited by humans in different environments may appear simple at first glance. However, many of them require forecasting the future states of different elements of the environment and their matching with feasible body movements.

The intrinsic complexity of this problem impedes modern robots to mimic smoothly even basic human motor skills in real-life scenarios. Existing works dealing with manipulators usually exploit one of the following paradigms:

1. The potential field method, originally putted forward by Khatib [122, 123, 124].
2. The technique based on learning from demonstration [55, 82, 125].
3. The dynamical system approach based on construction of attractors and repellers in a phase space [126].
4. The neural network approach [127, 128]. Despite important results recently obtained, still most of the works deal with either static or quasi-static situations and pay little attention to the cognitive abilities of the developed solutions. Moreover, frequently the provided approaches have a limited level of abstraction and hence lack scalability or portability.

Extensive literature suggests that a purely programmatic approach to the problem of limb movement can only work in tailor-made scenarios [129]. It is not robust to changes in the environment and requires complete rebuilding if, e.g., we try to transfer mathematical methods developed for a manipulator with minimal number of degrees of freedom (DoF) to a redundant one [130]. Thus, the problem of effective object manipulation requires support at an abstract cognitive level.

Growing experimental evidence suggests that mammals, and humans in particular, use an internal representation of the environment and the body for movement planing and execution [83, 131, 132, 133, 134, 135]. In previous sections we generalized the notion of cognitive maps into time-evolving situations and introduced the so-called *generalized cognitive maps* (GCMs) [7, 81], which provide an abstract description of the dynamic environment. Briefly, a GCM is built by a wave propagating in a neural network that models all possible subject's movements. The wave extracts the relevant spatiotemporal events from the environment and projects them into a purely spatial map. Thus, the time dimension disappears and we get a static representation that can further be used for path planing and execution, like an ordinary cognitive map [54, 77].

Nevertheless, the original procedure of building GCMs [7] described in Chapter 3 assumes that the subject has a rigid body, i.e., there are no internal degrees of freedom. Then the essential spatial extension and changing geometry of a limb bring additional degree of complexity. Thus, GCMs cannot be applied straightforwardly to modeling the arm movements. To resolve this problem, here we propose a transformation that allows extending the GCM-theory into limbs embedded in dynamic situations [63, 120]. In the resulting task or handspace [136] we can easily build GCMs and trace global collision-free trajectories for limb movements.

In this chapter we develop a general neural network approach implementing the concept of cognitive maps for a versatile controlling of limbs in time-evolving situations. The approach provides robust scalable solution and is applicable to limbs with minimalistic and redundant number of DoF. It also enables a constraint biasing efforts in target reaching among different DoF.

5.2. The Model for minimalistic limbs

Here we show how the concept of Generalized Cognitive Maps, developed for rigid agents, can be extended to a manipulator with two degrees of freedom. To enable the use of GCMs, we first have to eliminate the limb spatial dimensions and rotational degrees of freedom. This allows representing the limb as a point in some equivalent task space.

5.2.1. The 2DoF manipulator

Figure 5.1 illustrates a two-joint manipulator in a two-dimensional workspace, $\mathcal{W} \subset \mathbb{R}^2$. The limb shoulder is fixed at the origin of the plane (x_1, x_2) and joined to an articulated elbow by a rigid segment of length ρ. A forearm of length l joins the elbow with a hand located at $\vec{x}_h \in \mathbb{R}^2$. To generalize the further calculations, in what follows we rescale the spatial coordinates in such a way that the length of the forearm is $l = 1$ a.u. We then restrict the workspace to $\mathcal{W} = \overline{\mathcal{B}}_{\rho+1} \setminus \{\vec{0}\}$, i.e., a disk of radius $\rho + 1$ centered at the origin (here and farther on, $\overline{\mathcal{B}}_r$ denotes a closed disk of radius r centered at the origin).

The shoulder and elbow joints can freely rotate, thus changing the configuration of the limb and, consequently, the hand position. Our goal is to catch by the hand a target avoiding collisions with obstacles. In general the target and obstacles can move and have arbitrary shape. We thus aim at a holistic model of the arm that would allow solving this problem efficiently.

Without loss of generality let us first assume that there exists a single point-like target at $\vec{x}_t \in \mathcal{W}$ and an obstacle at $\vec{x} \in \mathcal{W}$ (Fig. 5.1, pink and blue circles, respectively). The forearm segment cannot cross the obstacle, thus the hand cannot directly reach the target (Fig. 5.1, dashed trajectory). Therefore, to accomplish the goal the limb first must shrink going down and then extend to the target (Fig. 5.1, solid trajectory). The situation becomes much more complex if during the motor execution the obstacle and/or target move in the plane (x_1, x_2) or in the global 3D space.

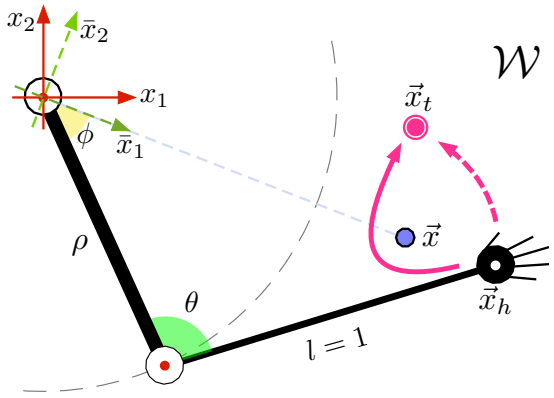

Figure 5.1: Two-joint manipulator (an upper limb) in a workspace $\mathcal{W}$. The shoulder is fixed at the origin. The upper arm and forearm have lengths ρ and $l = 1$ a.u., respectively. The upper arm forms an angle ϕ with the direction to a point-like obstacle located at $\vec{x}$ (blue circle). The limb segments can freely rotate around the shoulder and elbow (red dots in open circles). The hand at the end of the forearm, $\vec{x}_h$, should reach a target at $\vec{x}_t$ (pink circle). The direct motion along the dashed pink curve leads to a collision with the obstacle whereas the longer solid pink curve avoids collisions.

5.2.2. Transformation to the 2D Handspace

We now introduce the 2D *handspace* $\mathcal{H}_2 = \overline{\mathcal{B}}_{\rho+1} \setminus \mathcal{B}_{\max\{0,1-\rho\}}$, in which the same metric than in $\mathcal{W}$ is established. Each object including the limb is mapped from $\mathcal{W}$ into $\mathcal{H}_2$ in a specific way.

Compaction of the Limb

In the case of the limb, the mapping leads to a compaction

$$C: \begin{array}{ccc} \mathcal{P}(\mathcal{W}) & \to & \mathcal{H}_2 \\ L & \mapsto & \vec{x}_h \end{array}, \tag{5.1}$$

where $L \subset \mathcal{W}$ represents the union of the upper arm and forearm segments. Thus, the whole limb is reduced to a single point located at the hand position $\vec{x}_h \in \mathcal{H}_2$.

Extension of Objects

The mapping of objects goes in the opposite way. An object in the workspace is in general mapped into a set of curves, generating an extended object in the handspace. Geometrically,

this extended object represents the locus of hand locations while the limb slides around the object (Fig. 5.2).

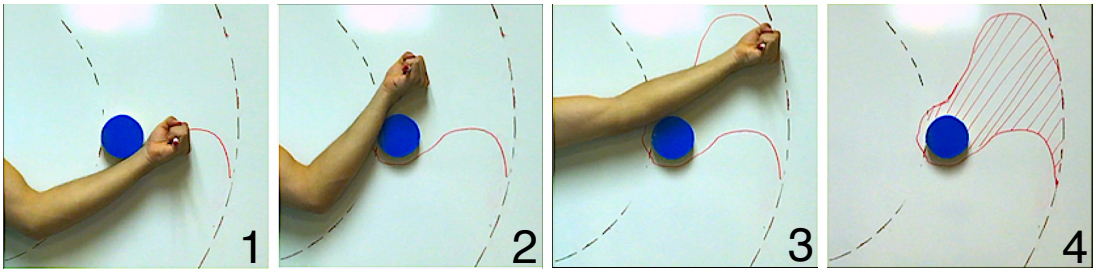

Figure 5.2: Generation of an extended obstacle by a human (three successive snapshots and the final extended obstacle are shown in panels 1–4). The hand moves continuously ensuring that the forearm always touches the static obstacle (blue cylinder) attached to a whiteboard. Along the movement the curve drawn by a marker depicts the boundary of the extended obstacle.

To express the handspace transformation of a point-like object $\vec{x} \in \mathcal{W}$, it will be useful to define the matrix of rotation between the original axes and those whose abscissa points to $\vec{x} = (x_1, x_2)^T$. In what follows:

$$\mathcal{M}(\vec{x}) = \frac{1}{\|\vec{x}\|} \begin{pmatrix} x_1 & -x_2 \\ x_2 & x_1 \end{pmatrix}. \tag{5.2}$$

Note that $\mathcal{M}$ is the matrix that transforms the basis from the local coordinates $(\bar{x}_1, \bar{x}_2)$ (Fig.5.1, green axes) to the global ones (x_1, x_2) (Fig.5.1, red axes). Thus $\vec{x} = \mathcal{M}\vec{\bar{x}}$, where $\vec{x}$ and $\vec{\bar{x}}$ are two different representations of the same point in $\mathcal{W}$, in the global and local coordinates, respectively.

Case 1. Let us first assume that a point-like object (Fig. 5.3A, blue dot) is reachable by the upper arm, i.e.,

$$\vec{x} \in \mathcal{A}_1 = \overline{\mathcal{B}}_\rho \setminus \{\vec{0}\} \subset \mathcal{W}. \tag{5.3}$$

Then a contact will take place whenever $\phi = 0$, where ϕ represents the angle that the upper arm forms with the direction given by $\vec{x}$ (see Figure 5.1). Thus, denoting by θ the angle between the upper arm and the forearm, we obtain the expansion

$$E_1(\vec{x}) = \{F_1(\theta, \vec{x}) : \theta \in [0, \pi]\} \subset \mathcal{H}_2 \tag{5.4}$$

(brown semicircumference in Figure 5.3A), where

$$F_1(\theta, \vec{x}) = \mathcal{M}(\vec{x}) \begin{pmatrix} \rho - \cos\theta \\ \sin\theta \end{pmatrix}. \tag{5.5}$$

The constraint $0 \leq \theta \leq \pi$ in (5.4) is imposed by the elbow nature.

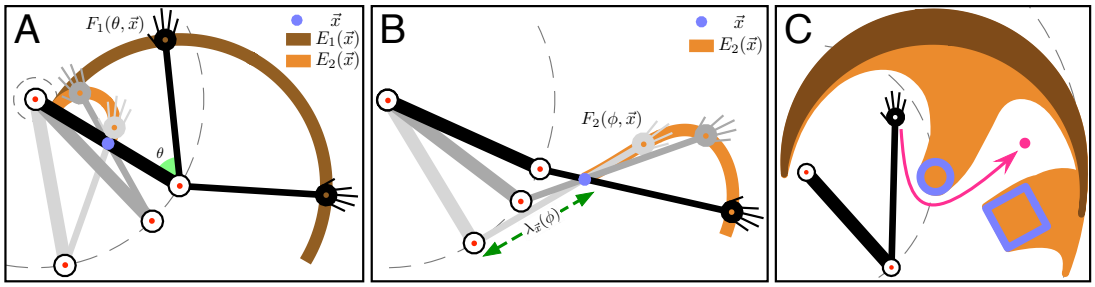

Figure 5.3: Mapping objects from the workspace $\mathcal{W}$ to the handspace $\mathcal{H}_2$. **A)** Situation where a point-like object is reachable by both the forearm and upper arm. The extended object has two parts: E_1 (brown curve) and E_2 (orange curve). E_1 is made up of the hand positions corresponding to a contact of the upper arm with the object and rotation of the forearm (two configurations are shown in black). E_2 is obtained from the set of the hand positions corresponding to sliding the forearm around the object (two configurations are shown in different gray intensity). **B)** A point-like object at $\vec{x}$ (blue dot) not reachable by the upper arm (same as in Figure 5.1) is mapped into an extended object, E_2 (orange curve). It is made up as the corresponding E_2 in panel A (three configurations are shown in different gray intensity). In this case, $E_1 = \emptyset$. **C)** Transformation of two spatially extended objects (blue circle and square, shown in blue) to the handspace (shown in brown and orange for touching by the upper arm and forearm, respectively). Note that the circular object can be reached by the upper arm and forearm, while the square one by the forearm only. If the objects remain static, the pink arrowed curve would represent a feasible trajectory to the target.

Case 2. Let us now consider a case similar to the one shown in Figure 5.1, where the point-like object (Fig. 5.3A, blue dot) is reachable by the forearm, i.e.

$$\vec{x} \in \mathcal{A}_2 = \overline{\mathcal{B}}_{\rho+1} \setminus \mathcal{B}_{\max\{0,1-\rho\}} \subset \mathcal{W}. \tag{5.6}$$

Then we can easily express the distance between the elbow and the object as a function of ϕ:

$$\lambda_{\vec{x}}(\phi) = (\rho^2 + \|\vec{x}\|^2 - 2\rho\|\vec{x}\| \cos\phi)^{\frac{1}{2}}. \tag{5.7}$$

Note that if a contact between the forearm and the object occurs, then $\phi \leq 0$ and $\lambda_{\vec{x}}(\phi) \leq 1$. Thus, taking

$$\phi_{\max}(\vec{x}) = \arccos\left(\frac{\rho^2 + \|\vec{x}\|^2 - 1}{2\rho\|\vec{x}\|}\right), \tag{5.8}$$

we can restrict the study to the case $\phi \in [-\phi_{\max}(\vec{x}), 0]$. All this leads to a map transformation (more details in [63])

$$E_2(\vec{x}) = \{F_2(\phi,\vec{x}) : \phi \in [-\phi_{\max}, 0]\} \subset \mathcal{H}_2, \tag{5.9}$$

where

$$F_2(\phi,\vec{x}) = \frac{\vec{x}}{\lambda_{\vec{x}}(\phi)} - \rho\left[\frac{1}{\lambda_{\vec{x}}(\phi)} - 1\right]\mathcal{M}(\vec{x})\begin{pmatrix}\cos\phi\\ \sin\phi\end{pmatrix}. \tag{5.10}$$

Note that whenever $\|\vec{x}\| \in (\rho - 1, \rho + 1]$, the point object can be reached both by the forearm and the upper arm (as in Figure 5.3A). Then the extension in the handspace splits into two different curves: E_1 (Fig. 5.3A, brown), whose equation has been given by (5.4), and E_2 (Fig. 5.3A, orange), given by (5.9). On the other hand, depending on the position of $\vec{x} \in \mathcal{W}$, some of E_j (but not both) could be empty (Fig. 5.3B, no brown extension): specifically, $E_j(\vec{x}) = \emptyset \Longleftrightarrow \vec{x} \in \mathcal{W} \setminus \mathcal{A}_j$, for $j \in \{1, 2\}$.

Thus, a globally extension of a point-like object in the handspace can be expressed as

$$\begin{array}{rccc} E: & \mathcal{W} & \rightarrow & \mathcal{P}(\mathcal{H}_2) \\ & \vec{x} & \mapsto & E_1(\vec{x}) \cup E_2(\vec{x}). \end{array} \tag{5.11}$$

The above described mapping enables compacting the limb into a point by applying compaction C, but at the same time it extends point objects into closed bounded sets by applying extension E. Then a real object with non-zero dimensions can be mapped from the workspace to the handspace by applying the transformation (5.11) to the object boundary. Figure 5.3C illustrates typical examples of mapping of objects of circular and square shapes. The circular object appears on the border delimited by the possible elbow positions and hence has two parts (orange and brown), while the square is unreachable by the upper arm and thus has only orange part.

5.2.3. Exploration of the Handspace and Generalized Cognitive Maps

Let us now consider a manipulator actuating in a dynamic situation. Then obstacles and/or targets can move in the workspace. For each time instant t the environment configuration can be transformed into the handspace as described in Section 5.2.2 and we obtain extended objects moving in the handspace. Now let us construct a GCM in this space.

To construct a GCM we simultaneously have to perform, as explained in Chapter 3: i) prediction of the obstacle movements and ii) simulation of all possible subject actions. Both calculations are performed "mentally" in a neural network and must be done faster than the time scale of the dynamic situation (for more detail see [7, 77]). Thus, in what follows we will deal with two times: i) t is the "real" time in the workspace, and ii) τ is the "mental" time used in mental calculations made by a neural network. Then having a trajectory of the hand $\vec{x}_h(\tau)$ in the handspace we will rescale time τ to implement real movement in the workspace. In Section 5.3 we will provide a verification of the results by using a 3D avatar simulating the movement of a humanoid robot. Thus, we adapt calculations to its characteristics and obtain the scaling constant $\kappa = t/\tau = 1/400$ [s].

Prediction of Object Movements

The first ingredient of a GCM is the transformation to the handspace described in Section 5.2.2. To predict the trajectories of objects in the workspace one alternative is to use a recurrent neural network that approximates trajectories by Taylor series up to quadratic terms, as done in [7, 54]. The Taylor coefficients are estimated by the network from the initial conditions provided by the sensory system of the subject. Here however we use a similar but purely computational approach. The trajectories are predicted using the initial (at $t = 0$) velocity and acceleration and taking into account physical constraints.

The displacement of an object in the workspace implies also a time-dependent adjustment of the shape of the corresponding extended object in the handspace. Indeed, Eq. (5.11) depends nonlinearly on the object position in the workspace, $\vec{x}(t)$. Thus, for each instant of the mental time τ we predict the future object position in the workspace and then evaluate its representation in the handspace by applying the transformation (5.11) to the points in the object boundary. Figure 5.4 shows a typical example of how two objects moving in the workspace can be projected into the handspace. Note the changes in the shape of the extended objects.

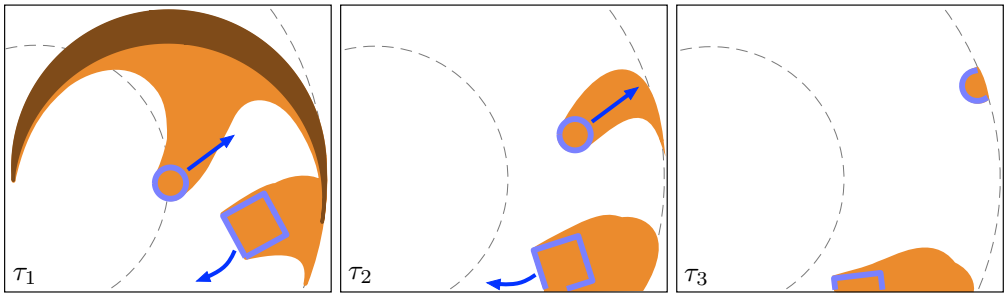

Figure 5.4: Movement of objects in the workspace (in blue) and their mapping into the handspace (brown/orange areas). Blue arrows mark directions of the object movements in the workspace. Initial situation (left panel, τ_1) corresponds to Figure 5.3. Note changes in the shape of the extended objects along the movement.

Simulation of Possible Subject Actions

According to [7] we simulate all possible hand movements in the handspace and match them with extended objects in a 2D neuronal lattice (cite Chapter 3). The lattice is composed of 80×80 locally coupled FitzHugh-Nagumo-type neurons described by the following dynamical system:

$$\begin{cases} \frac{du_{ij}}{d\tau} = q_{ij}\left(f(u_{ij}) - z_{ij} + d\Delta u_{ij}\right) \\ \frac{dz_{ij}}{d\tau} = \varepsilon(u_{ij} - 7z_{ij} - 2) \end{cases} \qquad (i,j) \in \Lambda, \qquad (5.12)$$

where $\Lambda = \{(i,j) \in \mathbb{N}^2 : \ 1 \leq i,j \leq 80\}$ is the network space; u_{ij} and z_{ij} are the membrane potential and recovering variable of neuron (i,j), respectively; Δ is the discrete 2D Laplacian; and $f(u) = (-u^3 + 4u^2 - 2u - 2)/7$ is the typical nonlinearity. In numerical experiments we set the diffusion constant to $d = 0{,}2$ and the small parameter to $\varepsilon = 0{,}04$. The selected functions and parameter values in (5.12) ensure propagation of a phase wave in the lattice. The system is considered with Neumann boundary conditions. The function $q_{ij}(\tau)$ describes effective objects and will be discussed later.

At the beginning all neurons except one are at rest ($u_{ij}(0) = z_{ij}(0) = 0$). The neuron $(i_\mathrm{h}, j_\mathrm{h})$ corresponding to the hand location has no dynamics $q_{i_\mathrm{h}j_\mathrm{h}} = 0$ and hence $u_{i_\mathrm{h}j_\mathrm{h}}(\tau) = u_{i_\mathrm{h}j_\mathrm{h}}(0) = 5 \ \forall \tau > 0$. This cell will initiate a phase wave in the lattice. Such a wave simulates all possible movements of the hand in a single run. Points on the wavefront at a time instant τ^* describe all positions virtually available to the hand. Then the wave explores the environment and finds ways to the target if they exist (for more details see [7, 54, 63]).

To illustrate the idea let us consider a situation similar to that shown in Figure 5.1, but now the point-like obstacle moves along a certain direction (Fig. 5.5A, blue arrow). In the handspace the arm is mapped into a point while the obstacle and the target are extended to curves (Fig. 5.5B). The displacement of the obstacle for $\tau > 0$ implies changes in its shape (as it happened in Figure 5.4).

Formation of Effective Static Objects

At $\tau > 0$ a wavefront propagates in the lattice (5.12) and switches cells from the initial downstate $u_{ij} = 0$ to the upstate $u_{ij} = 1$ (Fig. 5.5C). Then it is stored the time instant τ_{ij} when cell (i,j) crosses a threshold u_th (i.e., $\tau_{ij} = \min\{u_{ij}^{-1}(u_\mathrm{th})\}$ in case this potential threshold u_th is reached for some $\tau \in [0, \tau_\mathrm{max}]$; or $\tau_{ij} = \tau_\mathrm{max}$ otherwise). Thus, behind the wavefront we obtain a potential field that we can discretize through the following square matrix:

$$G = (\tau_{ij})_{i,j=1}^{80} \, . \tag{5.13}$$

The circular shape of the wavefront at the beginning (Fig. 5.5C, $\tau = 30$) means that the hand can move equally in all directions. However, this circular shape is broken once the wave starts interacting with extended objects (obstacles and targets). Such events correspond to possible collisions of the whole arm with obstacles or targets.

To explain how the GCM is constructed it is convenient to introduce the discrete mental time $n = 0, 1, \ldots$, that relates to the continuous time by $\tau = nh$, where h is the integration time step. Then we denote by Γ_n the set of cells $(i,j) \in \Lambda$ occupied by objects at the time

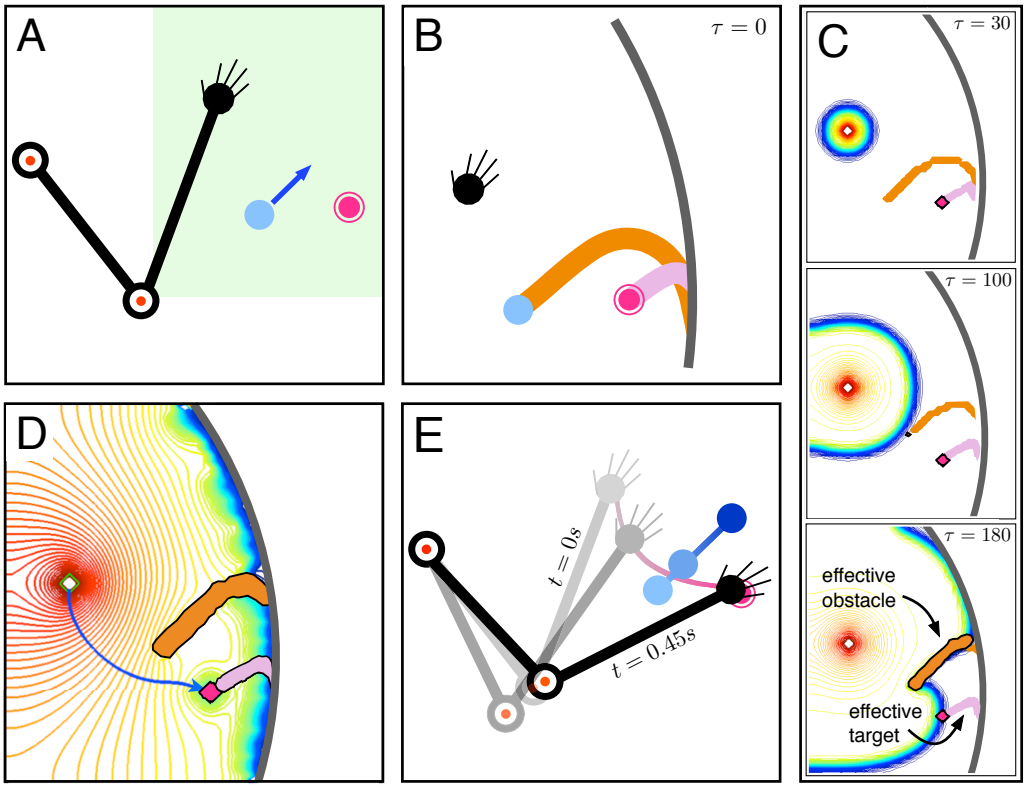

Figure 5.5: Generalized Cognitive Map representing and driving a manipulator in a simple dynamic situation. **A)** Initial situation similar to Figure 5.1. The obstacle (blue circle) moves along the direction shown by blue arrow. The hand should reach the target (pink circle) and avoid collision with the obstacle. **B)** The situation (for $\tau = 0$) in the handspace. The arm is reduced to a point (black circle), while the extended obstacle and target are shown in orange and purple. **C)** The process of generation of a GCM. Snapshots illustrate a traveling wavefront exploring the environment. **D)** The GCM of the situation. The static effective obstacle and target are outlined in orange and purple. Blue arrowed curve marks the shortest feasible path to the target (the highlighted border of the extended target corresponds to a collision with the hand, which is the final purpose). **E)** Limb movement in the workspace (superimposed snapshots with darker colors correspond to progressively increasing time instants).

instant nh. We also define the following iterative process:

$$\begin{cases} \Omega_0 = \{(i_{\mathrm{h}}, j_{\mathrm{h}})\} \\ \Omega_n = \Omega_{n-1} \cup \delta\Omega_n, \quad n = 1, 2, \ldots, \end{cases} \tag{5.14}$$

where $\delta\Omega_n = \{(i,j) \in \Gamma_n : \ u_{ij}(nh) \in [1,2], \ \ (i,j)\}$. The set Ω_n describes effective objects in the network space Λ. It is dynamically created as the wavefront explores Λ. Then we define

the binary coefficient used in Eq. (5.12):

$$q_{ij}(\tau) = \begin{cases} 0 & \text{if } (i,j) \in \Omega_n \\ 1 & \text{otherwise,} \end{cases}$$

where $\tau \in [h(n-1), hn)$. The cells in Ω_n have $du/d\tau = 0$ for $\tau \geq nh$ and hence will exhibit no dynamics, i.e., the effective objects are *static* and the wavefront slips around them (Fig. 5.5C, $\tau = 100$ and $\tau = 180$).

We note that although Λ is a square lattice, only the exploration of a part of it can be of interest. The hand cannot reach locations outside the disk $\overline{\mathcal{B}}_{\rho+1}$ neither inside $\mathcal{B}_{\max\{0,\rho-1\}}$. Thus, we can add artificial obstacles at the border of these two regions, which will restrict the wave propagation (Fig. 5.5C, black circle-like curve). Once the wave exploration of Λ has been finished, the created potential field $G = (\tau_{ij}) \in \mathcal{M}_{80\times 80}$ represents a Generalized Cognitive Map of the situation (Fig. 5.5D). It contains spatiotemporal relationships among the hand and other objects in the workspace structured as static effective objects in the handspace. These effective objects contain critical information about possible collisions of the fore/upper arm with objects (to be avoided) and hand with the target (to be caught, see Figure 5.5D, fucsia dot of the extended target).

Motor Execution

Once the wave has explored the handspace, we get a potential field (5.13) and effective static objects (see Figures 5.5C, 5.5D). These taken together represent a Generalized Cognitive Map of the situation. The effective objects contain critical information about possible collisions of the limb with the objects in the workspace. The gradient profile of the potential field ∇G imposes rules the limb should follow to reach the target.

We thus use a gradient descend method to find feasible trajectories connecting the initial location of the hand and the real (non-extended) target positions (Fig. 5.5D, blue arrowed curve). By construction such a trajectory circumvents effective obstacles in the handspace. However, what is more important, if the hand follows this trajectory, then in the workspace (i) the hand will reach the target; and (ii) during the move the limb will not bump against obstacle.

Therefore, in order to solve the dynamical situation in the workspace we use the trajectory obtained in the handspace and implement kinematic movements of the limb in such a way that the hand would follow this trajectory. Figure 5.5E shows three superimposed snapshots of the moving manipulator and obstacle in the workspace. The manipulator successfully accomplishes the task "reach the target and avoid collisions with obstacles", as expected.

5.3. Validation in a 3D Avatar

The proposed approach builds a basis for cognitive manipulators working in time-evolving situations. Note that a rather simple situation represented in Figure 5.5 has been used for illustration purpose only. The concept applies to situations of practically arbitrary complexity including 3D scenes.

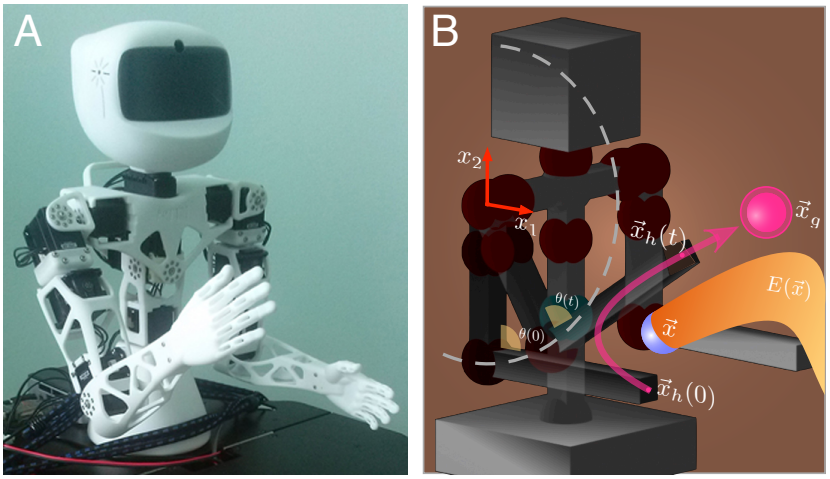

Figure 5.6: Setup for testing cognitive manipulation. **A)** Torso (upper part) of a humanoid robot Poppy. **B)** Avatar of the robot used in numerical tests of the cognitive model of a limb.

For testing purposes we built an avatar of a humanoid robot Poppy Torso (Fig. 5.6). The avatar uses server-client architecture and can receive motor commands through an interface from a MatLab script by means of the tcp-ip protocol. Then it can either reproduce movements on a computer screen or in a real robot in real time. In this work we, however, restricted ourself to the former option.

Cognitive manipulation in 3D space can be straightforwardly tackled by the concept of GCMs in the hand space described in Section 5.2. However, it implies constructing extended objects and simulating phase waves in 3D space, which requires significantly higher computational resources. Nonetheless, a simpler approach to 3D dynamic situations can be applied.

Figure 5.7A shows a 3D dynamical situation. The limb should catch a ball falling due to the gravity force and avoid collision with a fixed horizontal bar. We then can assume that the limb movements are restricted to the plane P formed by the upper arm and forearm. Then the 3D problem is reduced to considering a two-joint manipulator on a plane with 2D objects obtained by intersecting 3D objects (the ball and the bar) with the plane (Fig. 5.7B). Note that the latter problem is equivalent to the problem shown in Figure 5.5, but now the target is mobile and the limb should intercept it. Thus, we can apply directly the procedure described in Section 5.2.

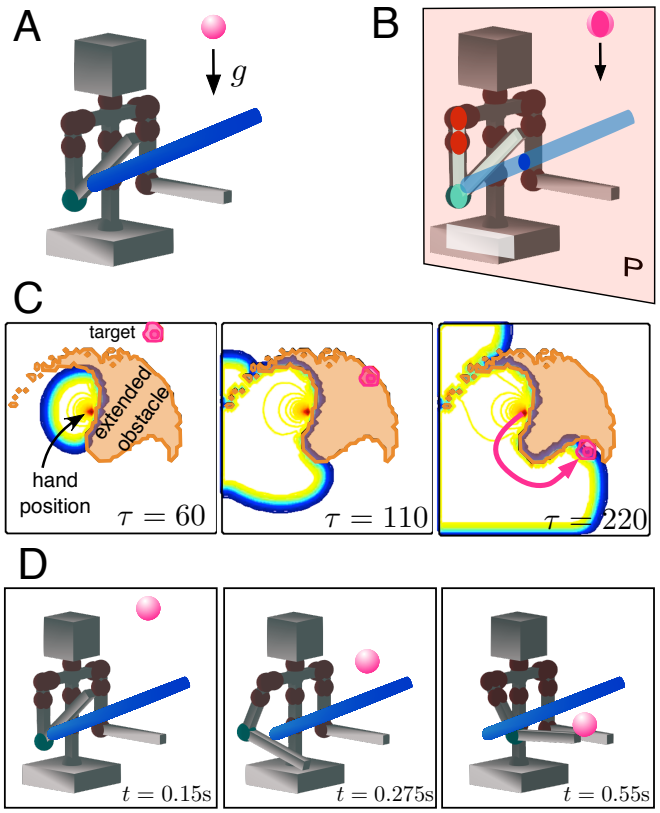

Figure 5.7: Cognitive movement of a robotic manipulator in 3D space. **A)** Dynamic situation. The robot catches a falling ball (in pink) in the presence of an obstacle (horizontal bar, in blue). **B)** Given that the limb moves in plane P the problem is reduced to a 2D situation. **C)** Snapshots of the wave generating a GCM in mental time τ. The static extended obstacle and the real (non-extended) target are drawn in orange and pink, respectively. Arrowed curve marks the hand trajectory to intercept the falling ball with the hand. **D)** Simulation of the limb movement in real time t.

In the 2D projection the static obstacle (blue bar) and the moving target (pink ball) are represented by the corresponding disks. Since the obstacle is static its representation in the handspace will be also static (Fig. 5.7C, orange area). For the sake of clarity, here we don't show the extension of the target in the handspace, but represent only the mapping of the falling ball (Fig. 5.7C, pink disk). Then the wave process similar to that shown in Figure 5.5 starts. The wave propagates from the hand position outwards and matches all possible hand movements with the target motion. We search for a contact of the wave with the non-extended target, which occurs at mental time $\tau = 220$ (Fig. 5.7C).

Once a contact of the wave with the real target has been achieved, we can stop the calculation and draw a curve from the initial hand position to the place of contact following the gradient of the field G (Fig. 5.7C, panel $\tau = 220$, arrowed curve). Now this trajectory can be implemented in the avatar in real time t. Figure 5.7D shows snapshots of the manipulator movements in the workspace and real time t.

5.4. The Model for redundant limbs

We will show that the approach presented in Section 5.2 is scalable to limbs with redundant numbers of degrees of freedom. In this section we provide a more general neural network model capable of driving a 3DoF limb in different time-evolving situations. For example, the limb should kick a falling ball and simultaneously avoid collisions with other, in general moving, objects.

5.4.1. The 3DoF manipulator

Figure 5.8 illustrates a kinematic model of an upper limb consisting of three segments moving in a two-dimensional workspace $\mathcal{W} \subset \mathbb{R}^2$. The limb shoulder is fixed at the origin of the plane (x_1, x_2) and it is joined to an articulated elbow by a rigid segment of length ρ. A forearm of length l joins the elbow with a hand at $\vec{x}_h \in \mathcal{W}$. The wrist can flex thus changing the angle of the last limb segment of length h.

As before, to generalize further calculations we rescale the spatial coordinates in such a way that the length of the forearm is $l = 1$ a.u. We then restrict the limb's workspace to:

$$\mathcal{W} = \overline{\mathcal{B}}_{\rho+1+h} \setminus \{\vec{0}\} \subset \mathbb{R}^2, \tag{5.15}$$

i.e., to a disk of radius $(\rho + 1 + h)$ centered at the origin.

The shoulder, elbow, and wrist joints can freely rotate within specific angular limits that depend on the internal limb structure. Thus, we have three degrees of freedom in a 2D workspace and hence the upper limb is redundant. The goal is to touch by the hand (any point in the last segment) a target avoiding collisions with obstacles.

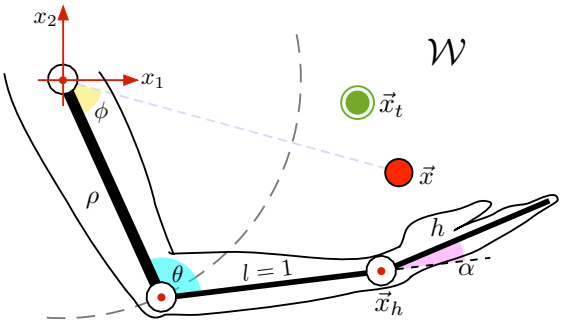

Figure 5.8: Model of an 3DoF upper limb in a 2D workspace $\mathcal{W}$. The shoulder is fixed at the origin. The upper arm, forearm, and hand have lengths ρ, $l = 1$, and h a.u., respectively. The upper arm forms an angle ϕ with the direction to a point-like obstacle located at $\vec{x}$ (red circle). The forearm has an angle θ with the upper arm, and α is the angle of the hand. The limb segments can freely rotate within specific limits (around red points in open circles). The goal is to reach a target at $\vec{x}_t$ (green circle) by the hand avoiding collisions.

Figure 5.8 illustrates a simple situation with a point target and a point obstacle, marked by $\vec{x}_t$ and $\vec{x}$, respectively. Further we will generalize this setting into a situation with multiple moving targets and obstacles of arbitrary shapes. We also note that the target cannot be touched by the upper arm and forearm, i.e., it plays the role of an obstacle for these segments of the limb.

5.4.2. Transformation to the 3D Handspace

Dealing with an additional degree of freedom involves redefining the handspace introduced in Section 5.2.2:

$$\mathcal{H}_3 = \left(\overline{\mathcal{B}}_{1+\rho} \setminus \mathcal{B}_{\max\{0,1-\rho\}}\right) \times J \subset \mathbb{R}^3, \tag{5.16}$$

where $J = [\alpha_{\min}, \alpha_{\max}]$ is the feasible interval of the wrist angle. Thus, $\mathcal{H}_3$ is a cylinder with a hole in the center. For the sake of simplicity and without loss of generality, in what follows we assume $\rho \geq 1$. Then $\mathcal{H}_3$ is a cylinder without the line in the center $\{(0,0)\} \times J$.

Note that $\dim(\mathcal{H}_3) = 3 > 2 = \dim(\mathcal{W})$ and hence we deal with a redundant limb. We can also consider a reduction of the handspace (5.16) into two dimensions. In case the hand angle α (Fig. 5.8) is fixed (i.e., the wrist is rigid), the limb is minimalistic ($\mathrm{DoF} = \dim(\mathcal{W})$) and $\mathcal{H}_3 = \mathcal{H}_2 \times \{\alpha\}$ becomes $\mathcal{H}_2$, a disk without a point at the origin.

The technique to introduce a mapping from $\mathcal{W}$ to $\mathcal{H}_2$ has been described in Section 5.2.2. Here we provide its extension to the 3D case.

Compaction of the Limb

Similar to Section 5.2.2, the mapping of the limb is given by:

$$\begin{array}{rccc} C: & \mathcal{P}(\mathcal{W}) & \to & \mathcal{H}_3 \\ & L & \mapsto & C(L) = (\vec{x}_h, \alpha), \end{array} \tag{5.17}$$

where $L \subset \mathcal{W}$ now represents the union of the upper arm, forearm, and hand segments. Thus, the whole limb is reduced to a single point located at the hand configuration $(\vec{x}_h, \alpha) \in \mathcal{H}_3$.

Extension of Objects

While the limb is mapped into a point in the handspace, the mapping of objects goes in the opposite way. If a point-like object was extended into a set of curves in $\mathcal{H}_2$ (Sect. 5.2.2), now the extension comprises a set of surfaces in $\mathcal{H}_3$. Each surface corresponds to collisions of the point object with any different point along the whole limb. Geometrically, such an extended object represents the locus of wrist locations $\vec{x}_h$ and hand angles α while the limb slides around the object in the workspace.

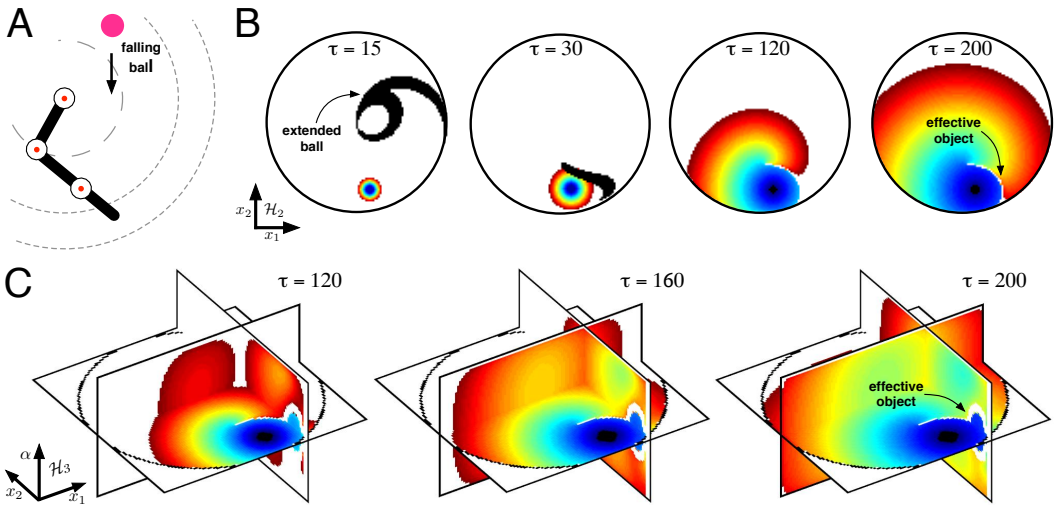

Figure 5.9: Wave exploration of the handspace for a dynamic situation. **A)** Simple dynamic situation. A hand (last segment of the limb shown in black) should kick a falling ball (in pink). The limb can have either 2 DoF (i.e., the wrist joint is fixed) or 3 DoF (the wrist is flexible). Gray circles mark regions reachable by different segments. **B)** The process of generation of a generalized cognitive map for the limb with 2 DoF in the hand space $\mathcal{H}_2$. Successive snapshots illustrate a traveling wavefront exploring the environment and the extended object corresponding to the falling ball (in black, snapshots $\tau = 15$, $\tau = 30$). The wave generates a potential field (colors from blue to red) and an effective object (in white, snapshot $\tau = 200$). **C)** The same as in (B) but for the limb with 3 DoF in the hand space $\mathcal{H}_3$.

To understand the new mapping to the new 3D handspace, let us start considering a limb trying to catch a falling ball (Fig. 5.9A) keeping the wrist rigid. If $J = \{0\}$, i.e., $\alpha_{\min} = 0 = \alpha_{\max}$, then $\mathcal{H}_3 = \mathcal{H}_2 \times \{0\}$ and the situation can be mapped as in the 2D case. Figure 5.9B illustrates the changing shape and the displacement of the extended ball in $\mathcal{H}_2$ (black areas in snapshots corresponding to the mental time $\tau = 15$ and $\tau = 30$), linked with the different positions occupied by the real ball in the workspace $\mathcal{W}$.

Similar but even more evolved representations of the extended 3D object can be obtained in $\mathcal{H}_3$ when $\alpha_{\min} \neq \alpha_{\max}$. Let us now describe the mapping. We consider a point object located at some fixed t at $x \in \mathcal{W}$. Then the map extending the point can be expressed as

$$\begin{array}{rccc} E: & \mathcal{W} & \to & \mathcal{P}(\mathcal{H}_3) \\ & x & \mapsto & E(\vec{x}). \end{array} \tag{5.18}$$

Since an object can collide with three limb segments, $E(\vec{x}) = E_1(\vec{x}) \cup E_2(\vec{x}) \cup E_3(\vec{x})$, where $E_{1,2,3}$ represent the extensions due to collisions with upper arm, forearm, and hand, respectively. Note that $E_{1,2}$ are built copying the corresponding expansions in $\mathcal{H}_2$ along the third dimension, since the collisions with the upper arm or the forearm don't depend on the angle of the hand segment. Also, as in the 2D case, depending on the position of the object $\vec{x}$, some of E_j can be empty (e.g., if $x \notin \overline{\mathcal{B}}_\rho$ then $E_1(\vec{x}) = \emptyset$).

Case 1. If the object is reachable by the upper arm, we obtain the expansion

$$E_1(\vec{x}) = \{F_1(\theta, \vec{x}) : \theta \in [0, \pi]\} \times J, \tag{5.19}$$

where F_1 is the application defined in 5.5.

Case 2. Let us assume that the object is reachable by the forearm. Then the expansion is given by

$$E_2(\vec{x}) = \{F_2(\phi, \vec{x}) : \phi \in [-\phi_{\max}, 0]\} \times J, \tag{5.20}$$

where $\phi_{\max}$ is the angle defined in 5.8 and F_2 is the application built in 5.10.

Case 3. Assuming that the hand forms an angle $\alpha \in J$ and is in contact with the point-object $\vec{x}$ at a distance $d = \|\vec{x} - \vec{x}_h\| < h$, then the expansion of the object is given by

$$E_3(\vec{x}) = \{F_3(d, \alpha, \vec{x}) : d \in [d_{\min}, h], \alpha \in J\}, \tag{5.21}$$

where

$$F_3(d, \alpha, \vec{x}) = \vec{x}_e + \frac{\operatorname{sign}(\alpha)}{\beta_{\vec{x}} \|\vec{x} - \vec{x}_e\|} (I_2 + dR_\alpha)(\vec{x} - \vec{x}_e), \tag{5.22}$$

R_α is the standard clockwise rotational matrix, and

$$\beta_{\vec{x}} = (1 + d^2 + 2d\cos\alpha)^{\frac{1}{2}} \tag{5.23}$$

is the distance between the object and the elbow, located in

$$\vec{x}_e = \frac{1}{2\|\vec{x}\|} \mathcal{M} \begin{pmatrix} \|\vec{x}\|^2 + \rho^2 - \lambda_{\vec{x}}^2 \\ -\left[(2\|\vec{x}\|\rho)^2 - (\|\vec{x}\|^2 + \rho^2 - \lambda_{\vec{x}}^2)^2\right]^{\frac{1}{2}} \end{pmatrix}. \tag{5.24}$$

The lower bound for d in (5.21) is given by

$$d_{\min}(\alpha, \vec{x}) = \left[(\|\vec{x}\| - \rho)^2 - \sin^2\alpha\right]^{\frac{1}{2}} - \cos\alpha. \tag{5.25}$$

if it is positive, or $d_{\min} = 0$ otherwise.

Finally, when dealing with a real object of an arbitrary shape, the transformation (5.18) is applied to the object's boundary. This generates extended objects occupying areas in $\mathcal{H}_2$ (see, e.g., Figure 5.9B, panel $\tau = 15$) or volumes in $\mathcal{H}_3$ (only partially shown in Figure 5.9C for visual clarity).

5.4.3. Exploration of the Handspace and Generalized Cognitive Maps

As mentioned in Section 5.2.3, to construct a GCM we perform: i) prediction of the objects' movements and ii) simulation of all possible subject actions matched with objects' movements. As seen above, there are several ways to solve the first problem (see, e.g., [7, 54, 63]). For the sake of simplicity, here we assume that the trajectories of all objects are given and hence we will concentrate on solving the second, much more complex task.

Using the predicted trajectories of the objects in the workspace we can evaluate for each time instant τ their extended images in the handspace (Fig. 5.9B, black areas). Then we can simulate all possible hand movements by a wave. In the handspace $\mathcal{H}_3$ the wave is initiated at the location of the wrist and initial hand angle $(\vec{x}_h(0), \alpha(0))$, whereas in $\mathcal{H}_2$ it starts from $\vec{x}_h(0)$ $(\alpha = 0)$. Figures 5.9B and 5.9C illustrate the wave propagation process in $\mathcal{H}_2$ and $\mathcal{H}_3$, respectively.

The set of points on the wavefront represents all possible configurations of the limb (wrist location and hand angle) at time τ. If the wavefront collides with an extended object then such an event corresponds to a possible collision of the limb and the object. Then at the locations of such collisions in the handspace we create effective static objects.

Figures 5.10A and 5.10B illustrate the shapes of the effective static objects obtained in $\mathcal{H}_2$ and $\mathcal{H}_3$, respectively (see also Figures 5.9B and 5.9C, panels $\tau = 200$). In both cases one part (shown in green) of the effective object corresponds to a target, i.e., to collisions of the ball with the hand in the workspace, while the other one (shown in red) marks collisions of the ball with forearm. Thus, the effective static objects should be either avoided (obstacles) or reached (targets). Using the potential field (Figs. 5.9B, 5.9C, $\tau = 200$) and the effective objects (Figs. 5.10B, 5.10C) we can trace different trajectories to the target.

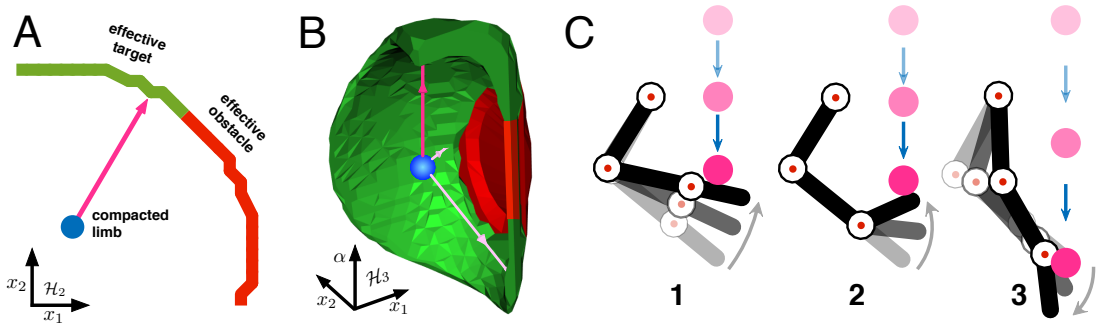

Figure 5.10: Effective static objects and execution of limb movement for the situation shown in Figure 5.9. **A)** Effective object in $\mathcal{H}_2$ (amplified from Figure 5.9B, $\tau = 200$) contains two parts: effective target (in green) and effective obstacle (in red). **B)** Same as in (A) but in $\mathcal{H}_3$. **C)** Three representative examples of limb movements receiving the ball with significantly different hand angles. Only panel 1 is available for a 2DoF manipulator, whereas Panels 1–3 are available for a 3DoF manipulator.

Let us now implement the wave process leading to formation of effective objects and a potential field guiding the limb.

Simulation of Possible Subject Actions

In Section 5.2.3 we considered 2D internal representations of workspaces and postulated a constant velocity c for the explorative wave [7, 63, 120]. This is equivalent to considering the handspace $\mathcal{H}_2$ of the limb with a rigid wrist. Then the velocity of the wrist $\vec{v} = d\vec{x}_h/dt \in \mathbb{R}^2$ will satisfy $\|\vec{v}\| = c$ (implementing, e.g., maximally fast displacement).

Now we take into account rotation of the wrist joint with an angular velocity $\omega = d\alpha/dt \in \mathbb{R}$. Then we impose the following constraint on the compound velocity:

$$\|\vec{v}\|^2(t) + \gamma_0\omega^2(t) = c^2, \tag{5.26}$$

where γ_0 is the bias between the velocity of motions in (x_1, x_2)-plane and rotation of the wrist. Note that such a formulation is similar to fixing the kinetic energy of the limb.

To account for constraint (5.26) in the handspace $\mathcal{H}_3$ we design a neural network in the form of a 3D cylindrical lattice:

$$\Lambda = \left\{(i,j,k) \in \mathbb{Z}^3 :\ i^2 + j^2 \le r^2,\ 1 \le k \le K\right\}, \tag{5.27}$$

where the constant $r \in \mathbb{N}$ defines the spatial resolution in (x_1, x_2) and is linked with the value $(\rho + 1)$; $K \in \mathbb{N}$ defines the resolution for the wrist flexions, linked with $|J|$.

On the lattice Λ we define the following dynamical system:

$$\frac{du_I}{d\tau} = q_I\big(f(u_I) + d_0(\Delta_x + \gamma\Delta_\alpha)u_I\big), \tag{5.28}$$

where $I = (i,j,k) \in \Lambda$; u_I is the membrane potential of neuron I; Δ_x, Δ_α are the discrete Laplacians in the corresponding variables; and $f(u) = u(u-0{,}1)(1-u)$ is the cubic nonlinearity, selected to ensure propagation of waves in the lattice. The binary function $q_I(\tau) \in \{0,1\}$ describes formation of effective objects and will be discussed later. The diffusion coefficient d_0 can be adjusted to account for the velocity of the arm movements in the workspace c and the velocity bias

$$\gamma = \gamma_0 \frac{(\rho+1)^2K^2}{r^2|J|^2}. \tag{5.29}$$

We note that for $\gamma = 0$, Eq. (5.28) is reduced to the system on a disk (e.g., in $\mathcal{H}_2$). It corresponds to movements with a rigid wrist joint. Thus, model (5.28) generalizes our previous developments restricted to $\mathcal{H}_2$ (Sect. 5.2.3). The other limit $\gamma \to \infty$ and $d_0\gamma = \mathrm{const}$ corresponds to the situation where the wrist flexion is the only available movement, i.e., we force the upper arm and forearm to stay still.

The dynamical system (5.28) is considered with Neumann boundary conditions (on the cylinder and extended objects). At the beginning the neurons are set to $u_I(0) = 0\ \forall I \in \Lambda \setminus S$, $u_I(0) = 1\ \forall I \in S$, where S is a small spheroid region centered at the initial hand position $I_h(0)$ and with the eccentricity defined by γ. Such an initial condition ensures correct formation of a spheroid wavefront at the beginning of integration of (5.28). We also note that $q_I(\tau) = 0\ \forall I \in S$ and hence $u_I(\tau) = 1\ \forall \tau \geq 0$.

Formation of Effective Static Objects

At $\tau > 0$ a wavefront propagates in the lattice (5.28) and switches cells from the initial downstate ($u_I = 0$) to the upstate ($u_I = 1$). Figures 5.9B and 5.9C show the wavefront simulating the same dynamic situation (Fig. 5.9A) but in $\mathcal{H}_2$ and $\mathcal{H}_3$, respectively. It is stored he time instant τ_I when cell I crosses a threshold $u_{\rm th}$ (i.e., $\tau_I = \min\{u_I^{-1}(u_{\rm th})\}$, in case $u_{\rm th}$ is reached by I in some $\tau \in [0, \tau_{\max}]$; or $\tau_I = \tau_{\max}$ otherwise). Thus, behind the wavefront we obtain a potential field that we can express through the following 3D matrix (color coded in Figures 5.9B, 5.9C):

$$G = (\tau_I)_{I \in \Lambda}\,, \tag{5.30}$$

The circular shape (spheroid in $\mathcal{H}_3$) of the wavefront at the beginning (Fig. 5.9B, $\tau = 15$) means that the hand can move equally well in all directions. However, this circular shape is broken once the wave approaches an extended object (Fig. 5.9B, $\tau = 30$). Such events correspond to possible collisions of the limb with the object. Part of these represent collisions with the forearm and the others with the hand (Figs. 5.10A, 5.10B). The former should be avoided, whereas the latter is desired (the hand kicks the target in mental simulation). We note that the process of collision of the wave with an extended object technically is similar in $\mathcal{H}_2$ and $\mathcal{H}_3$. However, in the latter case the wave propagates in 3D and the resulting collisions can produce much more evolved forms, in general not reducible to $\mathcal{H}_2$.

Let us now provide mathematical details for the process of formation of effective obstacles in neural network (5.28). It is convenient to introduce the discrete mental time $n = 0, 1, \ldots$ that relates to the continuous time by $\tau = hn$, where h is the integration time step. Then we denote by Γ_n the set of cells $I \in \Lambda$ occupied by the extended objects at time instant $\tau = hn$ in the hand space and define the following iterative process:

$$\begin{array}{l} \Omega_0 \leftarrow S \\ \Omega_n \leftarrow \Omega_{n-1} \cup \delta\Omega_n, \quad n = 1, 2, \ldots \end{array} \tag{5.31}$$

where $\delta\Omega_n = \{I \in \Gamma_n :\ u_I(hn) \in [0{,}4, 0{,}7]\}$.

The dynamical set Ω_n describes cells occupied by effective objects in the network space Λ

at time n. It can only grow as the wavefront explores Λ. Then we define:

$$q_I(\tau) = \begin{cases} 0 & \text{if } I \in \Omega_n \\ 1 & \text{otherwise.} \end{cases} \tag{5.32}$$

where $\tau \in [h(n-1), hn)$. Thus cells in Ω_n have $du_I/d\tau = 0$ for $\tau \geq hn$ (see Eq. (5.28)) and hence will exhibit no dynamics in the forward time, i.e., the effective objects are *static* and the wavefront slips around them (Figs. 5.9B, $\tau = 120$ and $\tau = 200$).

Motor Execution

Once the wave has explored the handspace, we get a potential field (5.30) and effective static objects (see Figures 5.9 and 5.10, respectively). These taken together represent a Generalized Cognitive Map of the situation. The effective objects contain critical information about possible collisions of the limb with the objects in the workspace. The gradient profile of the potential field ∇G imposes rules the limb should follow to reach the target.

We thus use a gradient descend method to find feasible trajectories connecting positions of the effective target and the initial location of the limb $I_h(0)$. Figures 5.10A and 5.10B (arrowed curves) show three representative examples of the trajectories. By construction of the field with a wavefront, such trajectories circumvent effective obstacles in the handspace. However, what is more important, if the limb follows one of the trajectories in the workspace [7]: (i) the hand will reach the target; (ii) during the move the limb (forearm and upper arm) will not bump against obstacles.

5.5. Comparison of minimalistic and redundant models

In order to actuate in a given dynamical situation we use one of the trajectories obtained in the handspace. Figure 5.10C shows examples of the motor executions in the workspace. In both cases the limb successfully accomplishes the task "reach the target and avoid collisions with obstacles", as expected. However, in the 2DoF case the repertoire of possible angles of the hand when kicking the ball is very limited (panel 1 in Figure 5.10C). Playing a game the ball only can be rebound to the "up-right". The handspace $\mathcal{H}_3$ provides significantly reacher dynamics. In this case we can easily choose the desired kick angle by selecting the value $\alpha(\tau_{\text{end}})$. For example, Figure 5.10C exemplifies two other choices that lead to kicks to the "up-left" and to the "right" (panels 2 and 3, respectively).

The dynamic situation described above was intentionally selected simple enough. Nevertheless, the discussed approach is aplicable to situations of arbitrary complexity. To illustrate the potential of the method let us consider a situation similar to that shown in Figure 5.9A, but now with an extra obstacle (Fig. 5.11A). In this case the falling ball is reachable for the limb during some time interval only. Then it hides behind the bar.

We repeated simulations described in previous sections. Figure 5.11B shows the effective static objects in the handspace $\mathcal{H}_3$. Now the part corresponding to obstacles (in red) is much bigger than in Figure 5.10B. We also notice that the target (in green) does not intersect the plane $\alpha = 0$ (shown in yellow). This means that there is no valid trajectory to the target in the case of the rigid wrist. A valid trajectory should necessarily change the hand angle $\alpha(t)$ (rose arrowed curve in Figure 5.11B). Although there is no trajectory with $\alpha = 0$ we can find one that goes closely to the target (blue arrowed curve in Figure 5.11B).

Figure 5.11C shows examples of motor execution of limb movements given by the trajectories shown in Figure 5.11B. As expected the limb with 3DoF (panel 1) intercepts the ball while the limb with 2DoF fails.

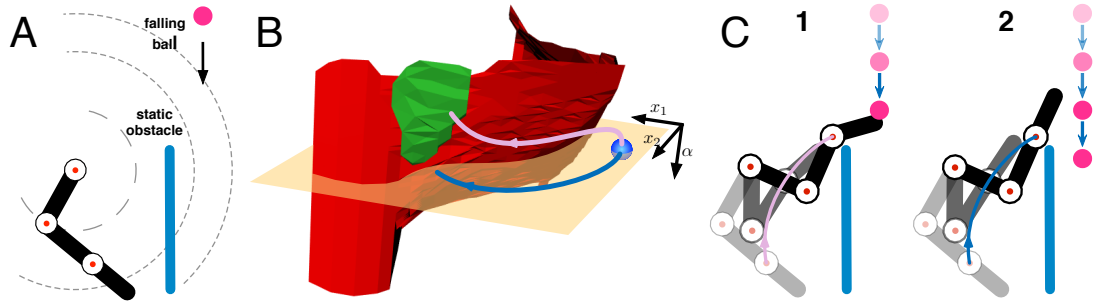

Figure 5.11: Advantage of a limb with 3DoF vs 2DoF. **A)** Situation similar to Figure 5.9A but now with an extra obstacle that "hides" the falling ball. **B)** Effective objects in the handspace $\mathcal{H}_3$. The obstacle is shown in red and the target in green. Yellow plane corresponds to $\alpha = 0$. Blue circle marks the initial position of the limb. To catch the ball it is necessary to flex the wrist joint (rose trajectory with decreasing $\alpha(\tau)$. Blue trajectory in the plane $\alpha = 0$ fails to reach the target. **C)** Examples of motor execution of trajectories shown in B. In the case of a limb with flexible wrist the ball can be caught (panel 1), whereas the 2DoF limb cannot reach the target (panel 2).

5.6. Conclusions

In this chapter we have discussed and numerically verified a novel approach based on the use of dynamical systems and neural networks that allows solving the problem of object handling and manipulation on an abstract cognitive level. The model has no restrictions about the obstacle positions and movement in the workspace, and can be used for decision-making in limbs with both minimal and redundant numbers of DoF. Thus, the approach is scalable, which is crucial for implementation in humanoid robots. We also note that the model naturally enables biasing the efforts of reaching a target among different DoF. Such an ability is frequently observed in humans playing sport games.

The approach consists in two steps: i) Transformation of the problem from the workspace to the so-called handspace, and ii) Construction of the so-called Generalized Cognitive Map in the handspace. The first step enables reduction of the limb to a point in the handspace. At

the same time obstacles are transformed into spatially extended objects of complex exotic shapes. The latter, however, is not a problem for construction of GCMs. The handspace is a specific version of the configuration spaces frequently used for description of limbs. However, instead of using the standard approach through joint angles, in our case the handspace is isometric to the workspace. The second step is performed by a wave propagating, in general, in a 3D neural network. The wave explores "mentally" the environment in the handspace and matches possible limb movements with changes in the environment. It allows converting a dynamic situation into a static representation, i.e., into a GCM. The resulting GCM contains both the information required to understand the situation and that needed to interact with it. Finally, trajectories provided by GCMs in the handspace guarantee collision-free movement of the limb in the workspace.

In order to demonstrate the feasibility of the proposed approach we have developed a 3D avatar (specific software) of a humanoid robot Poppy (Torso). Our experiments have shown that indeed the robot can operate with moving objects in the presence of obstacles. We remark that despite the apparent simplicity of the considered situations, similar experiments in humans may yield occasional failures [63]. This shows that even simple dynamic situations can puzzle our brain. Indeed, accurate and fast limb movement in a complex situation requires intensive training. In this regard one can naturally distinguish: i) static situations (e.g., playing piano) and ii) dynamic situations (e.g., playing basketball). In both cases training aims at automatizing the complex body movements. Such a learning process can be considered somehow straightforward in static scenarios. However, to imagine how it can be possible in dynamic situations is intriguing.

The terms "cognitive" and "automatic" may seem contradictory. The GCM theory provides a functional framework explaining how automation could be possible in dynamic situations. Indeed, as we have shown, dynamic situations can be represented by static GCMs. Then the difference between dynamic and static situations disappears in the brain. Moreover, this also enables classification of complex dynamic situations into well-structured sets of memories and experiences by means of standard methods of data clustering and machine learning. Concluding, the theory of generalized cognitive maps provides a functional bridge between effective cognition, dealing with direct interaction in the workspace and abstract cognition, whose impact over subject's behavior is less immediate but much more profound.

6 | Codifying memories: The high-dimensional brain

Codifying memories is one of the fundamental problems of modern Neuroscience. The functional mechanisms behind remain largely unknown. An experimental evidence suggests that some of the memory functions are performed by stratified brain structures as, e.g., the hippocampus. In this particular case, single neurons in the CA1 region receive a highly multidimensional input from the CA3 area, which is a hub for information processing. We thus assess the implication of the abundance of neuronal signaling routs converging onto single cells on the information processing. We show that single neurons can selectively detect and learn arbitrary information items, given that they operate in high dimensions. The argument is based on Stochastic Separation Theorems and measure concentration phenomena. We demonstrate that a simple enough functional neuronal model is capable of explaining:

1. Extreme selectivity of single neurons to the information content.
2. Simultaneous separation of several uncorrelated stimuli, or informational items, from a random large stimuli set by a single neuron.
3. Dynamic learning of new items by associating them with already "known" ones.

These results constitute a basis for organization of complex memories in ensembles of single neurons. Moreover, they show that no *a priori* assumptions on the structural organization of neuronal ensembles are necessary for explaining basic concepts of static and dynamic memories.

6.1. Introduction

The human brain is arguably amongst the most sophisticated and enigmatic nature creations. Over millions of years it has evolved to amass billions of neurons, featuring on average 86×10^9 cells [137]. This remarkable figure is several orders of magnitude higher than that of the most mammals and several times larger than in primates [138]. Whilst measuring roughly $2\,\%$ of the body mass, the human brain consumes about $20\,\%$ of the total energy [139].

The significant metabolic cost associated with a larger brain in humans, as opposed to mere body size (a path that great apes might have evolved [138]), must be justified by evolutionary advantages. Some of the benefits may be related to the development of a remarkably important social life in humans. This, in particular, requires extensive abilities in formation of complex memories. Indirectly this hypothesis is supported by the significant difference among species in the number of neurons in the cortex [140] and the hippocampus [141]. For example, in the CA1 area there are $0{,}39 \times 10^6$ pyramidal neurons in rat, $1{,}3 \times 10^6$ in monkey, and 14×10^6 in human.

Evolutionary implications in relation to cognitive functions have been widely discussed in the literature [142, 143, 144]. Recently, it has been shown that in humans new memories can be learnt very rapidly by supposedly individual neurons from a limited number of experiences [145]. Moreover, neurons can exhibit remarkable selectivity to complex stimuli, the evidence that have led to debates around the existence of the so-called "grand mother" and "concept" cells [146, 147, 148], and their role as elements of a declarative memory. These findings suggest that not only the brain can learn rapidly but also it can respond selectively to "rare" individual stimuli. An experimental evidence indicates that such a cognitive functionality can be delivered by single neurons [145, 146, 147]. The fundamental questions, hence, are: *How is this possible?* and *What could be the underlying mechanisms implementing such a functionality?*

Recent theoretical advances achieved within the Blue Brain Project show that the brain can operate in many dimensions [149]. It is claimed that the brain has structures operating in up to eleven dimensions. Groups of neurons can form the so called cliques, i.e., networks of specially interconnected neurons that generate precise representations of geometric objects. Then the dimension grows with the number of neurons in the clique. Other approach to a multidimensional representation of spatiotemporal information in the brain relies on the generalized cognitive maps (see, e.g., [54, 63, 77, 81]). Within this concept time-evolving information from the environment goes through a specific transformation and finally is coded as a point in $\mathbb{R}^n$ space. These information items (maps) can be learnt, classified, and retrieved on purpose. However, how the brain or individual neurons can distinguish among a huge number of different maps and select an appropriate one remain largely unknown.

In this chapter we propose that brain areas with a predominant laminar topology and abundant signaling routs simultaneously converging on individual cells (e.g., the hippocampus) are propitious for high-dimensional processing and learning of complex information items. We

show that a canonical simple neuronal model, the perceptron [150], in combination with a Hebbian-type of learning or spike timing dependent plasticity [151, 152] may provide answers to the above mentioned fundamental questions. In particular, starting from stochastic separation theorems [153] we demonstrate that individual neurons gathering multidimensional stimuli through a sufficiently large number of synaptic inputs can exhibit extreme selectivity either to individual information items or to groups of items. Moreover, neurons are capable of associating and learning uncorrelated information items. Thus, a large number of signaling routs simultaneously converging on a large number of single cells, as it is widely observed in laminar brain structures, translates into a natural environment for rapid formation and maintenance of extensive memories. This is vital for social life, and hence may constitute a significant evolutionary advantage, albeit, at the cost of high metabolic expenditure.

6.2. Fundamental problems of encoding memories

Different brain structures, such as, e.g., the hippocampus, have a pronounced laminar organization. For example the CA1 region of the hippocampus is constituted by a palisade of morphologically similar pyramidal cells oriented with their main axis in parallel and forming a monolayer (Fig. 6.1A). The major excitatory input to these neurons comes through Schaffer collaterals from the CA3 region [154, 155, 156], which is a hub routing information among many brain structures. Each CA3 pyramidal neuron sends an axon that bifurcates and leaves multiple collaterals in the CA1 with dominant parallel orientation (Fig. 6.1B). This topology allows multiple parallel axons conveying multidimensional "spatial" information from one area (CA3) simultaneously leave synaptic contacts on multiple neurons in another area (CA1). Thus, we have simultaneous convergence and divergence of the information content (Fig. 6.1B).

Experimental findings show that multiple CA1 pyramidal cells distributed in the rostro-caudal direction are activated near-synchronously by assemblies of simultaneously firing CA3 pyramidal cells [155, 157, 158]. Thus, an ensemble of single neurons in CA1 can receive simultaneously the same synaptic input (Fig. 6.1B). Since these neurons have different topology and functional connectivity [159], their response to the same input can be different. Moreover, experimental results *in-vivo* show that long term potentiation can significantly increase the spike transfer rate in the CA3-CA1 pathway [160]. This suggests that the efficiency of individual synaptic contacts can be increased selectively.

In this work we will follow conventional and rather general functional representation of signaling in the neuronal pathways. We assume that upon receiving an input, a neuron can either generate a response or remain silent. Forms of neuronal responses as well as the definitions of synaptic inputs vary from one model to another. However, here we adopt a rather general functional approach. Under a stimulus we understand a number of excitations simultaneously (or within a short time window) arriving to a neuron through several axones and thus transmitting some "spatially coded" information items [68]. If a neuron responds to a stimulus

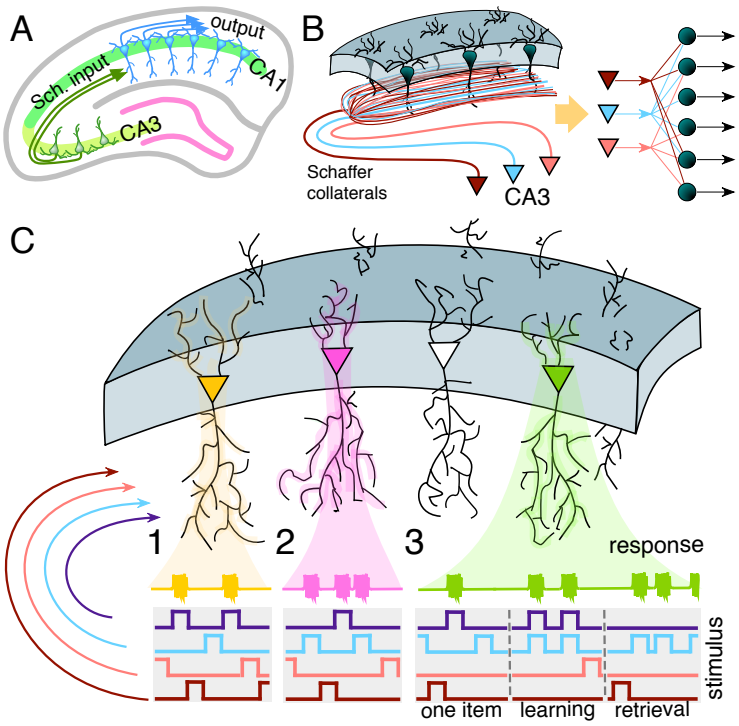

Figure 6.1: Encoding memories by single neurons in laminar structures. **A)** Laminar organization of the CA3 and CA1 areas in the hippocampus facilitates multiple parallel synaptic contacts between neurons in these areas by means of Schaffer collaterals. **B)** Axons from CA3 pyramidal neurons (different colors) bifurcate and pass through the CA1 area in parallel gives rise to the convergence-divergence of the information content (left panel). Multiple CA1 neurons receive multiple synaptic contacts. Such a connectivity structure (right panel). **C)** Schematic representation of three main encoding schemes. 1. Selectivity. A neuron (in yellow) receives inputs from multiple presynaptic cells that code different information items. It detects (responds) to only one stimulus (purple trace) while reject the others. 2. Clustering. Similar to 1, but now a neuron (in pink) detects a group of stimuli (purple and blue traces) and ignore the others. 3. Acquiring memories. A neuron (in green) learns dynamically a new memory item (blue trace) by associating it with know one (purple trace).

(e.g., generates output spikes or increases its firing rate), we then say that the neuron detects the information content of the given stimulus.

We now pose the following fundamental questions related to the information encoding and formation of memories by an ensemble of single neurons in laminated brain structures:

1. *Selectivity: Detection of one stimulus from a set* (Fig. 6.1C.1). Let us pick an arbitrary stimulus from a reasonably large set, such that a single neuron from a large neuronal ensemble detects this stimulus. Then what is the probability that this neuron will be stimulus-specific, i.e., it will reject all the other stimuli from the set?

2. *Clustering: Detection of a group of stimuli from a set* (Fig. 6.1C.2). Let us assume that within a set of stimuli we select a smaller subset, i.e., a group of stimuli. Then what is the probability that, in the neuronal ensemble, there exists a neuron such that it detects all stimuli from this subset but stays silent for all remaining stimuli in the set?

3. *Acquiring memories: Learning new stimulus by associating it with one already known* (Fig. 6.1C.3). Let us consider two different stimuli $\boldsymbol{s}_1$ and $\boldsymbol{s}_2$ such that at the beginning (for $t \in [0, t_0]$) they do not overlap in time and a neuron detects $\boldsymbol{s}_1$, but not $\boldsymbol{s}_2$. In the next interval $t \in (t_0, t_1]$ the stimuli start to overlap in time (i.e., they stimulate the neuron together). In the last time interval $t > t_1$ the neuron receives only stimulus $\boldsymbol{s}_2$. Then what is the probability that there is a time instant $t_2 \geq t_1$, such that the neuron will detect $\boldsymbol{s}_2$ alone?

These questions are at the core of a broad range of numerous puzzling phenomena reported in [145, 146, 147]. In what follows we will show that, remarkably, these non-trivial questions can be answered within a simple classical modeling framework whereby a neuron is represented by a mere perceptron equipped with a Hebbian-type of learning.

6.3. Formal statement of the problem

In what follows we will address the three fundamental questions formulated in Section 6.2. To this end we first will define the information content to be processed by neurons and then we will provide a mathematical model of the neuron equipped with synaptic plasticity.

Before going further let us first introduce suitable notations. Given two vectors $\boldsymbol{x}, \boldsymbol{y} \in \mathbb{R}^n$, their inner product is

$$\langle \boldsymbol{x}, \boldsymbol{y} \rangle = \sum_{i=1}^{n} x_i y_i.$$

We denote by $B_n(1) = \{\boldsymbol{x} \in \mathbb{R}^n | \ \ \|\boldsymbol{x}\| \leq 1\}$ a unit n-ball centered at the origin; $\mathcal{V}(\Xi)$ is the Lebesgue volume of $\Xi \subset \mathbb{R}^n$, and $|\mathcal{M}|$ is the cardinality of a set $\mathcal{M}$.

6.3.1. Information content and classes of stimuli

In what follows we assume that a neuron receives and processes a large but finite set of different stimuli codifying different information items:

$$\mathcal{S} = \{\boldsymbol{s}_i\}. \tag{6.1}$$

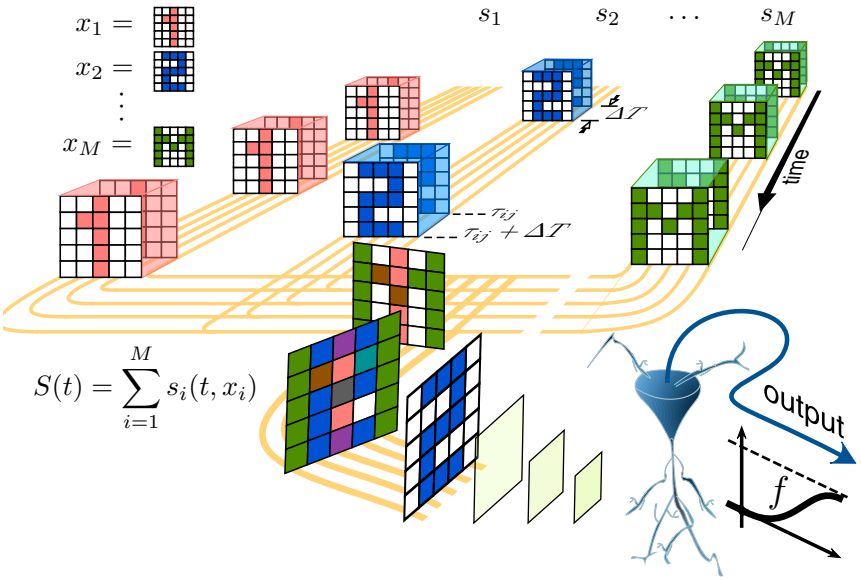

Figure 6.2: Codification of information in spatiotemporal stimuli received by a neuron. Each of M stimuli contains the "spatial" information, $\boldsymbol{x}_i \in \mathbb{R}^n$, (images from 1 to M) conducted through n axons (in yellow) and temporal part, $c(t - \tau_{ij})$, defining the times of arrival. A neuron (in blue) processes the stimuli and generates a response by using a transfer function f.

Figure 6.2 illustrates schematically the information flow. Each individual stimulus i is modeled by a vector-valued function $\boldsymbol{s} : \mathbb{R} \times \mathbb{R}^n \to \mathbb{R}^n$:

$$\boldsymbol{s}(t, \boldsymbol{x}_i) = \boldsymbol{x}_i \sum_j c(t - \tau_{ij}), \tag{6.2}$$

where $\boldsymbol{x}_i \in \mathbb{R}^n$ is the stimulus content codifying the information to be transmitted over n individual axons. For illustration purpose, as information items we will use some images $X_i \in \mathcal{M}_{l\times l}(\mathbb{R})$ (square matrices, Fig. 6.2). Then the dimension of each information item is $n = l^2$.

In Eq. (6.2) the function $c(\cdot)$ defines the stimulus context, i.e., the time windows when the stimulus arrives to the neuron. For the sake of simplicity we use a rectangular window:

$$c(t) = \begin{cases} 1 & \text{if } t \in [0, \Delta T] \\ 0 & \text{otherwise,} \end{cases} \tag{6.3}$$

where $\Delta T > 0$ is the window length. In the representation (6.2), (6.3) we assumed that the shape of all presynaptic activations does not change over time and is common for all stimuli. The time instants of the stimulus presentations, $\tau_{i,j}$, are ordered and satisfy:

$$\tau_{i,j+1} > \tau_{i,j} + \Delta T, \quad \forall j. \tag{6.4}$$

Different stimuli arrive to the neuron at different time instants and are added linearly on the neuronal membrane. Thus, in general the neuronal input can be written as:

$$\boldsymbol{S}(t) = \sum_{i,j} \boldsymbol{x}_i c(t - \tau_{i,j}). \tag{6.5}$$

In the next Section we will discuss different approaches to organizing memories in an ensemble of single neurons. For the sake of simplicity, we then assume that the information content of stimuli (6.1), i.e. vectors $\boldsymbol{x}_i$ are drawn i.i.d. from some distribution. Then for a given neuron some information will be relevant, while the other will not. For convenience, we thus partition the data sample into two sets:

$$\mathcal{M} = \{\boldsymbol{x}_1, \ldots, \boldsymbol{x}_M\}, \quad \mathcal{Y} = \{\boldsymbol{x}_{M+1}, \ldots, \boldsymbol{x}_{M+m}\}, \tag{6.6}$$

where M is large but finite and $m \geq 1$ is in general smaller than M. The set $\mathcal{M}$ contains a $background$ content for a given neuron, whereas the set $\mathcal{Y}$ models the informational content $relevant$ to the task at hand.

The sets $\mathcal{M}$ and $\mathcal{Y}$ give rise to the corresponding subsets of stimuli:

$$\begin{aligned} \mathcal{S}(\mathcal{M}) &= \{\boldsymbol{s}_i \in \mathcal{S} \mid \boldsymbol{s}_i(\cdot) = \boldsymbol{s}(\cdot, \boldsymbol{x}_i),\ \boldsymbol{x}_i \in \mathcal{M}\}, \\ \mathcal{S}(\mathcal{Y}) &= \{\boldsymbol{s}_i \in \mathcal{S} \mid \boldsymbol{s}_i(\cdot) = \boldsymbol{s}(\cdot, \boldsymbol{x}_i),\ \boldsymbol{x}_i \in \mathcal{Y}\}. \end{aligned} \tag{6.7}$$

6.3.2. Neuronal model

To stay within functional description of the information processing let us consider the most basic class of model neurons, a perceptron [150]. A single neuron receives a stimulus $\boldsymbol{s}(t, \boldsymbol{x})$ through n synaptic inputs (Fig. 6.2) and its membrane potential, $y(t) \in \mathbb{R}$, is given by

$$y(\boldsymbol{s}, \boldsymbol{w}) = \langle \boldsymbol{w}, \boldsymbol{s} \rangle, \tag{6.8}$$

where $\boldsymbol{w} \in \mathbb{R}^n$ is a vector of the synaptic weights. The neuron generates a response, v, according to:

$$v(\boldsymbol{s}, \boldsymbol{w}, \theta) = f(y(\boldsymbol{s}, \boldsymbol{w}) - \theta), \tag{6.9}$$

where $\theta \in \mathbb{R}$ is the firing threshold and $f : \mathbb{R} \to \mathbb{R}$ is the transfer function (Fig. 6.2, inset) satisfying: $f \in \mathcal{C}(\mathbb{R})$, f is locally Lipschitz, $f(u) = 0$ for $u \in (-\infty, 0]$, and $f(u) > 0$ for $u \in (0, \infty)$.

The model (6.8), (6.9) captures threshold nature of the neuronal activation but disregards the specific dynamics accounted in other more advanced models. Nevertheless, as we will show in Section 6.4, this phenomenological model is already sufficient to explain the fundamental properties of information processing, which we have discussed in Section 6.2.

6.3.3. Synaptic plasticity

In addition to the basic neuronal response mechanism, we also assume that the neuron can adapt to stimulation though a plasticity. In particular, we suppose that the synaptic weights, $\boldsymbol{w}$, do not stay constant over time but are adjusted in accordance with the Hebbian postulate.

The description adopted here relies on neuronal firing rates. Then the Hebbian rule implies that the dynamics of $\boldsymbol{w}$ should depend on the product of the input signal, $\boldsymbol{s}$, and the neuronal output, v. We thus arrive to a modified classical Oja rule [161]:

$$\dot{\boldsymbol{w}} = \alpha v y \left(\boldsymbol{s} - y\boldsymbol{w}\right), \tag{6.10}$$

where $\alpha > 0$ defines the relaxation time. The multiplicative term v in (6.10) accounts for STDP plasticity whereby the synaptic weights $\boldsymbol{w}$ are changed only when the stimulus evokes a non-zero neuronal response. Besides we note that in comparison to the classical Hebbian rule, the weights $\boldsymbol{w}$ are bounded in forward time (see below) and therefore conform with physiological plausibility.

The following results demonstrate that the provided neuronal model is well-posed.

Lemma 6.1

Consider (6.2), (6.9), and (6.10). Then:

1. Solutions $\boldsymbol{w}(\cdot, \boldsymbol{w}_0)$ of (6.10) are defined for all $t \geq t_0$ and are unique and bounded in forward time.

2. If, in addition, there exist numbers $L, \delta > 0$ such that the following property holds along the solutions of (6.10):

$$\int_t^{t+L} v(\tau) y^2(\tau)\, \mathrm{d}\tau > \delta, \quad \forall t \geq t_0, \tag{6.11}$$

then $\boldsymbol{x}/\|\boldsymbol{x}\|$ is an attractor, that is:

$$\lim_{t\to\infty} \boldsymbol{w}(t, \boldsymbol{w}_0) = \frac{\boldsymbol{x}}{\|\boldsymbol{x}\|}. \tag{6.12}$$

Proof. **1.** The right-hand side of (6.10) is continuous in $\boldsymbol{w}$ and piece-wise continuous in t with finite number of discontinuities of the first kind in any finite interval containing t_0, independently on the values of $\boldsymbol{w}$. Hence, in accordance with Peano Theorem, solutions of (6.10) are defined on some non-empty interval containing t_0. Let $\mathcal{T}$ be the maximal interval of this solution definition (to the right of t_0). There is a $t_1 > t_0$ such that $[t_0, t_1] \in \mathcal{T}$. Consider

$$V(\boldsymbol{w}) = 1 - \|\boldsymbol{w}\|^2.$$

In the interval $[t_0, t_1]$ we have:

$$\dot{V} = -2\alpha v y^2 V.$$

Given that $vy^2 \geq 0$, the above expression implies that

$$|1 - \|\boldsymbol{w}_0\|^2| \geq |1 - \|\boldsymbol{w}(t)\|^2| \geq \|\boldsymbol{w}(t)\|^2 - 1 \quad \Rightarrow \quad \|\boldsymbol{w}(t)\|^2 \leq 1 + |1 - \|\boldsymbol{w}_0\|^2|. \tag{6.13}$$

Hence $\boldsymbol{w}(\cdot, \boldsymbol{w}_0)$ is bounded on.

Given that the right-hand side of (6.10), as a function of $\boldsymbol{w}$, is continuous, the function f is continuous, and the function c in the definition of (6.2) is bounded, there is a constant $D > 0$ such that

$$\begin{aligned} &\|v(\boldsymbol{s}(t,\boldsymbol{x}), \boldsymbol{w}, t)\langle \boldsymbol{s}(t,\boldsymbol{x}), \boldsymbol{w}\rangle(\boldsymbol{s}(t,\boldsymbol{x}) - \langle \boldsymbol{s}(t,\boldsymbol{x}), \boldsymbol{w}\rangle \boldsymbol{w})\| < D \\ &\qquad \text{for all } \|\boldsymbol{w}\| \leq (|1 - \|\boldsymbol{w}_0\|^2| + 1)^{1/2}. \end{aligned}$$

This means that there exists a $\Delta > 0$ such that solutions $\boldsymbol{w}(\cdot, \boldsymbol{w}_0)$ are defined on $[t_0, t_1 + \Delta]$. And in fact, one can always extend the right boundary of this interval to the right by Δ-increments indefinitely. Hence $\mathcal{T} = [t_0, \infty)$, and solutions are defined for all $t \geq t_0$. Boundedness of solutions follows immediately from (6.13). Finally note that the right-hand side of (6.10) is locally Lipschitz in $\boldsymbol{w}$ implying that solution $\boldsymbol{w}(\cdot, \boldsymbol{w}_0)$ is unique.

2. For the sake of convenience, we denote

$$p(t) = v(\boldsymbol{s}(t,\boldsymbol{x}), \boldsymbol{w}(t, \boldsymbol{w}_0), \theta)\langle \boldsymbol{s}(t,\boldsymbol{x}), \boldsymbol{w}(t, \boldsymbol{w}_0)\rangle^2.$$

Notice that condition (6.11) assures that both $\boldsymbol{x} \neq 0$, $\boldsymbol{w}_0 \neq 0$. Moreover, since $V(\boldsymbol{w}(t, \boldsymbol{w}_0))$ is defined for all $t \geq t_0$, we can conclude that

$$V(t) = V_0 e^{-\alpha \int_{t_0}^{t} p(\tau) \mathrm{d}\tau} \leq V_0 e^{-\alpha\delta \left\lfloor \frac{t - t_0}{L} \right\rfloor}.$$

Hence

$$\lim_{t \to \infty} \|\boldsymbol{w}(t, \boldsymbol{w}_0)\| = 1. \tag{6.14}$$

Consider:

$$\boldsymbol{w}(t, \boldsymbol{w}_0) = e^{-\alpha \int_{t_0}^{t} p(\tau) \mathrm{d}\tau} \boldsymbol{w}_0 + \left[\int_{t_0}^{t} e^{-\alpha \int_{\tau}^{t} p(s) \mathrm{d}s} v(\tau) y(\tau) \sum_j c(\tau - \tau_j) \, \mathrm{d}\tau \right] \boldsymbol{x}$$

Observe that the first term decays exponentially to 0, whereas the second term is proportional to $\boldsymbol{x}$. This, combined with (6.14), automatically leads to (6.12) ■

6.4. Formation of memories in high-dimensions

In Section 6.2 we formulated three fundamental problems required for organization of memories in a laminar brain structure. Let us now show how they can be treated given that pyramidal neurons operate in high dimensions.

To formalize the analysis we require several definitions. Let $\mathcal{U}$ be a subset of the stimulus set $\mathcal{S}$. Then a neuron (6.9) parameterized by $(\boldsymbol{w}, \theta)$ partitions the set $\mathcal{U}$ into the following subsets:

$$\begin{aligned} \mathrm{Activated}(\mathcal{U}, (\boldsymbol{w}, \theta)) =& \{\boldsymbol{s}_i \in \mathcal{U} \mid \exists\ t > t_0 :\ v(\boldsymbol{s}_i(t), \boldsymbol{w}, \theta) \neq 0\} \\ \mathrm{Silent}(\mathcal{U}, (\boldsymbol{w}, \theta)) =& \{\boldsymbol{s}_i \in \mathcal{U} \mid v(\boldsymbol{s}_i(t), \boldsymbol{w}, \theta) = 0\ \forall\ t \geq t_0\}. \end{aligned} \tag{6.15}$$

6.4.1. Extreme selectivity of a single neuron to a single stimulus

In this section we aim at finding neurons with high specificity to the stimulus content, i.e., those that respond to a single stimulus while rejecting the others. Thus, the relevant set, $\mathcal{Y}$, has only one element $|\mathcal{Y}| = 1$. Let us also assume that the stimuli with different information content, $\boldsymbol{s}(\cdot, \boldsymbol{x}_i)$, do not overlap in time, i.e., we present them to a neuron one by one. We will further assume that the neuronal ensemble contains a large number of neurons with different parameters (Fig. 6.1).

Given a relevant information content, $\boldsymbol{x}_{M+1} \in \mathcal{Y}$, we may find a neuron in a big enough neuronal ensemble, such that it generates a non-zero response to the corresponding stimulus. In other words, $\boldsymbol{s}(\cdot, \boldsymbol{x}_{M+1}) \in \mathrm{Activated}(\mathcal{S}(\mathcal{Y}), (\boldsymbol{w}, \theta))$. Mathematically such a neuron can be selected in the following way.

Consider an orthonormal basis of $\mathbb{R}^n$ $\mathcal{B} = \{\boldsymbol{e}_i\}_{i=1}^n$, such that the first unit vector is directed along $\boldsymbol{x}_{M+1}$:

$$\boldsymbol{e}_1 = \frac{\boldsymbol{x}_{M+1}}{\|\boldsymbol{x}_{M+1}\|}. \tag{6.16}$$

Then the neuronal information space $\mathbb{R}^n = L\{\boldsymbol{e}_1\} \oplus L\{\boldsymbol{e}_2, \ldots, \boldsymbol{e}_n\}$. The neuron parameters, i.e., the coupling weights $\boldsymbol{w} = (w_1, \ldots, w_n)^T$ and the firing threshold θ, should satisfy the condition $w_1 > \theta / \|\boldsymbol{x}_{M+1}\|$ (Fig. 6.3, green area). This choice ensures that the neuronal output to this stimulus

$$v = f(w_1 \|\boldsymbol{x}_{M+1}\| - \theta) > 0,$$

for some $\tau_{M+1,k} > t_0$, and hence the neuron will generate a non-zero response to the stimulus.

According with the stimulus selectivity hypothesis (Sect. 6.2, Fig. 6.1C.1), such a neuron should be extremely selective.

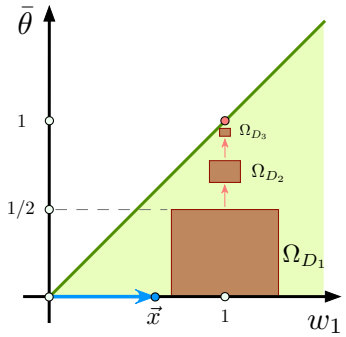

Figure 6.3: Selection of neuronal parameters $\bar{\theta} = \theta/\|\boldsymbol{x}_{M+1}\|$ and $\boldsymbol{w}$, such that the neuron responds to the relevant information $\boldsymbol{x}_{M+1}$. Any point within the green area ensures that the neuron will detect the stimulus $\boldsymbol{x}$. Here we use a basis $\mathcal{B}$ depending on the information item $\boldsymbol{x}_{M+1}$. Brown areas illustrates hypercylinders defined in Theorem 6.1 for $D_1 = 0{,}3$, $D_2 = 0.1$, $D_3 = 0{,}03$; and $\|\boldsymbol{x}\| = 0{,}6$.

Definition 6.1 (Neuronal Selectivity)**.** *We say that a neuron is selective to the information content iff it responds to the relevant stimulus from the set $\mathcal{S}(\mathcal{Y})$ and ignores all the others from the set $\mathcal{S}(\mathcal{M})$.*

As we will see below, different admissible pairs $(\boldsymbol{w}, \theta)$ (Fig. 6.3) produce different selectivity levels. The closer to the bisectris, the higher the selectivity. One can pick an arbitrary firing threshold $\theta \geq 0$ and select the synaptic efficiency:

$$\boldsymbol{w} = \frac{\theta + \epsilon}{\|\boldsymbol{x}_{M+1}\|}\boldsymbol{e}_1 + \sum_{i=2}^{n} w_i \boldsymbol{e}_i, \ \epsilon > 0, \ w_i \in \mathbb{R}. \tag{6.17}$$

Let us now get a deeper insight in the dynamics of $\boldsymbol{w}$. We assume that the stimuli $\boldsymbol{s}(\cdot, \boldsymbol{x}_i)$, $i = 1, \ldots, M$ do not produce neuronal response, i.e., $v(\boldsymbol{s}(t, \boldsymbol{x}_i)) = 0$. Then the dynamics of the coupling weights (6.10) is restricted to time intervals of the presence of the stimulus $\boldsymbol{s}(\cdot, \boldsymbol{x}_{M+1})$. Between these intervals $\boldsymbol{w}(t)$ stays constant. Thus, without lose of generality when considering the asymptotic behavior of $\boldsymbol{w}$ we can concatenate the stimulus intervals and assume that $\boldsymbol{s}(t) = \boldsymbol{x}_{M+1}$.

Now we note that in the basis (6.16), $L\{\boldsymbol{e}_1\}$ is an invariant manifold for (6.10) and by representing $\boldsymbol{w} = \sum_{i=1}^{n} w_i(t)\boldsymbol{e}_i$ we can rewrite the dynamics in the form:

$$\dot{w}_1 = \alpha\|\boldsymbol{x}_{M+1}\|^2 v(w_1) w_1 (1 - w_1^2), \tag{6.18}$$

$$\dot{w}_i = -\alpha\|\boldsymbol{x}_{M+1}\|^2 v(w_1) w_1^2 w_i, \quad i = 2, \ldots, n, \tag{6.19}$$

where $v(w_1) = f(w_1\|\boldsymbol{x}_{M+1}\| - \theta)$. Note that Eq. (6.18) is autonomous, while (6.19) depends on the solution $w_1(t)$. The coupling $\boldsymbol{w}$ shows some dynamics iff $v(w_1) > 0$ and hence $w_1 > \theta/\|\boldsymbol{x}_{M+1}\|$, which is equivalent to (6.17). Given that we have two cases (Fig. 6.4):

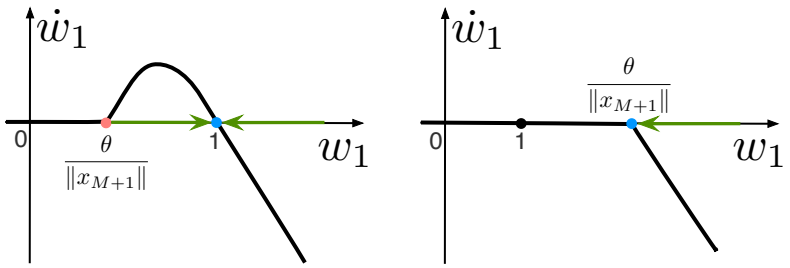

Figure 6.4: Sketch of the dynamics of $\boldsymbol{w}$ in the manifold $L\{\boldsymbol{e}_1\}$. Thick black curve shows the function corresponding to the r.h.s. of (6.18) for two cases: $\theta < \|x_{M+1}\|$ (left) and $\theta > \|x_{M+1}\|$ (right). Blue (red) dots correspond to stable (unstable) equilibria. Green arrows mark trajectories. In the first case (left) w_1 tends to 1, whereas in the second (right) it goes asymptotically to $\theta/\|x_{M+1}\|$.

A: If $\theta < \|\boldsymbol{x}_{M+1}\|$ then $w_1 \to 1$ and $w_i \to 0$, $i = 2, \ldots, n$ when $t \to \infty$. Thus,

$$\lim_{t\to\infty} \boldsymbol{w}(t) = \frac{\boldsymbol{x}_{M+1}}{\|\boldsymbol{x}_{M+1}\|} = \boldsymbol{e}_1. \tag{6.20}$$

This case is equivalent to the second statement of Lemma 6.1.

B: If $\theta \geq \|\boldsymbol{x}_{M+1}\|$ then $w_1 \to \theta/\|\boldsymbol{x}_{M+1}\|$ when $t \to \infty$. Given that f is Lipschitz we can conclude that $w_i \to w_i^*$, $i = 2, \ldots, n$, where the limit constants satisfy $0 \leq |w_i^*| < |w_i(0)|$. Thus,

$$\lim_{t\to\infty} \boldsymbol{w}(t) = \frac{\theta}{\|\boldsymbol{x}_{M+1}\|}\boldsymbol{e}_1 + \sum_{i=2}^{n} w_i^* \boldsymbol{e}_i. \tag{6.21}$$

Note that in this case condition (6.11) of Lemma 6.1 is not satisfied.

In summary, asymptotically the synaptic efficiency converges to:

$$\boldsymbol{w}_\infty = \begin{cases} \boldsymbol{e}_1 & \text{if } \theta < \|\boldsymbol{x}_{M+1}\| \\ \frac{\theta}{\|\boldsymbol{x}_{M+1}\|}\boldsymbol{e}_1 + \sum_{i=2}^{n} w_i^* \boldsymbol{e}_i & \text{if } \theta \geq \|\boldsymbol{x}_{M+1}\|, \end{cases} \tag{6.22}$$

where w_i^* are some constants depending on the initial conditions.

Figure 6.5 illustrates a typical simulation of the dynamics of three neurons with different pairs $(\boldsymbol{w}_i, \theta_i)$ under sequential stimulation by different information items. For illustration we selected several (30×38) color images (i.e., $\boldsymbol{x}_i \in \mathbb{R}^{3420}$). Then we arbitrary assigned the firing thresholds θ_i to the neurons and evaluated $\boldsymbol{w}_i$ by using (6.17) and the first three images as the relevant information items for the corresponding neurons. The neurons detect their own (relevant) stimuli, as expected. Moreover, they do not respond to the stimulation by other background information items. Thus, the neurons indeed exhibit high stimulus selectivity.

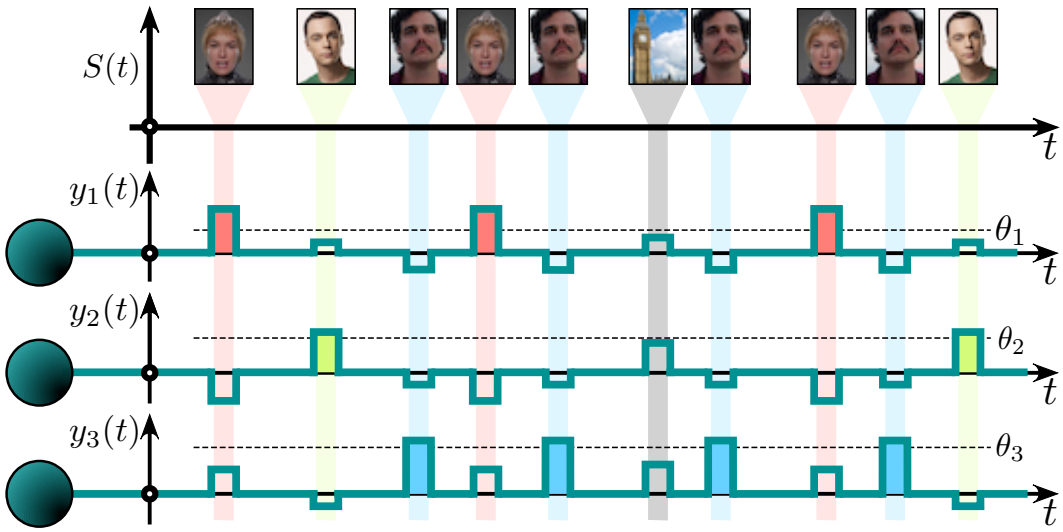

Figure 6.5: Example of selective neuronal responses to stimulation with different (30×38) images (only first few stimulus in the time line are shown). Each neuron responds to its own (relevant) stimulus only and rejects the others.

Theorem 6.1 provides theoretical justification of these observations. There and throughout the text, unless stated otherwise, we assume, for simplicity, that $\boldsymbol{x}_i$ are random vectors i.i.d in the unit ball $B_n(1)$ centered at the origin.

Theorem 6.1

Consider the sets of stimuli $\mathcal{S}(\mathcal{M})$ and $\mathcal{S}(\mathcal{Y})$ specified by (6.7). Let $(\boldsymbol{w}, \theta)$ be the neuron parameters such that

$$\boldsymbol{s}_{M+1} \in \text{Activated}(\mathcal{S}(\mathcal{Y}), (\boldsymbol{w}, \theta)) \text{ and } 0 < \frac{\theta}{\|\boldsymbol{w}\|} < 1.$$

Then:

1. The probability that the neuron is silent for all background stimuli $\boldsymbol{s}_i \in \mathcal{S}(\mathcal{M})$ is bounded from below by

$$P(\boldsymbol{s}_i \in \text{Silent}(\mathcal{S}(\mathcal{M}), (\boldsymbol{w}, \theta)) \; \forall \boldsymbol{s}_i \in \mathcal{S}(\mathcal{M}) | \; \boldsymbol{w}, \theta) \geq$$
$$\geq \left[1 - \frac{1}{2}\left(1 - \frac{\theta^2}{\|\boldsymbol{w}\|^2}\right)^{\frac{n}{2}}\right]^M. \tag{6.23}$$

2. There is a family of sets parametrized by D $(0 < D < \frac{1}{2})$,

$$\Omega_D = \Big\{(\boldsymbol{w},\theta)\big|\ \|\boldsymbol{w}-\boldsymbol{e}_1\| < D,\ \theta \in [\theta^* - 2D, \theta^* - D],\ 0 < \frac{\theta^* - D}{1-D} < 1\Big\},$$

where $\theta^* = \|\boldsymbol{x}_{M+1}\|$ and $\boldsymbol{e}_1 = \boldsymbol{x}_{M+1}/\|\boldsymbol{x}_{M+1}\|$, such that

$$\boldsymbol{s}_{M+1} \in \text{Activated}(\mathcal{Y},(\boldsymbol{w},\theta)) \text{ for all } (\boldsymbol{w},\theta) \in \Omega_D$$

and

$$\begin{aligned} P(\boldsymbol{s}_i \in \text{Silent}(\mathcal{S}(\mathcal{M}),(\boldsymbol{w},\theta))\ \forall \boldsymbol{s}_i \in \mathcal{S}(\mathcal{M})\big|\ (\boldsymbol{w},\theta) \in \Omega_D) \geq \\ \geq \max_{\varepsilon\in(0,1-2D)} (1-(1-\varepsilon)^n)\left[1-\frac{1}{2}\rho(\varepsilon,D)^{\frac{n}{2}}\right]^M, \end{aligned} \tag{6.24}$$

where

$$\rho(\varepsilon,D) = 1 - \left(\frac{1-\varepsilon-2D}{1+D}\right)^2.$$

Proof of Theorem 6.1. In two parts:

1. Let us first assume that $\|\boldsymbol{w}\| = 1$. Notice that the condition

$$\langle \boldsymbol{w}, \boldsymbol{x}_i\rangle \leq \theta \quad \forall \boldsymbol{x}_i \in \mathcal{M}, \tag{6.25}$$

assures that

$$\boldsymbol{s}_i \in \text{Silent}(\mathcal{S}(\mathcal{M}),(\boldsymbol{w},\theta)) \ \ \forall \boldsymbol{s}_i \in \mathcal{S}(\mathcal{M}),$$

i.e., the neuron is silent for all stimuli except $\boldsymbol{s}_{M+1}$ that does evoke a response by construction. Therefore, it is sufficient to estimate the probability that (6.25) holds.

Let $\mathcal{C}_n(\boldsymbol{w},\theta)$ be the spherical cap:

$$\mathcal{C}_n(\boldsymbol{w},\theta) = \{\boldsymbol{x} \in B_n(1) \mid \langle \boldsymbol{w},\boldsymbol{x}\rangle > \theta\}.$$

Then the ratio of volumes $\mathcal{V}(\mathcal{C}_n(\boldsymbol{w},\theta))/\mathcal{V}(B_n(1))$ is the probability that a random vector $\boldsymbol{x}_i \in \mathcal{C}_n(\boldsymbol{w},\theta)$. Observe that

$$\frac{\mathcal{V}(\mathcal{C}_n(\boldsymbol{w},\theta))}{\mathcal{V}(B_n(1))} \leq \frac{1}{2}(1-\theta^2)^{n/2}.$$

Thus, the probability that all $\boldsymbol{x}_i \in \mathcal{M}$ are outside the cap $\mathcal{C}_n(\boldsymbol{w},\theta)$ is bounded from below by

$$P \geq \left(1-\frac{1}{2}(1-\theta^2)^{n/2}\right)^M. \tag{6.26}$$

Let now $\|\boldsymbol{w}\| \neq 1$. Then the weights normalization $\boldsymbol{w} \mapsto \boldsymbol{w}/\|\boldsymbol{w}\|$ followed by the threshold scaling $\theta \mapsto \theta/\|\boldsymbol{w}\|$ generalize the estimate (6.26):

$$P(\boldsymbol{s}_i \in \mathrm{Silent}(\mathcal{S}(\mathcal{M}), (\boldsymbol{w}, \theta)) \text{ for all } \boldsymbol{s}_i \in \mathcal{S}(\mathcal{M}) | \, \boldsymbol{w}, \theta) \geq \left[1 - \frac{1}{2}\left(1 - \frac{\theta^2}{\|\boldsymbol{w}\|^2}\right)^{\frac{n}{2}}\right]^M.$$

This proves the first estimate (6.23).

2. Observe that $\boldsymbol{x}_{M+1} \neq 0$. Consider then the functional

$$\ell(\boldsymbol{x}) = \langle \boldsymbol{e}_1, \boldsymbol{x} \rangle - \theta^* + D.$$

It is clear that $\ell(\boldsymbol{x}_{M+1}) = D > 0$. Hence

$$\langle \boldsymbol{w}, \boldsymbol{x}_{M+1} \rangle - \theta = \ell(\boldsymbol{x}_{M+1}) + \langle \boldsymbol{w} - \boldsymbol{e}_1, \boldsymbol{x}_{M+1} \rangle + \theta^* - D - \theta > 0, \quad \forall (\boldsymbol{w}, \theta) \in \Omega_D.$$

This implies that $\boldsymbol{s}_{M+1} \in \mathrm{Activated}(\mathcal{Y}, (\boldsymbol{w}, \theta))$ $\forall (\boldsymbol{w}, \theta) \in \Omega_D$, i.e., the neuron detects the relevant information item given that its parameters are within Ω_D.

Using the definition of Ω_D we obtain the following inequality:

$$\frac{\theta}{\|\boldsymbol{w}\|} \geq \frac{\theta^* - 2D}{\|\boldsymbol{e}_1\| + D} = \frac{\|\boldsymbol{x}_{M+1}\| - 2D}{1 + D}, \quad \forall (\boldsymbol{w}, \theta) \in \Omega_D.$$

Now we notice that, with probability $p = 1 - (1 - \varepsilon)^n$, the norm $\|\boldsymbol{x}_{M+1}\| \geq 1 - \varepsilon$. Therefore, at least with probability p:

$$\frac{\theta}{\|\boldsymbol{w}\|} \geq \frac{1 - \varepsilon - 2D}{1 + D}.$$

Finally: 1) given $D > 0$, the value of ε can be chosen arbitrarily in $(0, 1 - 2D)$; 2) vectors $\boldsymbol{x}_i$ are drawn independently from the same distribution. Then estimate (6.24) immediately follows from (6.23) ■

Remark 6.1. *For a fixed D, the volume $\mathcal{V}(\Omega_D) > 0$. Thus, the estimate provided by Theorem 6.1 is robust to small perturbations of $(\boldsymbol{w}, \theta)$ and hence the neuronal characteristics can slightly fluctuate without affecting the neuronal functionality.*

Remark 6.2. *According to Theorem 6.1, the size of the stimuli set, $\mathcal{S}(\mathcal{M})$, for which the probability of neuronal selective response is guaranteed to exceed some fixed value $p_0 \in (0, 1)$ is exponential in dimension n. In order to see this, observe that (see e.g. (23) in [162])*

$$\left(1 - \frac{\theta^2}{\|\boldsymbol{w}\|^2}\right)^{\frac{n}{2}} < \exp\left(-\frac{n\theta^2}{2\|\boldsymbol{w}\|^2}\right).$$

Therefore, choosing M *so that* $\left(1-\frac{1}{2}\exp\left(-\frac{n\theta^2}{2\|\boldsymbol{w}\|^2}\right)\right)^M \geq p_0$ *or, equivalently, as*

$$M \leq \frac{\ln(p_0^{-1})}{-\ln\left(1-\frac{1}{2}\exp\left(-\frac{n\theta^2}{2\|\boldsymbol{w}\|^2}\right)\right)},$$

ensures that p_0 *is a lower bound for the expression in the right-hand side of (6.23). Recall that* $-\ln(1-x) < x/(1-x)$ *for all* $x \in (0,1)$ *([162], proof of Proposition 2). Hence*

$$M \leq \frac{\ln(p_0^{-1})(1-x)}{x} \Rightarrow M \leq \frac{\ln(p_0^{-1})}{-\ln(1-x)} \text{ for all } x \in (0,1).$$

Substituting $\frac{1}{2}\exp\left(-\frac{n\theta^2}{2\|\boldsymbol{w}\|^2}\right)$ *in place of* x *in this inequality results in*

$$\begin{aligned} &M \leq \exp\left(\frac{n\theta^2}{2\|\boldsymbol{w}\|^2}\right)\ln(p_0^{-1}) \Rightarrow \\ &\Rightarrow P(\boldsymbol{s}_i \in \mathrm{Silent}(\mathcal{S}(\mathcal{M}),(\boldsymbol{w},\theta))\ \forall \boldsymbol{s}_i \in \mathcal{S}(\mathcal{M})\big|\ \boldsymbol{w},\theta) \geq p_0, \end{aligned} \tag{6.27}$$

providing that relevant conditions of the theorem are met.

To illustrate the Theorem we generated 1000 information items $\{\boldsymbol{x}_i\}_{i=1}^{1000}$ by taking them equidistributed from: 1) a unit ball $B_n(1)$ (i.e. $\|\boldsymbol{x}_i\|_2 \leq 1$) and 2) a unit hypercube (i.e. $\|\boldsymbol{x}_i\|_\infty \leq 1$). Then we selected 2000 single neurons with fixed firing threshold $\theta_m = 0{,}5$. The coupling efficiency of each neuron $\{\boldsymbol{w}_m\}_{m=1}^{2000}$ was set according with (6.17) and $w_{mk} = 0$, $k = 2,\ldots,n$, $\epsilon = 0{,}05$. Once the neuronal ensemble and stimuli have been defined, we evaluated the output of each neuron and determined if it is selective(see Definition 6.1). The procedure was repeated for different values of n.

Figure 6.6A shows the empirical frequency of the selective neurons in an ensemble, for stimuli taken from: i) a unit ball (red), ii) a hypercube (blue), and iii) the estimate provided by Theorem 6.1 (dashed). In small dimensions ($n < 6$) neurons exhibit little selectivity, i.e., they confuse several stimuli and generate a nonspecific response. For higher dimensions the selectivity increases rapidly and around $n = 20$ it approaches $100\,\%$. Thus, an ensemble of "high dimensional" neurons is capable of detecting unequivocally information items from an exponentially in n large set of stimuli.

To formally evaluate the memory capacity of an ensemble of single neurons, we introduced the following notion:

Definition 6.2 (Memory Capacity)**.** *The memory capacity of a neuronal ensemble is the maximal number of information items (stimuli) that can be unequivocally detected by the ensemble with a given probability.*

For each dimension n we empirically searched for the maximal number of stimuli, such that the probability of detection of each of them by a the neuronal ensemble would be at least

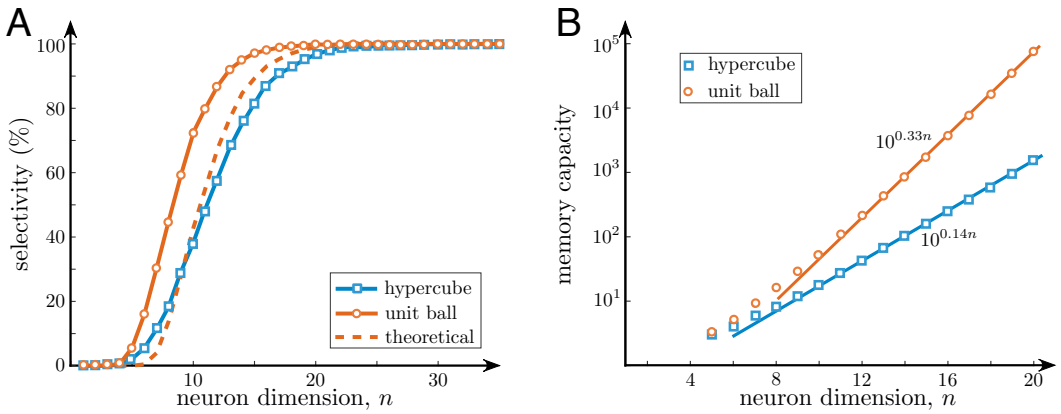

Figure 6.6: Extreme selectivity to stimuli and memory capacity of single neurons. A) Stimulus selectivity vs the neuron dimension. B) Memory capacity of a neuronal ensemble vs the neuron dimension.

p. Figure 6.6B shows the memory capacity from two distributions: in a unit ball and in a hypercube. The memory capacity grows exponentially (cf. (6.27)) with the neuron dimension in both cases. Such a fast growth can easily cover quite exigent memory necessities.

Theorem 6.1 also provides a general way to find neurons responsive to a given stimulus and also selective (i.e., ignoring) to background stimuli with some probability. Figure 6.3 shows three projections of the hypercylinders (in brown) ensuring the stimulus detection and selectivity. The smaller is the cylinder, the higher is the selectivity.

6.4.2. Selectivity of a single neuron to multiple stimuli

To organize memories, the ability to associate different information items into groups (Fig. 6.1C2) is essential. Let us now consider the task of how a neuron can separate a group of items, e.g. randomly and independently chosen m elements, from another random set whose size M is large enough to be of interest, i.e. $M \gg n$. In particular, the neuron should detect all items from the relevant set $\mathcal{Y}$, whilst rejecting all the others from the background set $\mathcal{M}$.

To assess neuronal selectivity to multiple stimuli, we consider the set $\mathcal{Y}$ containing several random vectors: $\mathcal{Y} = \{\boldsymbol{x}_{M+1}, \ldots, \boldsymbol{x}_{M+m}\}$ with $m > 1$. As in Section 6.4.1, here we assume that all stimuli do not overlap in time and arrive to the neuron separately. We also suppose that the vectors $\{\boldsymbol{x}_i\}_{i=1}^{M+m}$ are drawn i.i.d. from $B_n(1)$. Then the question of interest is: Can we find a neuron [i.e., parameters $(\boldsymbol{w}, \theta)$], such that it would generate a non-zero response to all $\boldsymbol{s}_i \in \mathcal{S}(\mathcal{Y})$ and, with high enough probability, would be silent to all $\boldsymbol{s}_i \in \mathcal{S}(\mathcal{M})$?

Theorem 6.2 as well as the numerical analysis provided assure that this is indeed possible, provided that the neuronal dimensionality, n, is large enough. Moreover, the theorem states that the separation can be achieved by neurons whose synaptic weights vectors, $\boldsymbol{w}$, are aligned closely to the mean vector for the stimulus set $\mathcal{Y}$:

$$\bar{\boldsymbol{x}} = \frac{1}{m}\sum_{i=1}^{m} \boldsymbol{x}_{M+i}. \tag{6.28}$$

This vector points to the center of the group to be separated from the remaining background vectors. In low dimensions, e.g., $n = 2$, such a choice appears to be extremely unlikely to succeed if at all possible. However, as we will see later, high dimensional neurons can accomplish this task, with probability close to one.

Theorem 6.2

Consider the sets of stimuli $\mathcal{S}(\mathcal{M})$ and $\mathcal{S}(\mathcal{Y})$ specified by (6.7) and let $D > 0$, $\varepsilon, \delta \in (0, 1)$ be chosen such that

$$\theta^* = \frac{(1-\varepsilon)^3 - \delta(m-1)}{\sqrt{m(1-\varepsilon)[1-\varepsilon+\delta(m-1)]}} > D. \tag{6.29}$$

Consider the set:

$$\Omega_D = \Big\{(\boldsymbol{w}, \theta) \big|\ \|\boldsymbol{w} - \boldsymbol{w}^*\| < D,\ \theta \in (0, \theta^* - D],\ 0 < \frac{\theta^* - D}{1 - D} < 1\Big\},$$

where $\boldsymbol{w}^* = \bar{\boldsymbol{x}}/\|\bar{\boldsymbol{x}}\|$. Then

$$\begin{aligned} &P\Big([\boldsymbol{s}_i \in \text{Activated}(\mathcal{S}(\mathcal{Y}), \boldsymbol{w}, \theta)\ \forall\ \boldsymbol{s}_i \in \mathcal{S}(\mathcal{Y})]\ \& \\ &\quad [\boldsymbol{s}_i \in \text{Silent}(\mathcal{S}(\mathcal{M}), \boldsymbol{w}, \theta)\ \forall\ \boldsymbol{s}_i \in \mathcal{S}(\mathcal{M})]\Big|(\boldsymbol{w}, \theta) \in \Omega_D\Big) \geq p(\varepsilon, \delta, D, m), \end{aligned} \tag{6.30}$$

where

$$\begin{aligned} p(\varepsilon, \delta, D, m) =& (1 - (1-\varepsilon)^n)^m \prod_{d=1}^{m-1} \left(1 - d\left(1-\delta^2\right)^{\frac{n}{2}}\right)\left[1 - \frac{1}{2}\Delta^{\frac{n}{2}}\right]^M, \\ \Delta =& 1 - \frac{\theta^2}{(1+D)^2}. \end{aligned}$$

The proof of the Theorem is essentially contained in the two following Lemmas (cf. [162]).

Lemma 6.2

Let $\mathcal{Y} = \{\boldsymbol{x}_1, \boldsymbol{x}_2, \ldots, \boldsymbol{x}_k\}$ be a set of k i.i.d. random vectors from the equidistribution in the unit ball $B_n(1)$. Let $\delta, r \in (0,1)$, and suppose that $\|\boldsymbol{x}_i\| \geq r$, for all $i \in \{1, \ldots, k\}$.

Then the probability that the elements of $\mathcal{Y}$ are pair-wise δ/r-orthogonal, that is

$$|\cos(\angle(\boldsymbol{x}_i, \boldsymbol{x}_j))| \leq \frac{\delta}{r} \text{ for all } i \neq j \quad i, j \in \{1, \ldots, k\},$$

is bonded from below as

$$\mathcal{P}\left(|\cos(\angle(\boldsymbol{x}_i, \boldsymbol{x}_j))| \leq \frac{\delta}{r} \ \forall\ i, j \in \{1, \ldots, k\},\ i \neq j \ \mid \|\boldsymbol{x}_i\| \geq r,\ 1 \leq i \leq k\right) \geq \prod_{d=1}^{m-1} \left(1 - d\left(1 - \delta^2\right)^{\frac{n}{2}}\right).$$

Proof. Let $\boldsymbol{x}_i$, $i = 1, \ldots, k$ be random vectors satisfying conditions of the lemma. Let $E_\delta(\boldsymbol{x}_i)$ be the delta-thickening of the largest equator of $B_n(1)$ that is orthogonal to $\boldsymbol{x}_i$. There is only one such equator, and it is uniquely determined by $\boldsymbol{x}_i$. Consider the following probabilities:

$$\begin{aligned}
&P(\boldsymbol{x}_2 \in\ E_\delta(\boldsymbol{x}_1))\\
&P([\boldsymbol{x}_3 \in\ E_\delta(\boldsymbol{x}_2)]\&[\boldsymbol{x}_3 \in\ E_\delta(\boldsymbol{x}_1)])\\
&P([\boldsymbol{x}_4 \in\ E_\delta(\boldsymbol{x}_3)]\&[\boldsymbol{x}_4 \in\ E_\delta(\boldsymbol{x}_2)]\&[\boldsymbol{x}_4 \in\ E_\delta(\boldsymbol{x}_1)])\\
&\ldots\\
&P([\boldsymbol{x}_k \in\ E_\delta(\boldsymbol{x}_{k-1})]\&\cdots\&[\boldsymbol{x}_k \in\ E_\delta(\boldsymbol{x}_1)]).
\end{aligned}$$

Recall that, for any random events $A_1, \ldots, A_k$, the probability

$$P(A_1 \& A_2 \& \cdots \& A_k) \geq 1 - \sum_{i=1}^{k} (1 - P(A_i)).$$

Pick $\boldsymbol{x}_i, \boldsymbol{x}_j \in \mathcal{Y}$, $i \neq j$. The probability that $\boldsymbol{x}_i \in E_\delta(\boldsymbol{x}_j)$ is bounded from below by $1 - (1 - \delta^2)^{\frac{n}{2}}$ (cf. [162], Proposition 3; see also Figure 1 in [162] for illustration). Then

$$\begin{aligned}
&P(\boldsymbol{x}_2 \in\ E_\delta(\boldsymbol{x}_1)) \geq 1 - \left(1 - \delta^2\right)^{\frac{n}{2}}\\
&P([\boldsymbol{x}_3 \in\ E_\delta(\boldsymbol{x}_2)]\&[\boldsymbol{x}_3 \in\ E_\delta(\boldsymbol{x}_1)]) \geq 1 - 2\left(1 - \delta^2\right)^{\frac{n}{2}}\\
&P([\boldsymbol{x}_4 \in\ E_\delta(\boldsymbol{x}_3)]\&[\boldsymbol{x}_4 \in\ E_\delta(\boldsymbol{x}_2)]\&[\boldsymbol{x}_4 \in\ E_\delta(\boldsymbol{x}_1)]) \geq 1 - 3\left(1 - \delta^2\right)^{\frac{n}{2}} \qquad (6.31)\\
&\ldots\\
&P([\boldsymbol{x}_k \in\ E_\delta(\boldsymbol{x}_{k-1})]\&\cdots\&[\boldsymbol{x}_k \in\ E_\delta(\boldsymbol{x}_1)]) \geq 1 - (k-1)\left(1 - \delta^2\right)^{\frac{n}{2}}.
\end{aligned}$$

The fact that $\boldsymbol{x}_i \in E_\delta(\boldsymbol{x}_j)$ combined with the condition that $\|\boldsymbol{x}_i\| \geq r$, $\boldsymbol{x}_j \geq r$ imply:

$$|\cos(\angle(\boldsymbol{x}_i, \boldsymbol{x}_j))| \leq \frac{\delta}{r}.$$

Finally, given that $\boldsymbol{x}_1, \ldots, \boldsymbol{x}_k$ are drawn independently, the probability that all vectors in $\mathcal{Y}$ are pair-wise orthogonal is the product of all probabilities in the left-hand side of (6.31). Thus the statement follows ■

Lemma 6.3

Let $\mathcal{Y} = \{\boldsymbol{x}_1, \ldots, \boldsymbol{x}_m\}$ be a finite set from $B_n(1)$. Let $\|\boldsymbol{x}_i\| \geq 1 - \varepsilon$, $\varepsilon \in (0, 1)$ for all $\boldsymbol{x}_i \in \mathcal{Y}$, and $\beta_1, \beta_2 \in \mathbb{R}$ be such that the following condition holds:

$$\beta_2(m-1) \leq \sum_{j \in \{1,\ldots,m\},\ j \neq i} \langle \boldsymbol{x}_i, \boldsymbol{x}_j \rangle \leq \beta_1(m-1) \text{ for all } i = 1, \ldots, m. \tag{6.32}$$

Consider the linear functional

$$\ell(\boldsymbol{x}) = \left\langle \frac{\bar{\boldsymbol{y}}}{\|\bar{\boldsymbol{y}}\|}, \boldsymbol{x} \right\rangle - \frac{1}{\sqrt{m}} \left(\frac{(1-\varepsilon)^2 + \beta_2(m-1)}{\sqrt{1 + (m-1)\beta_1}} \right),\ \bar{\boldsymbol{y}} = \frac{1}{m} \sum_{i=1}^{m} \boldsymbol{x}_i,$$

and suppose that parameters β_1, β_2 satisfy:

$$(1-\varepsilon)^2 + \beta_2(m-1) > 0,\ 1 + (m-1)\beta_1 > 0.$$

Then

$$\ell(\boldsymbol{x}_i) \geq 0 \text{ for all } \boldsymbol{x}_i \in \mathcal{Y}. \tag{6.33}$$

Proof. Consider the set $\mathcal{Y}$. According to the lemma assumptions, $\|\boldsymbol{x}_i\| \geq 1 - \varepsilon$ for some given $\varepsilon \in (0, 1)$ and all $i = 1, \ldots, m$. Consider now the mean vector $\bar{\boldsymbol{y}}$

$$\bar{\boldsymbol{y}} = \frac{1}{m} \sum_{i=1}^{m} \boldsymbol{x}_i,$$

and evaluate the following inner products

$$\left\langle \frac{\bar{\boldsymbol{y}}}{\|\bar{\boldsymbol{y}}\|}, \boldsymbol{x}_i \right\rangle = \frac{1}{m\|\bar{\boldsymbol{y}}\|} \left(\|\boldsymbol{x}_i\|^2 + \sum_{j \in \{1,\ldots,m\},\ j \neq i} \langle \boldsymbol{x}_i, \boldsymbol{x}_j \rangle \right),\ i = 1, \ldots, m.$$

According to assumption (6.32), the following holds

$$\left\langle \frac{\bar{\boldsymbol{y}}}{\|\bar{\boldsymbol{y}}\|}, \boldsymbol{x}_i \right\rangle \geq \frac{1}{m\|\bar{\boldsymbol{y}}\|} \left((1-\varepsilon)^2 + \beta_2(m-1) \right),$$

and, respectively,

$$\frac{1}{m}\left(1 + (m-1)\beta_1\right) \geq \langle \bar{\boldsymbol{y}}, \bar{\boldsymbol{y}} \rangle = \|\bar{\boldsymbol{y}}\|^2 \geq \frac{1}{m}\left((1-\varepsilon)^2 + \beta_2(m-1) \right)$$

Let $(1-\varepsilon)^2 + \beta_2(m-1) > 0$ and $1 + \beta_1(m-1) > 0$. It is clear that for the the functional ℓ, as defined by (6.33), the following holds for all $i = 1, \ldots, m$: $\ell(\boldsymbol{x}_i) \geq 0$ ■

Proof of Theorem 6.2. Consider the set $\mathcal{Y}$. With probability $(1-(1-\varepsilon)^n)^m$, all elements $\boldsymbol{x}_i \in \mathcal{Y}$ satisfy the condition $\|\boldsymbol{x}_i\| \geq 1-\varepsilon$. Hence, using Lemma 6.2 we have that the following inequality

$$|\langle \boldsymbol{x}_i, \boldsymbol{x}_j \rangle| \leq \frac{\delta}{1-\varepsilon}, \quad \forall \boldsymbol{x}_i, \boldsymbol{x}_j \in \mathcal{Y},\ i \neq j$$

holds with probability

$$p_0 \geq (1-(1-\varepsilon)^n)^m \prod_{d=1}^{m-1} \left(1 - d(1-\delta^2)^{\frac{n}{2}}\right).$$

This implies that, with probability p_0, the following conditions are met

$$\|\boldsymbol{x}_i\| \geq 1-\varepsilon, \quad -\frac{(m-1)\delta}{1-\varepsilon} \leq \sum_{j=1,\ j\neq i}^{m} \langle \boldsymbol{x}_i, \boldsymbol{x}_j \rangle \leq \frac{(m-1)\delta}{1-\varepsilon}, \quad \forall\ \boldsymbol{x}_i \in \mathcal{Y}.$$

Consider the functional $\ell(\boldsymbol{x}) = \langle \boldsymbol{w}^*, \boldsymbol{x} \rangle - \theta^* + D$. Denoting $\beta_1 = \delta/(1-\varepsilon)$, $\beta_2 = -\delta/(1-\varepsilon)$, and invoking Lemma 6.3, we can conclude that, with probability p_0,

$$\ell(\boldsymbol{x}) \geq D, \quad \forall \boldsymbol{x} \in \mathcal{Y}.$$

In fact, following the argument from the proof of Theorem 6.1, we can conclude that

$$\ell_0(\boldsymbol{x}) = \langle \boldsymbol{w}, \boldsymbol{x} \rangle - \theta = \ell(\boldsymbol{x}) + \langle \boldsymbol{w} - \boldsymbol{w}^*, \boldsymbol{x} \rangle - \theta + (\theta^* - D) > 0\ \forall\ (\boldsymbol{w}, \theta) \in \Omega_D,\ \boldsymbol{x} \in \mathcal{Y}.$$

Thus the probability that $\ell_0(\boldsymbol{x}) > 0$ for all $\boldsymbol{x} \in \mathcal{Y}$ and that $\ell_0(\boldsymbol{x}) \leq 0$ for all $\boldsymbol{x} \in \mathcal{M}$ is bounded from below by

$$(1-(1-\varepsilon)^n)^m \prod_{d=1}^{m-1} \left(1 - d(1-\delta^2)^{\frac{n}{2}}\right) \left(1 - \frac{1}{2}\left(1 - \frac{\theta^2}{\|\boldsymbol{w}\|^2}\right)^{\frac{n}{2}}\right)^M.$$

Noticing that $\|\boldsymbol{w}\| \leq 1 + D$, we can conclude that (6.30) holds ■

The Theorem admits a simple corollary.

Corollary 6.1

Suppose that conditions of Theorem 6.2 hold. Let, in addition, $\theta^* > 2D$. Consider the set

$$\Omega_D^* = \Big\{(\boldsymbol{w},\theta)\big|\ \|\boldsymbol{w}-\boldsymbol{w}^*\| < D,\ \theta \in [\theta^*-2D, \theta^*-D],\ 0 < \frac{\theta^*-D}{1-D} < 1\Big\},$$

where $\boldsymbol{w}^* = \bar{\boldsymbol{x}}/\|\bar{\boldsymbol{x}}\|$. Then

$$\begin{aligned} &P\Big([\boldsymbol{s}_i \in \mathrm{Activated}(\mathcal{S}(\mathcal{Y}), \boldsymbol{w}, \theta)\ \forall\ \boldsymbol{s}_i \in \mathcal{S}(\mathcal{Y})]\ \& \\ &[\boldsymbol{s}_i \in \mathrm{Silent}(\mathcal{S}(\mathcal{M}), \boldsymbol{w}, \theta)\ \forall\ \boldsymbol{s}_i \in \mathcal{S}(\mathcal{M})]\Big|(\boldsymbol{w},\theta) \in \Omega_D^*\Big) \geq \\ &\geq (1-(1-\varepsilon)^n)^m \prod_{d=1}^{m-1}\left(1-d\left(1-\delta^2\right)^{\frac{n}{2}}\right)\left[1-\frac{1}{2}\Delta^{\frac{n}{2}}\right]^M, \end{aligned} \tag{6.34}$$

where

$$\Delta = 1-\left(\frac{\theta^*-2D}{1+D}\right)^2.$$

Proof. The proof of this corollary follows immediately from Theorem 6.2 and the fact that $\theta > \theta^* - 2D$ ■

Remark 6.3. *Estimate (6.30) provided by Theorem 6.2 holds for all admissible values of ε, δ specified by (6.29). These include maximizers of $p(\varepsilon, \delta, D, m)$, which can be used as the lower-bound "optimistic" estimates of the neuron performance.*

Remark 6.4. *The term θ^* in Theorem 6.2 is an upper bound for the firing threshold θ. The larger is the value of θ, the higher is the neuronal selectivity to multiple stimuli. The value of θ^*, however, decays with the number of stimuli m.*

The extent to which the decay mentioned in Remark 6.4 affects the neuron's abilities to separate multiple stimuli from the rest depends largely on the neuron dimensionality, n, and hence that of the information content $\boldsymbol{x}_i$. Note also that the probability of neuronal selective response to multiple stimuli, as provided by Theorem 6.2, can be much larger if the informational content vectors, $\boldsymbol{x}_i$, of the stimuli set $\mathcal{S}(\mathcal{Y})$ are spatially close or positively correlated [163] (see also Lemma 6.3).

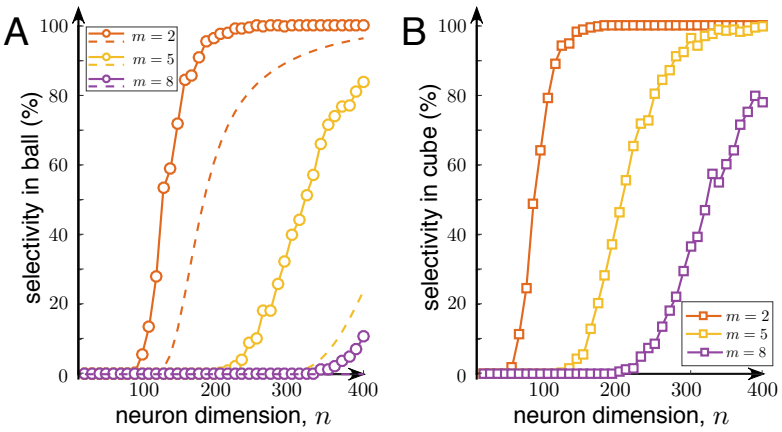

Figure 6.7: Selectivity of a single neuron to multiple stimuli. The neuronal selectivity for stimuli of which the informational content vectors $\boldsymbol{x}_i$ are chosen randomly **A)** from a unit ball, and **B)** from a hypercube, approaches $100\,\%$ if the dimension grows. In (A) dashed curves correspond to estimates provided by Theorem 6.2. Parameter values: $\epsilon = 0{,}01$, $D = 0{,}001$, $\delta = (1-\epsilon)/2(m-1), \theta = \theta^* - D$.

Remark 6.5. *Similarly to Remark 6.2, the size of the stimuli set $\mathcal{S}(\mathcal{M})$ for which selective response is ensured, with some fixed probability, grows exponentially with dimension n. In order to see this, observe that*

$$(1-(1-\varepsilon)^n)^m \prod_{d=1}^{m-1}\left(1-d\left(1-\delta^2\right)^{\frac{n}{2}}\right)\left[1-\frac{1}{2}\Delta^{\frac{n}{2}}\right]^M \geq$$
$$\geq (1-(1-\varepsilon)^n)^m \left(1-m\exp\left(-\frac{\delta^2 n}{2}\right)\right)^m \left(1-\exp\left(-\frac{n\Delta^2}{2}\right)\right)^M.$$

Hence choosing $M \leq \exp\left(\frac{n\Delta^2}{2}\right)\ln(p_0^{-1})$ implies, in accordance with (6.30), that

$$P\Big([\boldsymbol{s}_i \in \text{Activated}(\mathcal{S}(\mathcal{Y}), \boldsymbol{w}, \theta)\ \forall\ \boldsymbol{s}_i \in \mathcal{S}(\mathcal{Y})]\ \&$$
$$\&\ [\boldsymbol{s}_i \in \text{Silent}(\mathcal{S}(\mathcal{M}), \boldsymbol{w}, \theta)\ \forall\ \boldsymbol{s}_i \in \mathcal{S}(\mathcal{M})]\Big|(\boldsymbol{w}, \theta) \in \Omega_D\Big) \geq$$
$$\geq p_0\left(1-m\exp\left(-\frac{\delta^2 n}{2}\right)\right)^m (1-(1-\varepsilon)^n)^m.$$

To better illustrate Theorem 6.2 we conducted several numerical experiments. We used a set of $M = 10^3$ background information items $\mathcal{M}$ and a set of relevant vectors, $\mathcal{Y}$, consisting of $m = \{2, 5, 8\}$. All items (i.e., vectors $\boldsymbol{x}_i$, $i = 1, \ldots, M+m$) were randomly chosen. First, we used a unit ball with equidistribution and selected the neuronal parameters in accordance with Theorem 6.2. Figure 6.7A illustrates the results.

Similarly to the case of neuronal selectivity to a single item (Fig. 6.6A), we observe a steep growth of the selectivity index with dimensionality of neuronal synaptic weights vectors. The sharp increase occurs, however, at significantly higher dimensions (around $n = 120$ for $m = 2$). The number of random and uncorrelated stimuli, to which a neuron is capable to respond selectively is fundamentally linked to the neuron dimensionality. For example, the probability that the neurons are selective to $m = 5$ random stimuli becomes sufficiently large only at $n > 400$. This contrasts sharply with the case when $m = 2$.

Our numerical experiments also show that the firing threshold specified in Theorem 6.2 for arbitrarily chosen fixed values of δ, ε is not optimal in the sense of providing the best possible probability estimates. Playing with θ one can observe that the values of n at which neuronal selectivity to multiple stimuli starts to emerge are in fact significantly lower than those predicted by (6.34). This is not surprising. First, since estimate (6.34) holds for all admissible values of δ, ε, it should hold for the maximizer of $p(\varepsilon, \delta, D, m)$. Second, the estimate is conservative in the sense that it is based on conservative estimates of the volume of spherical cups $\mathcal{C}_n$ (see e.g. proof of Theorem 6.1). Deriving more accurate numerical expressions for the latter is of course possible, although at the expense of simplicity. Qualitatively, however, the results will not change.

To demonstrate that dependence of the selectivity index on the firing threshold is likely to hold qualitatively for much broader class of distributions from which the sets $\mathcal{M}$, $\mathcal{Y}$ are drawn, we repeated the simulation for a distribution in the unit n-cube centered at the origin. In this case, Theorem 6.2 does not formally apply. Yet, as our experiments showed, an equivalent statement can still be produced (cf. [153]). We selected the firing threshold $\theta = 0{,}5\|\bar{x}\|$ and repeated the simulation for the equidistribution in the unit n-cube. The results are shown in Figure 6.7B. The neuron's performance in the cube is markedly better than that of in $B_n(1)$. Interestingly, this is somewhat contrary to expectations that might have been induced by our earlier experiments (shown in Figure 6.6) in which neuronal selectivity of a single neuron to a single stimulus was more pronounced for $B_n(1)$.

Overall, the results suggest that single neurons can indeed separate random uncorrelated information items from a large set of background items with probability close to one. This gives rise to a possibility for a neuron to respond selectively to various arbitrary uncorrelated information items simultaneously. The latter property provides a natural mechanism for accurate and precise grouping of stimuli by a single neuron.

6.4.3. Dynamic memory: Learning new information items by association

In the previous sections we dealt with a quasistatic model of neuronal functions. We assumed that the relevant information items were sparse in time and hence the synaptic efficiency did not change much. Such a functionality can be related to "static" memory. Let us now proceed to study the dynamic memory.

In this section we explicitly model the dynamics of synaptic efficiency, $\boldsymbol{w}$, over time in accordance with (6.10), a Hebbian-type model of synaptic plasticity. As before, we will deal with two sets of stimuli, the relevant one $\mathcal{S}(\mathcal{Y})$ and the background one $\mathcal{S}(\mathcal{M})$. We will divide the time interval into two epochs: i) Learning phase and ii) Retrieval phase. Within the learning phase all stimuli from the set $\mathcal{S}(\mathcal{Y})$ arrive completely synchronized, i.e.,:

$$\tau_{M+1,j} = \tau_{M+2,j} = \cdots = \tau_{M+m,j}, \quad \forall\, j. \tag{6.35}$$

Such a synchronization is assumed to be a mechanism for associating or grouping different uncorrelated information items for the purposes of memorizing them at a later stage.

The dynamics of the synaptic weights for $t \geq t_0$ follows Eq. (6.10) with the input signal given by:

$$\bar{\boldsymbol{s}}(t) = \sum_{i=1}^{m} \boldsymbol{s}_{M+i}(t), \quad \boldsymbol{w}(t_0) = \boldsymbol{w}_0. \tag{6.36}$$

Let the values of $\boldsymbol{w}_0 \in \mathbb{R}^n$ and the neural firing threshold, θ, satisfy the following condition:

$$\begin{aligned} &\exists\ \boldsymbol{s}_k \in \mathcal{S}(\mathcal{Y}) \ \text{ such that } \ \boldsymbol{s}_k \in \text{Activated}(\mathcal{S}(\mathcal{Y}), \boldsymbol{w}_0, \theta) \\ &\boldsymbol{s}_i \in \text{Silent}(\mathcal{S}(\mathcal{Y}), \boldsymbol{w}_0, \theta) \text{ for all } \boldsymbol{s}_i \in \mathcal{S}(\mathcal{Y}) \setminus \{\boldsymbol{s}_k\}. \end{aligned} \tag{6.37}$$

Thus, at the beginning there is one information item "known" to the neuron, whereas the others relevant items are "new".

As we have already shown (see, e.g., Theorem 6.1), if n is large enough then there exist domains of such parametrizations, $(\boldsymbol{w}_0, \theta)$, with probability close to one (Fig. 6.3). Then the question is: What is the probability that, during the learning phase the synaptic weights evolve in time in such a way that the neuron becomes responsive to all $\boldsymbol{s}_i \in \mathcal{S}(\mathcal{Y})$ whilst remaining silent to all $\boldsymbol{s}_i \in \mathcal{S}(\mathcal{M})$? In this scenario the neuron learns new items and can recognize them in the retrieval phase. The answer to this question is provided by the following theorem.

Theorem 6.3

Consider the sets of stimuli $\mathcal{S}(\mathcal{M})$ and $\mathcal{S}(\mathcal{Y})$ specified by (6.7). Let (6.35) hold, the dynamics of neuronal synaptic weights satisfy (6.10), (6.36), and $(\boldsymbol{w}_0, \theta)$ be chosen such that condition (6.37) is satisfied. Pick $\varepsilon, \delta \in (0, 1)$ such that

$$(1 - \varepsilon)^3 > \delta(m - 1).$$

Moreover, suppose that

(i) There exist $L, \kappa > 0$ such that

$$\int_t^{t+L} v(\bar{\boldsymbol{s}}(\tau), \boldsymbol{w}(\tau), \theta) \langle \bar{\boldsymbol{s}}(\tau), \boldsymbol{w}(\tau) \rangle^2 > \kappa, \quad \forall\, t \geq t_0.$$

(ii) The firing threshold θ satisfies

$$0 < \theta < \frac{(1-\varepsilon)^3 - \delta(m-1)}{\sqrt{m(1-\varepsilon)[(1-\varepsilon)+\delta(m-1)]}}.$$

Then for, any $1-\theta > D > 0$, there is a $t_1(D) > t_0$ such that

$$\mathcal{P}([\mathcal{S}(\mathcal{Y}) \in \text{Activated}(\mathcal{S}, \boldsymbol{w}(t), \theta)] \;\&\; [\mathcal{S}(\mathcal{M}) \in \text{Silent}(\mathcal{S}, \boldsymbol{w}(t), \theta)]) \geq$$
$$(1-(1-\varepsilon)^n)^m \prod_{d=1}^{m-1} \left(1 - d\left(1-\delta^2\right)^{\frac{n}{2}}\right) \left[1 - \frac{1}{2}\left(1 - \frac{\theta^2}{(1+D)^2}\right)^{\frac{n}{2}}\right]^M$$

for all $t \geq t_1(D)$.

Proof of Theorem 6.3. According to Lemma 6.1, solutions $\boldsymbol{w}(t, \boldsymbol{w}_0)$ are defined for all $t \geq t_0$. Moreover, condition 1 of the theorem and Lemma 6.1 imply that

$$\lim_{t\to\infty} \boldsymbol{w}(t) = \bar{\boldsymbol{x}}/\|\bar{\boldsymbol{x}}\|. \tag{6.38}$$

Let $D > 0$ be chosen so that

$$0 < \frac{\theta}{1-D} < 1.$$

Given that $0 < \theta < 1$, such Ds always exist. Equation (6.38) implies that there is a $t_1(D) > t_0$ such that

$$\|\boldsymbol{w}(t) - \bar{\boldsymbol{x}}/\|\bar{\boldsymbol{x}}\|\| < D, \;\forall\; t \geq t_1(D).$$

The theorem now follows from Theorem 6.2 ■

Figure 6.8 illustrates the theorem numerically. In simulations illustrated with Figure 6.8A we assumed that the relevant set $\mathcal{Y}$ consists of $m = 2$ items. One of them (Fig. 6.8A, green) is considered as "known" to the neuron, i.e., its informational content, $\boldsymbol{x}_{M+1}$, satisfies $\langle \boldsymbol{w}_0, \boldsymbol{x}_{M+1}\rangle > \theta$ and hence generates a signal, $\langle \boldsymbol{w}_0, \boldsymbol{s}_{M+1}(t)\rangle$ that is above the firing threshold θ at some $t \geq t_0$. Consequently, the neuron detects this stimulus selectively as described in Section 6.4.1. For the second stimulus, however, we had $\langle \boldsymbol{w}_0, \boldsymbol{x}_{M+2}\rangle < \theta$. Therefore the neuron did not detect the stimulus $\boldsymbol{s}_{M+2}$ that is associated with the vector $\boldsymbol{x}_{M+2}$. The background stimuli from the set $\mathcal{S}(\mathcal{M})$ were also sub-threshold.

During learning phase, the neuron receives $M = 500$ and $m = 2$ relevant stimuli. Relevant stimuli from the set $\mathcal{S}(\mathcal{Y})$ appear simultaneously, i.e., they are temporarily associated. The learning phase results in changes in the synaptic efficiency. The membrane potential variable, $\langle \boldsymbol{w}(t), \bar{\boldsymbol{s}}(t)\rangle$ progressively increases when the relevant stimuli arrive. These neuronal adjustments give rise to new functionality. At some time instant (marked by red circle in Figure 6.8A) the neuron becomes responsive to the new relevant stimulus (Fig. 6.8A, yellow) which is synchronized with the "known" one. Note that all other background stimuli, which show

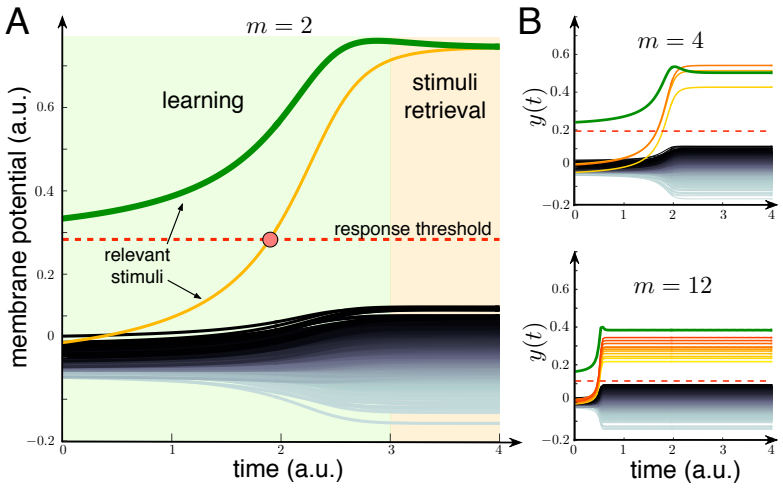

Figure 6.8: Dynamic memory: Learning new information items by association with previously learnt. **A)** Example of dynamic association of a known stimulus (green curve) and a new one (yellow curve). Two relevant stimuli out of 502 are learnt by the neuron. **B)** Same as in A but for $m = 4$ and $m = 12$. Parameter values: $\epsilon = 0{,}01$, $D = 0{,}001$, $\delta = (1-\epsilon)^3/2(m-1)$, $\alpha = 1$, $M = 500$, $\theta = \theta^* - D$, $n = 400$.

no temporal associativity, remain below the threshold (Fig. 6.8A, black traces). Thus, after a transient period, the neuron learns new stimulus. Once the learning is over, the neuron responds selectively to either of the two relevant stimuli.

The procedure described above applies to cases in which the number of relevant information items in the set $\mathcal{Y}$, m, is larger than 2 too. Figure 6.8B shows examples for $m = 4$ and $m = 12$. In both cases the neuron was able to learn all relevant stimuli, whilst rejecting all of the background stimuli. We observed, however, that increasing the value of m, i.e. the number of information items to be learnt, leads to decreases of viable firing thresholds at which the neuron exhibits the required selectivity and separation. In other words, the neuron does detect the assigned group of new stimuli, but with lower accuracy. This behavior is not surprising and is in accord with the bound on θ prescribed in the statement of Theorem 6.3.

6.5. Discussion

Theorems 6.1–6.3 and our numerical simulations demonstrate that the extreme stimulus selectivity to single and multiple stimuli, and capabilities to learn uncorrelated stimuli can be explained by relatively simple functional mechanisms implemented in single neurons. To achieve it we have used the following properties: i) the dimensionality n of the information content and neurons is sufficiently large, ii) a perceptron model, Eq. (6.9), as an adequate representation of neuronal response to stimuli, and iii) plasticity of the synaptic efficiency

governed by Hebbian rule (6.10). A crucial consequence of these results is that no *a priori* assumptions on the structural organization of neuronal ensembles are necessary for explaining basic concepts of static and dynamic memories.

Our approach, however, does not take into account more advanced neuronal behaviors provided by, e.g., models of spike-timing dependent plasticity [152] and firing threshold adaptation [164]. Nevertheless, our model captures essential properties of neuronal dynamics and as such is generic enough for the purpose of functional description of memories.

Firing threshold adaption, as reported in [164], steers firing activity of a stimulated neuron to a homeostatic state. In this state, the value of the threshold is just large/small enough to maintain reasonable firing rate without over/under-excitation. In our model, such a mechanism could be translated into keeping the value of θ sufficiently close to θ^* provided in Theorems 6.1 and 6.2.

In addition to rather general model of neuronal behavior, another major theoretical assumption of our approach was the presumption that stimuli informational content is drawn from an equidistribution in a unit ball $B_n(1)$. This assumption, however, can be lifted, and results of Theorems 6.1–6.3 generalized to product measures. Key ingredients of such generalizations are provided in [153], and practical feasibility is illustrated with Figures 6.6–6.8. In these figures we used information items randomly drawn from a hypercube.

Our theoretical and numerical analysis has revealed an interesting hierarchy of cognitive functionality implementable at the level of single neurons. We have shown that cognitive functionality develops with the dimensionality, or connectivity parameter n, in single neurons. This reveals explicit relationships between complexity of neural connectivity in living organisms with different cognitive behaviors such organisms can exhibit (cf. [73]).

As we can see from Theorems 6.1, 6.2 and Figures 6.6, 6.7, the ability of forming static memories increases monotonically with n. The increase of cognitive functionality, however, occurs in steps. Indeed, neuronal selectivity to a single stimulus is not at all visible at small n; it emerges rapidly when the dimension parameter n exceeds some critical value around $n = 10 - 20$ (see Figure 6.6A) for $M = 10^3$. This constitutes the first critical transition. The second critical transition occurs at significantly larger values, around $n = 100 - 400$ (see Figure 6.7). At this second stage the neuronal selectivity to multiple $uncorrelated$ stimuli develops. The ability to respond selectively to a given set of multiple uncorrelated information items is apparently crucial for rapid learning "by temporal association" in such neuronal systems. Such learning ability as well as formation of dynamic memories are justified by Theorem 6.3 and illustrated with Figure 6.8.

In the core of our mathematical arguments are measure concentration phenomena exemplified in [162] and stochastic separation theorems [153, 165]. Some of these results, that have been central in the proofs of Theorem 6.2 and 6.3, namely statements that random i.i.d. vectors from equidistributions in $B_n(1)$ and product measures are almost orthogonal with probability close to one, are closely related to notions of effective dimensionality of spaces based on ϵ-

$quasiorthogonality$ introduced in [166, 167]. In these works the authors demonstrated that in high dimensions there $exist$ exponentially large sets of quasiorthogonal vectors. In [162], however, as well as in our current work (see Lemma 6.2) we demonstrate that not only such sets exist, but also that they are typical in some sense.

Finally, note hat the number of multiple stimuli that can be selectively processed by single neurons is not extraordinarily large. In fact, as we have shown in Figures 6.7 and 6.8, memorizing 8 information items at the level of single neurons requires more than 400 connections. This suggests, that not only new memories are naturally packed $in\ quanta$, but also that there is a limit on this number that is associated with the cost of implementation of such functions. This cost is the number of individual functional synapses. Balancing the costs in living beings is of course a subject of selection and evolution. Nevertheless, as our current study have showed, there are clear functional gains which these costs may be paying for.

6.6. Conclusion

In this chapter we analyzed the dramatic consequences of the abundance of signalling routes for functionality of neural systems. We demonstrated that complex cognitive functionality related to extreme selectivity to stimulation, both single and multiple, and rapid learning of new memories at the level of single neurons can be explained by presence of multiple signalling routs and simple physiological mechanisms. These mechanisms are mere perceptron-like behavior of neurons in response to stimulation and a Hebbian-type learning rule governing changes of synaptic connections.

The phenomenon is robust; it emerges in simple generic models of neuronal activity. Remarkably, it offers simple mathematical explanation of a wealth of empirical evidence related to in-vivo reporting of grandmother cells, concept cells, and rapid learning at the level of individual neurons [145, 146, 147]. Finding simple laws explaining complex behaviours has always been the driver of progress in mathematical biology and neuroscience. Examples of such simple laws include but are not limited to [168, 169, 170].

Our results not only provide an explanation of the reported empirical evidence but also show that such behavior is expected in systems where stimuli informational content is inherently high-dimensional. In such systems, complex cognitive functionality at the level of elementary units, i.e. single neurons, occurs naturally. The higher the dimensionality, the stronger the effect. In particular, we have shown that the memory capacity in ensembles of single neurons grows exponentially with dimension. Hence, from evolutionary point of view, accommodating large number of signalling routes converging to single neurons is advantageous despite the increased metabolic costs.

The considered class of neuronal models, being generic, is of course a simplification. It does not capture spontaneous firing, signal propagation in neuronal dentritic trees, and

other complicated physiologically relevant features of real neuronal cells. Moreover, we have assumed that stimuli informational content is sampled from an equidistribution in a unit ball. The results, however, can already be generalized to product measure distributions, using e.g. [153]. Generalizing the findings to models that offer better physiological realism is the focus of our future work.

Conclusions

Throughout this thesis we have presented, analyzed and artificially implemented some novel models capable of explaining in mathematical terms different paramount cognitive processes observed in the brain of humans and mammals. Let us recall the structure of this work. On balance, Chapters 1 and 2 has been devoted to the study of the cognitive mechanisms behind the imitation learning processes, while Chapters 3, 4 and 5 provide a mathematical description of the cognitive abilities exhibited by cognitive agents to autonomously cope with dynamic situations.

Chapter 1 proposes a model for learning heteroclinic circuits in networks of neural networks. The model considers a learning relationship between two decoupled network motifs, playing roles of teacher and learner. The information transfer is implemented through a learning rule that changes local couplings in the learner according to the dynamics of the teacher. We have shown that under appropriate training a set of learner motifs arranged in a chain can progressively "copy" the connectivity pattern of the teacher network motif, by only observing its states and tuning itself to replicate the exhibited behavior. The time interval required for pattern replication grows linearly with the chain size. Thus, the learning process does not blow up and at the end we observe phase synchronized oscillations along the whole chain of network motifs.

This mathematical perspective of the imitation learning paradigm, addressed as a process of synchronization between neural networks, has been tackled in more depth in Chapter 2. Here three important theorems have been formulated and proved: Theorem 2.1 introduces a novel learning rule and postulates its exponentially fast convergence independently on the initial conditions. The new model supposes a generalization of the one initially proposed. It also aims at learning the correct order of the different motifs comprising the teacher's behavior. Theorem 2.2 presents a rigorous approach that enables the learner network to auto-rewire "on the fly", through an iterative process that requires, as Theorem 2.3 proves, less iterations than the number of motifs to be learnt. To validate the generalized model we have designed, based on these results, an algorithm that has been tested on mobile robots playing roles of teacher and learner. The teacher is programmed to reproduce a complex trajectory, while the learner is set at random. Then the learner starts to learn the teacher's trajectory. At the beginning its movements are quite chaotic. However, after few cycles the learner successfully

copies the teacher's behavior.

Regarding the second part of the thesis, in Chapter 3 we have discussed how to generalize the widely known concept of cognitive map upon dynamic situations. Thanks to the process of Prediction-for-CompAction, a time-changing situation can be represented as a static structure similar to a classical map. Mathematically, to generate this so-called Generalized Cognitive Map, or GCM, a neural architecture consisting of two coupled neural networks has been introduced. First, a recurrent neural network predicts future positions of the objects that could disrupt the agent's path. These data are mapped into the second 2D neuronal lattice that simulates what will happen if the agent takes this or that trajectory. Finally, a wavefront propagating over the lattice collides with objects provided by the first network and forms a static potential field surrounding "islands". This effective islands represent the spatial coincidences between agent and objects. Thus, knowing their location enables navigation avoiding collisions both with moving or static obstacles.

The main drawback of the wave-dynamic method proposed to building GCMs is its relatively high computational load, which stems from the modeling of a rather large 2D neural network. In order to achieve a real-time performance of the proposed model that allows the implementation of GCMs in real robots, Chapter 4 presents a model of totalistic isotropic Cellular Automata (CA) that enables the simulation of the process of wave propagation in 2D media. For correct interaction of waves with objects we introduced secondary wave sources in accordance with the Huygens' principle. Numerical simulations have confirmed that indeed the proposed CA enables fast and correct modeling of the process of propagation of waves in isotropic media with complex spatial configurations. Besides, due to its minimalistic nature, the proposed model is computationally efficient and permits relatively simple hardware implementation on a chip, which may further increase the calculation speed and hence be used for real-time tasks. To illustrate this ability we implemented the model on an onboard computer of a wheeled robot. The CA was used to build GCMs. On the onboard computer this process lasted around 300 ms, independently on the complexity of the environment. This delay falls within the time scale of human reaction, which allows the robot to react promptly to unexpected changes in the environment.

Chapter 5 shows how the concept of GCM, developed for rigid agents, can be extended to manipulators with two and three degrees of freedom. The approach consists in two steps: first we transform the problem from the workspace to the so-called handspace, and then we construct the appropriate GCM in this specific version of configuration space. The first step enables reduction of the whole limb to a point in the handspace. At the same time obstacles are transformed into spatially extended objects of complex exotic shapes. As in the case of navigation, GCMs in the handspace guarantee collision-free movement of the limb in the workspace. Besides, in order to demonstrate the feasibility of the proposed approach we have developed a 3D avatar of a humanoid robot. Our experiments have shown that indeed the robot can operate with moving objects in the presence of obstacles.

Finally, Chapter 6 proposes a mathematical tool for the encoding of memories by singles neurons. It consists on a canonical simple model, the well-known perceptron, combinated with a Hebbian-type learning rule governing changes of synaptic connections. Three significant theorems demonstrate that individual neurons gathering multidimensional stimuli through a sufficiently large number of synaptic entries can exhibit extreme selectivity either to individual information items or to groups of items. Our simulations show that neurons following this model are capable of associating and learning uncorrelated information items. A crucial consequence of our results is that no a priori assumptions on the structural organization of neuronal ensembles are necessary for explaining basic concepts of static and dynamic memories.

The researh carried out throughout the development of this thesis has been collected and disseminated in the following list of articles and conferences:

Publications in peer-reviewed journals:

1. Villacorta-Atienza JA, **Calvo C**, and Makarov VA. *Prediction-for-CompAction: Navigation in social environments using generalized cognitive maps*. Biological Cybernetics 109(3) 307-320, 2015

2. Makarov VA, **Calvo C**, Gallego V, and Selskii A. *Synchronization of heteroclinic circuits through learning in chains of neural motifs*. IFAC-PapersOnLine 49(14) 80-83, 2016

3. **Calvo C**, Gallego V, Selskii A, and Makarov VA. *Learning connectivity structure in a chain of network motifs*. Advanced Science Letters 22(10) 2647-2651, 2016

4. **Calvo C**, Villacorta-Atienza JA, Mironov VI, Gallego V, and Makarov VA. *Waves in isotropic totalistic cellular automata: Application to real-time robot navigation*. Advances in Complex Systems 19(4) 1650012-18, 2016

5. Villacorta-Atienza JA, **Calvo C**, Lobov S, and Makarov VA. *Limb movement in dynamic situations based on Generalized Cognitive Maps*. Mathematical Modelling of Natural Phenomena 12(4) 15-29, 2017

6. **Calvo C**, Kastalskiy I, Villacorta-Atienza JA, Khoruzhko M, and Makarov VA. *Holistic model of cognitive limbs for dynamic situations*. Proceedings of the 5th International Congress on Neurotechnology, Electronics and Informatics – NEUROTECHNIX 1 60-67, 2017

7. Tyukin IY, Gorban AN, **Calvo C**, Makarova J, and Makarov VA. *High-dimensional brain. A tool for encoding and rapid learning of memories by single neurons*. Bulletin of Mathematical Biology https://doi.org/10.1007/s11538-018-0415-5, 2018

8. **Calvo Tapia C**, Tyukin IY, and Makarov VA. *Fast social-like learning of complex behaviors based on motor motifs*. Physical Review E 97(5) 052308, 2018

9. **Calvo Tapia C**, Villacorta-Atienza JA, Kastalskiy I, Diez-Hermano S, Sanchez-Jimenez A, and Makarov VA. *Cognitive neural network driving DoF-scalable limbs in time-evolving situations*. Neural Networks (IJCNN), 2018 International Joint Conference on. IEEE 1-7, 2018

10. Villacorta-Atienza JA, **Calvo Tapia C**, Diez-Hermano S, Sanchez-Jimenez A, Lobov S, Krilova N, Murciano A, Lopez-Tolsa G, Pellon R, and Makarov VA. *Static internal representation of dynamic situations reveals time compaction in human cognition*. arXiv preprint arXiv:1806.10428, 2018

11. **Calvo Tapia C**, Makarov VA, and van Leeuwen C. *Basic principles drive self-organization of brain-like connectivity structure*. Communications in Nonlinear Science and Numerical Simulation (under review), 2019

12. **Calvo Tapia C**, Tyukin IY, and Makarov VA. *Universal principles justify the existence of concept cells*. Scientific Reports (submitted), 2019

International congresses:

1. Villacorta-Atienza JA, **Calvo C**, Gallego V, and Makarov VA. *Generalized cognitive maps for social navigation in cooperative and non-cooperative environments*. euRobotics Brokerage Day. Brussels Expo, Brussels, Belgium, 2015

2. **Calvo C**, Villacorta-Atienza JA, Gallego V, and Makarov VA. *Generalized cognitive maps for social navigation in cooperative and non-cooperative environments*. 2nd International Conference on Mathematical Neuroscience. Palais des Congrès, Juan les Pins, Antibes, France, 2016

3. **Calvo C**, Kastalskiy I, Villacorta-Atienza JA, Khoruzhko M, and Makarov VA. *Holistic model of cognitive limbs for dynamic situations*. 5th International Congress on Neurotechnology, Electronics and Informatics. Vila Galé Santa Cruz, Funchal, Madeira, Portugal, 2017

4. **Calvo Tapia C**, Tyukin IY, and Makarov VA. *Fast learning of complex behaviors from demonstration in neural networks*. Volga Neuroscience Meeting 2018. Nizhny Novgorod - Samara - Nizhny Novgorod, Russia, 2018

5. **Calvo Tapia C**, Tyukin IY, and Makarov VA. *Fast social-like learning of complex behaviors in neural networks*. International Congress on Industrial and Applied Mathematics. Valencia, Spain, 2019

Divulgation:

1. Makarov VA, **Calvo C**, Villacorta-Atienza JA, and Velarde MG. *El GPS dinámico del cerebro nos acerca al diseño de robots inteligentes*. Red.escubre 43 5-8, 2015

2. **Calvo C**. *Navegación cognitiva en robot Pioner 3DX: percepción, decisión y ejecución motora*. Cursos de verano Complutense - Matemáticas para el mundo y para la sociedad. San Lorenzo de El Escorial, Madrid, Spain, 2016

3. Villacorta-Atienza JA, **Calvo C**, and Makarov VA. *¿Es la biomimética el futuro de la robótica?* Boletín del Colegio Oficial de Doctores y Licenciados en Filosofía y Letras y en Ciencias 264 17-18, 2016

4. **Calvo Tapia C**. *Aprendizaje por imitación*. Seminarios de la Red de Doctorandos en Matemáticas UCM. Madrid, Spain, 2018

5. **Calvo Tapia C**. *Matemáticas hacia un robot inteligente*. Escuela de Doctorado UCM - PhDay Complutense. Madrid, Spain, 2019

6. **Calvo Tapia C**. *El cerebro de alta dimensión: modelos matemáticos de procesos cognitivos*. Colegio Oficial de Doctores y Licenciados en Filosofía y Letras y en Ciencias de la Comunidad de Madrid - Universidad de Otoño 2019. Madrid, Spain, 2019

Bibliography

[1] R. R. Llinás. *I of the Vortex: From Neurons to Self*. MIT Press, 2001.

[2] S. M. Reader. Animal social learning: Associations and adaptations. *F1000Research*, 5, 2016.

[3] M. D. Suboski and J. J. Templeton. Life skills training for hatchery fish: Social learning and survival. *Fisheries Research*, 7(4):343–352, 1989.

[4] A. Thornton and K. McAuliffe. Teaching in wild meerkats. *Science*, 313(5784):227–229, 2006.

[5] B. G. Galef and K. N. Laland. Social learning in animals: Empirical studies and theoretical models. *Bioscience*, 55(6):489–499, 2005.

[6] S. Lew-Levy, R. Reckin, N. Lavi, J. Cristóbal-Azkarate, and K. Ellis-Davies. How do hunter-gatherer children learn subsistence skills? *Human Nature*, 28(4):367–394, 2017.

[7] J. Villacorta-Atienza, M. Velarde, and V. Makarov. Compact internal representation of dynamic situations: Neural network implementing the causality principle. *Biological Cybernetics*, 103(4):285–297, 2010.

[8] V. A. Makarov and J. A. Villacorta-Atienza. Compact internal representation as a functional basis for protocognitive exploration of dynamic environments. *Recurrent Neural Networks for Temporal Data Processing*, pages 81–102, 2011.

[9] J. A. Villacorta-Atienza and V. A. Makarov. Neural network architecture for cognitive navigation in dynamic environments. *IEEE Transactions on Neural Networks and Learning Systems*, 24(12):2075–2087, 2013.

[10] J. A. Villacorta-Atienza and V. A. Makarov. Neuronal chains as processing units of long scale wave information. *BMC Neuroscience*, 14(1):P256, 2013.

[11] L. M. Hopper. Deferred imitation in children and apes. *Psychologist*, 23(4):294–297, 2010.

[12] A. Billard and D. Grollman. Robot learning by demonstration. *Scholarpedia*, 8(12):3824, 2013.

[13] C. L. Nehaniv and K. Dautenhahn. Like me? - Measures of correspondence and imitation. *Cybernetics & Systems*, 32(1-2):11–51, 2001.

[14] M. Rabinovich, A. Volkovskii, P. Lecanda, R. Huerta, H. Abarbanel, and G. Laurent. Dynamical encoding by networks of competing neuron groups: Winnerless competition. *Physical Review Letters*, 87(6):068102, 2001.

[15] A. Selskii and V. Makarov. Synchronization of heteroclinic circuits through learning in coupled neural networks. *Regular and Chaotic Dynamics*, 21(1):97–106, 2016.

[16] M. A. Cohen and S. Grossberg. Absolute stability of global pattern formation and parallel memory storage by competitive neural networks. *IEEE Transactions on Systems, Man, and Cybernetics*, 13(5):815–826, 1983.

[17] P. Varona, M. Rabinovich, A. Selverston, and Y. Arshavsky. Winnerless competition between sensory neurons generates chaos: A possible mechanism for molluscan hunting behavior. *Chaos*, 12(3):672–677, 2002.

[18] M. Moussaïd, D. Helbing, and G. Theraulaz. How simple rules determine pedestrian behavior and crowd disasters. *Proceedings of the National Academy of Sciences*, 108(17):6884–6888, 2011.

[19] B. Schmidt and A. D. Redish. Neuroscience: Navigation with a cognitive map. *Nature*, 497(7447):42, 2013.

[20] M. O. Franz and H. A. Mallot. Biomimetic robot navigation. *Robotics and Autonomous Systems*, 30(1-2):133–153, 2000.

[21] R. Sternberg. *Cognitive Psychology*. Cengage Learning, 2008.

[22] V. Gallese and A. Goldman. Mirror neurons and the simulation theory of mind-reading. *Trends in Cognitive Sciences*, 2(12):493–501, 1998.

[23] R. Cook, G. Bird, C. Catmur, C. Press, and C. Heyes. Mirror neurons: From origin to function. *Behavioral and Brain Sciences*, 37(2):177–192, 2014.

[24] G. Rizzolatti and M. Fabbri-Destro. Mirror neurons. *Scholarpedia*, 3(1):2055, 2008.

[25] G. Rizzolatti and L. Craighero. The mirror-neuron system. *Annual Review of Neuroscience*, 27:169–192, 2004.

[26] M. Iacoboni, R. P. Woods, M. Brass, H. Bekkering, J. C. Mazziotta, and G. Rizzolatti. Cortical mechanisms of human imitation. *Science*, 286(5449):2526–2528, 1999.

[27] G. Buccino, S. Vogt, A. Ritzl, G. R. Fink, K. Zilles, H. J. Freund, and G. Rizzolatti. Neural circuits underlying imitation learning of hand actions: An event-related fMRI study. *Neuron*, 42(2):323–334, 2004.

[28] R. G. Morris, P. Garrud, J. a. Rawlins, and J. O'Keefe. Place navigation impaired in rats with hippocampal lesions. *Nature*, 297(5868):681, 1982.

[29] D. Klement, E. Pašťalková, and A. A. Fenton. Tetrodotoxin infusions into the dorsal hippocampus block non-locomotor place recognition. *Hippocampus*, 15(4):460–471, 2005.

[30] D. Levcik, T. Nekovarova, A. Stuchlik, and D. Klement. Rats use hippocampus to recognize positions of objects located in an inaccessible space. *Hippocampus*, 23(2):153–161, 2013.

[31] E. C. Tolman. Cognitive maps in rats and men. *Psychological Review*, 55(4):189, 1948.

[32] J. O'Keefe and J. Dostrovsky. The hippocampus as a spatial map: Preliminary evidence from unit activity in the freely-moving rat. *Brain Research*, 1971.

[33] T. Danjo, T. Toyoizumi, and S. Fujisawa. Spatial representations of self and other in the hippocampus. *Science*, 359(6372):213–218, 2018.

[34] D. B. Omer, S. R. Maimon, L. Las, and N. Ulanovsky. Social place-cells in the bat hippocampus. *Science*, 359(6372):218–224, 2018.

[35] Ø. A. Høydal, E. R. Skytøen, S. O. Andersson, M. B. Moser, and E. I. Moser. Object-vector coding in the medial entorhinal cortex. *Nature*, 568(7752):400, 2019.

[36] T. J. Davidson, F. Kloosterman, and M. A. Wilson. Hippocampal replay of extended experience. *Neuron*, 63(4):497–507, 2009.

[37] J. O'Keefe and L. Nadel. *The Hippocampus as a Cognitive Map*. Oxford: Clarendon Press, 1978.

[38] J. A. Villacorta-Atienza, C. Calvo Tapia, S. Diez-Hermano, A. Sanchez-Jimenez, S. Lobov, N. Krilova, A. Murciano, G. Lopez-Tolsa, R. Pellon, and V. Makarov. Static internal representation of dynamic situations reveals time compaction in human cognition. *arXiv preprint arXiv:1806.10428*, 2018.

[39] R. Milo, S. Shen-Orr, S. Itzkovitz, N. Kashtan, D. Chklovskii, and A. U. Network motifs: Simple building blocks of complex networks. *Science*, 298(5594):824–827, 2002.

[40] U. Alon. Network motifs: Theory and experimental approaches. *Nature Reviews Genetics*, 8(6):450–461, 2007.

[41] O. Sporns and R. Kötter. Motifs in brain networks. *PLoS Biology*, 2(11):e369, 2004.

[42] X. Hong-Lin, Y. Han-Bing, G. Cui-Fang, and Z. Ping. Social network analysis based on network motifs. *Journal of Applied Mathematics*, 2014, 2014.

[43] S. Wernicke. Efficient detection of network motifs. *IEEE/ACM Transactions on Computational Biology and Bioinformatics (TCBB)*, 3(4):347–359, 2006.

[44] P. Ribeiro and F. Silva. G-tries: An efficient data structure for discovering network motifs. In *Proceedings of the 2010 ACM Symposium on Applied Computing*, pages 1559–1566, 2010.

[45] C. Calvo, V. Gallego, A. Selskii, and V. Makarov. Learning connectivity structure in a chain of network motifs. *Advanced Science Letters*, 22(10):2647–2651, 2016.

[46] V. Makarov, C. Calvo, V. Gallego, and A. Selskii. Synchronization of heteroclinic circuits through learning in chains of neural motifs. *IFAC-PapersOnLine*, 49(14):80–83, 2016.

[47] I. Lodato, S. Boccaletti, and V. Latora. Synchronization properties of network motifs. *EPL (Europhysics Letters)*, 78(2):28001, 2007.

[48] A. Shilnikov, R. Gordon, and I. Belykh. Polyrhythmic synchronization in bursting networking motifs. *Chaos*, 18(3), 2008.

[49] H. Abarbanel, M. Rabinovich, A. Selverstone, M. Bazhenov, R. Huerta, M. Sushchik, and L. Rubchinskii. Synchronization in neural networks. *Physics-Uspekhi*, 135(4):337–362, 1996.

[50] P. Ashwin and P. Chossat. Attractors for robust heteroclinic cycles with continua of connections. *Journal of Nonlinear Science*, 8(2):103–129, 1998.

[51] P. Ashwin and M. Field. Heteroclinic network in coupled cell systems. *Archive for Rational Mechanics and Analysis*, 148(2):107–143, 1999.

[52] V. Afraimovich, M. Rabinovich, and P. Varona. Heteroclinic contours in neural ensembles and the winnerless competition principle. *International Journal of Bifurcation and Chaos*, 14(4):1195–1208, 2004.

[53] V. Makarov, Y. Song, M. Velarde, D. Hubner, and H. Cruse. Elements for a general memory structure: Properties of recurrent neural networks used to form situation models. *Biological Cybernetics*, 98(5):371–395, 2008.

[54] J. Villacorta-Atienza and V. Makarov. Neural network architecture for cognitive navigation in dynamic environments. *IEEE Transactions on Neural Networks and Learning Systems*, 24(12):2075–2087, 2013.

[55] C. Calvo Tapia, I. Tyukin, and V. Makarov. Fast social-like learning of complex behaviors based on motor motifs. *Physical Review E*, 97(5):052308, 2018.

[56] W. Hoppitt and K. Laland. *Social Learning: An Introduction to Mechanisms, Methods, and Models*. Princeton University Press, 2013.

[57] S. Schaal. Is imitation learning the route to humanoid robots? *Trends in Cognitive Sciences*, 3(6):233–242, 1999.

[58] C. Breazeal, D. Buchsbaum, J. Gray, D. Gatenby, and B. Blumberg. Learning from and about others: Towards using imitation to bootstrap the social understanding of others by robots. *Artificial Life*, 11(1-2):31–62, 2005.

[59] E. Broadbent, R. Stafford, and B. MacDonald. Acceptance of healthcare robots for the older population: Review and future directions. *International Journal of Social Robotics*, 1(4):319, 2009.

[60] F. Stulp, E. Oztop, P. Pastor, M. Beetz, and S. Schaal. Compact models of motor primitive variations for predictable reaching and obstacle avoidance. In *Humanoid Robots. Humanoids 2009. 9th IEEE-RAS International Conference on*, pages 589–595, 2009.

[61] A. Colome and C. Torras. Dimensionality reduction and motion coordination in learning trajectories with dynamic movement primitives. In *Intelligent Robots and Systems (IROS 2014), 2014 IEEE/RSJ International Conference on*, pages 1414–1420, 2014.

[62] F. Meier, E. Theodorou, F. Stulp, and S. Schaal. Movement segmentation using a primitive library. In *Intelligent Robots and Systems (IROS). IEEE/RSJ International Conference on*, pages 3407–3412, 2011.

[63] J. Villacorta-Atienza, C. Calvo, S. Lobov, and V. Makarov. Limb movement in dynamic situations based on generalized cognitive maps. *Mathematical Modelling of Natural Phenomena*, 12(15), 2017.

[64] S. Schaal, P. Mohajerian, and A. Ijspeert. Dynamics systems vs. optimal control - a unifying view. *Progress in Brain Research*, 165:425–445, 2007.

[65] T. Matsubara, S. Hyon, and J. Morimoto. Learning parametric dynamic movement primitives from multiple demonstrations. *Neural Networks*, 24(5):493–500, 2011.

[66] Y. Tassa, T. Erez, and E. Todorov. Synthesis and stabilization of complex behaviors through online trajectory optimization. In *Intelligent Robots and Systems (IROS). IEEE/RSJ International Conference on*, pages 4906–4913, 2012.

[67] A. Ansari and T. Murphey. Sequential action control: Closed-form optimal control for nonlinear and nonsmooth systems. *IEEE Transactions on Robotics*, 32(5):1196–1214, 2016.

[68] N. Benito, G. Martin-Vazquez, J. Makarova, V. Makarov, and O. Herreras. The right hippocampus leads the bilateral integration of gamma-parsed lateralized information. *eLife*, 5:e16658, 2016.

[69] G. Martin-Vazquez, N. Benito, V. Makarov, O. Herreras, and J. Makarova. Diversity of LFPs activated in different target regions by a common CA3 input. *Cerebral Cortex*, 26(3):4082–4100, 2016.

[70] H. Sompolinsky and I. Kanter. Temporal association in asymmetric neural networks. *Physical Review Letters*, 77(22):2861–2864, 1986.

[71] I. Tyukin, A. Gorban, C. Calvo, J. Makarova, and V. Makarov. High-dimensional brain. A tool for encoding and rapid learning of memories by single neurons. *Bulletin of Mathematical Biology*, (in press), 2018.

[72] E. del Rio, V. Makarov, M. Velarde, and W. Ebeling. Mode transitions and wave propagation in a driven-dissipative toda-rayleigh ring. *Physical Review E*, 67(5):056208–056217, 2003.

[73] S. Lobov, M. Zhuravlev, V. Makarov, and V. Kazantsev. Noise enhanced signaling in STDP driven spiking-neuron network. *Mathematical Modelling of Natural Phenomena*, 12(4):109–124, 2017.

[74] V. Afraimovich, V. Zhigulin, and M. Rabinovich. On the origin of reproducible sequential activity in neural circuits. *Chaos*, 14:1123, 2004.

[75] F. Hadaeghi, M. Reza, H. Golpayegani, and G. Murray. Towards a complex system understanding of bipolar disorder: A map based model of a complex winnerless competition. *Journal of Theoretical Biology*, 376:74–81, 2015.

[76] T. Rost, M. Deger, and M. Nawrot. Winnerless competition in clustered balanced networks: Inhibitory assemblies do the trick. *Biological Cybernetics*, 112(1-2):81–98, 2017.

[77] C. Calvo, J. Villacorta-Atienza, V. Mironov, V. Gallego, and V. Makarov. Waves in isotropic totalistic cellular automata: Application to real-time robot navigation. *Advances in Complex Systems*, 19(4):1650012–18, 2016.

[78] I. Tyukin, D. Prokhorov, and C. van Leeuwen. Adaptation and parameter estimation in systems with unstable target dynamics and nonlinear parametrization. *IEEE Transactions on Automatic Control*, 52(9):1543–1559, 2007.

[79] I. Tyukin. *Adaptation in Dynamical Systems*. Cambridge University Press, 2011.

[80] A. Hramov, A. Koronovskii, V. Makarov, A. Pavlov, and E. Sitnikova. *Wavelets in Neuroscience*. Springer, 2015.

[81] J. Villacorta-Atienza, C. Calvo, and V. Makarov. Prediction-for-CompAction: Navigation in social environments using generalized cognitive maps. *Biological Cybernetics*, 109(3):307–320, 2015.

[82] D. Park, H. Hoffmann, P. Pastor, and S. Schaal. Movement reproduction and obstacle avoidance with dynamic movement primitives and potential fields. In *Humanoid Robots. Humanoids 2008 - 8th IEEE-RAS International Conference on*, pages 91–98, 2008.

[83] B. Schmidt and A. Redish. Navigation with a cognitive map. *Nature*, 497(7447):42–43, 2013.

[84] B. E. Pfeiffer and D. J. Foster. Hippocampal place-cell sequences depict future paths to remembered goals. *Nature*, 497(7447):74, 2013.

[85] J. A. Meyer and D. Filliat. Map-based navigation in mobile robots:: II. A review of map-learning and path-planning strategies. *Cognitive Systems Research*, 4(4):283–317, 2003.

[86] S. Ho, E. Hori, T. Kobayashi, K. Umeno, A. Tran, T. Ono, and H. Nishijo. Hippocampal place cell activity during chasing of a moving object associated with reward in rats. *Neuroscience*, 157(1):254–270, 2008.

[87] P. Telensky, J. Svoboda, K. Blahna, J. Bureš, S. Kubik, and A. Stuchlik. Functional inactivation of the rat hippocampus disrupts avoidance of a moving object. *Proceedings of the National Academy of Sciences*, 108(13):5414–5418, 2011.

[88] E. T. Hall. A system for the notation of proxemic behavior. *American anthropologist*, 65(5):1003–1026, 1963.

[89] T. Lozano-Pérez and M. A. Wesley. An algorithm for planning collision-free paths among polyhedral obstacles. *Communications of the ACM*, 22(10):560–570, 1979.

[90] M. Kuderer, H. Kretzschmar, C. Sprunk, and W. Burgard. Feature-based prediction of trajectories for socially compliant navigation. In *Robotics: Science and Systems*, 2012.

[91] E. I. Moser, E. Kropff, and M. B. Moser. Place cells, grid cells, and the brain's spatial representation system. *Annual Review of Neuroscience*, 31:69–89, 2008.

[92] C. R. Boldea. A particle cellular automata model for fluid simulations. *Annals of the University of Craiova, Mathematics and Computer Science Series*, 36(2):35–41, 2009.

[93] I. Karafyllidis and A. Thanailakis. Simulation of two-dimensional photoresist etching process in integrated circuit fabrication using cellular automata. *Modelling and Simulation in Materials Science and Engineering*, 3(5):629, 1995.

[94] Q. A. Huang, Z. F. Zhou, W. H. Li, and D. W. Xu. A modified cellular automata algorithm for the simulation of boundary advancement in deposition topography simulation. *Journal of Micromechanics and Microengineering*, 16(1):1, 2005.

[95] K. Reuther and M. Rettenmayr. Perspectives for cellular automata for the simulation of dendritic solidification – A review. *Computational Materials Science*, 95:213–220, 2014.

[96] A. Nishiyama, T. Tokihiro, M. Badoual, and B. Grammaticos. Modelling the morphology of migrating bacterial colonies. *Physica D: Nonlinear Phenomena*, 239(16):1573–1580, 2010.

[97] P. Singhal and H. Kundra. A review paper of navigation and path-finding using mobile cellular automata. *International Journal of Advances in Computer Science and Communication Engineering (IJACSCE)*, 2, 2014.

[98] M. Markus and B. Hess. Isotropic cellular automaton for modelling excitable media. *Nature*, 347(6288):56, 1990.

[99] I. French, D. Anderson, and E. Catchpole. Graphical simulation of bushfire spread. *Mathematical and Computer Modelling*, 13(12):67–71, 1990.

[100] I. Karafyllidis and A. Thanailakis. A model for predicting forest fire spreading using cellular automata. *Ecological Modelling*, 99:87–97, 1997.

[101] M. Delorme, J. Mazoyer, and L. Tougne. Discrete parabolas and circles on 2D cellular automata. *Theoretical Computer Science*, 218(2):347, 1999.

[102] M. Marek. Grid anisotropy reduction for simulation of growth processes with cellular automaton. *Physica D: Nonlinear Phenomena*, 253:73–84, 2013.

[103] G. C. Sirakoulis, I. Karafyllidis, and A. Thanailakis. A cellular automaton for the propagation of circular fronts and its applications. *Engineering Applications of Artificial Intelligence*, 18(6):731–744, 2005.

[104] M. Kobayashi. Isotropic cellular automaton for excitable media with random neighbor selection. In *International Conference on Cellular Automata*, pages 35–44. Springer, 2014.

[105] G. M. Ortigoza. Unstructured triangular cellular automata for modeling geographic spread. *Applied Mathematics and Computation*, 258:520–536, 2015.

[106] C. Behring, M. Bracho, M. Castro, and J. Moreno. An algorithm for robot path planning with cellular automata. In *Theory and Practical Issues on Cellular Automata*, pages 11–19. Springer, 2001.

[107] R. Al-Hmouz, T. Gulrez, and A. Al-Jumaily. Cellular automata based path planning algorithm for autonomous mobile robots. In *Proceedings of the 16th IFAC World Congress*, 2005.

[108] K. Charalampous, A. Amanatiadis, and A. Gasteratos. Efficient robot path planning in the presence of dynamically expanding obstacles. In *International Conference on Cellular Automata*, pages 330–339. Springer, 2012.

[109] Y. P. Gunji, T. Shirakawa, T. Niizato, M. Yamachiyo, and I. Tani. An adaptive and robust biological network based on the vacant-particle transportation model. *Journal of Theoretical Biology*, 272(1):187–200, 2011.

[110] U. A. Syed and F. Kunwar. Cellular automata based real-time path-planning for mobile robots. *International Journal of Advanced Robotic Systems*, 11(7):93, 2014.

[111] Y. Tavakoli, H. H. S. Javadi, and S. Adabi. A cellular automata based algorithm for path planning in multi-agent systems with a common goal. *International Journal of Computer Science and Network Security*, 8(7):119–123, 2008.

[112] H. Qu, S. X. Yang, A. R. Willms, and Z. Yi. Real-time robot path planning based on a modified pulse-coupled neural network model. *IEEE Transactions on Neural Networks*, 20(11):1724–1739, 2009.

[113] T. Fong, I. Nourbakhsh, and K. Dautenhahn. A survey of socially interactive robots. *Robotics and Autonomous Systems*, 42(3-4):143–166, 2003.

[114] M. Schilling, J. Paskarbeit, T. Hoinville, A. Hüffmeier, A. Schneider, J. Schmitz, and H. Cruse. A hexapod walker using a heterarchical architecture for action selection. *Frontiers in Computational Neuroscience*, 7:126, 2013.

[115] P. Petrov. Modeling and adaptive path control of a differential drive mobile robot. In *Proceedings of the 12th WSEAS International Conference on Automatic Control, Modelling & Simulation*, pages 403–408, 2010.

[116] D. E. Meyer, A. M. Osman, D. E. Irwin, and S. Yantis. Modern mental chronometry. *Biological Psychology*, 26(1-3):3–67, 1988.

[117] P. Progias and G. C. Sirakoulis. An FPGA processor for modelling wildfire spreading. *Mathematical and Computer Modelling*, 57(5-6):1436–1452, 2013.

[118] L. Salas-Paracuellos, L. Alba, J. A. Villacorta-Atienza, and V. A. Makarov. FPGA implementation of a modified FitzHugh-Nagumo neuron based causal neural network for compact internal representation of dynamic environments. In *Proceedings of SPIE – the International Society for Optical Engineering*, volume 8068, page 80680J, 2011.

[119] R. S. Campos, R. M. Amorim, B. L. de Oliveira, B. M. Rocha, J. Sundnes, L. P. da Silva Barra, M. Lobosco, and R. W. dos Santos. 3D heart modeling with cellular automata, mass-spring system and CUDA. In *International Conference on Parallel Computing Technologies*, pages 296–309. Springer, 2013.

[120] C. Calvo, I. Kastalskiy, J. Villacorta-Atienza, M. Khoruzhko, and V. Makarov. Holistic model of cognitive limbs for dynamic situations. In *Neurotechnology, Electronics and Informatics (NEUROTECHNIX 2017). 5th International Congress on*, pages 60–67, 2017.

[121] C. Calvo Tapia, J. Villacorta-Atienza, I. Kastalskiy, S. Diez-Hermano, A. Sánchez-Jiménez, and V. Makarov. Cognitive neural network driving DoF-scalable limbs in time-evolving situations. In *Neural Networks (IJCNN). IEEE 2018 International Joint Conference on*, pages 1–7, 2018.

[122] O. Khatib. Real-time obstacle avoidance for manipulators and mobile robots. *The International Journal of Robotics Research*, 5(1):90–98, 1986.

[123] L. Sentis and O. Khatib. Synthesis of whole-body behaviors through hierarchical control of behavioral primitives. *International Journal of Humanoid Robotics*, 2(04):505–518, 2005.

[124] D. Seredynsk, K. Banachowicz, and T. Winiarski. Graph-based potential field for the end-effector control within the torque-based task hierarchy. In *Methods and Models in Automation and Robotics (MMAR). 21st International Conference on*, pages 645–650, 2016.

[125] A. Ijspeert, J. Nakanishi, and S. Schaal. Learning attractor landscapes for learning motor primitives. In *Advances in Neural Information Processing Systems*, pages 1547–1554, 2003.

[126] H. Reimann, I. Iossifidis, and G. Schoner. Autonomous movement generation for manipulators with multiple simultaneous constraints using the attractor dynamics approach. In *Robotics and Automation (ICRA). IEEE International Conference on*, pages 5470–5477, 2011.

[127] S. Li, Y. Zhang, and L. Jin. Kinematic control of redundant manipulators using neural networks. *IEEE Transactions on Neural Networks and Learning Systems*, 28(10):2243–2254, 2017.

[128] H. Sadjadian, H. Taghirad, and A. Fatehi. Neural networks approaches for computing the forward kinematics of a redundant parallel manipulator. *International Journal of Computational Intelligence*, 2(1):40–47, 2005.

[129] H. Choset, S. Hutchinson, K. Lynch, G. Kantor, W. Burgard, L. Kavraki, and S. Thrun. *Principles of Robot Motion: Theory, Algorithms, and Implementation*. MIT Press, 2005.

[130] R. Patel and F. Shadpey. *Control of Redundant Robot Manipulators: Theory and Experiments*. Springer-Verlag Berlin Heidelberg, 2005.

[131] J. McIntyre, M. Zago, A. Berthoz, and F. Lacquaniti. Does the brain model Newton's laws? *Nature Neuroscience*, 4(7):693–694, 2001.

[132] P. Dean, J. Porrill, C. Ekerot, and H. Jorntell. The cerebellar microcircuit as an adaptive filter: Experimental and computational evidence. *Nature Reviews Neuroscience*, 11(1):30–43, 2010.

[133] M. F. Land. Do we have an internal model of the outside world? *Philosophical Transactions of the Royal Society B: Biological Sciences*, 369(1636):20130045, 2014.

[134] A. Terekhov and J. O'Regan. Space as an invention of active agents. *Frontiers in Robotics and AI*, 3:4, 2016.

[135] W. Noguchi, H. Iizuka, and M. Yamamoto. Cognitive map self-organization from subjective visuomotor experiences in a hierarchical recurrent neural network. *Adaptive Behavior*, 25(3):129–146, 2017.

[136] M. Spong, S. Hutchinson, and M. Vidyasagar. *Robot Modeling and Control*. Wiley, New York, 2006.

[137] S. Herculano-Houzel. The remarkable, yet not extraordinary, human brain as a scaled-up primate brain and its associated cost. *Proceedings of the National Academy of Sciences*, 109(Supplement 1):10661–10668, 2012.

[138] S. Herculano-Houzel and J. H. Kaas. Gorilla and orangutan brains conform to the primate cellular scaling rules: Implications for human evolution. *Brain, Behavior and Evolution*, 77(1):33–44, 2011.

[139] D. D. Clarke. Circulation and energy metabolism of the brain. *Basic Neurochemistry: Molecular, Cellular, and Medical Aspects*, 1999.

[140] S. Herculano-Houzel. The human brain in numbers: A linearly scaled-up primate brain. *Frontiers in Human Neuroscience*, 3:31, 2009.

[141] P. Andersen, R. Morris, D. Amaral, T. Bliss, and J. O'Keefe. *The Hippocampus Book*. Oxford University Press, 2006.

[142] M. Platek, J. Keenan, and T. K. Shackelford. *Evolutionary Cognitive Neuroscience*. MIT Press, 2007.

[143] C. C. Sherwood, A. L. Bauernfeind, S. Bianchi, M. A. Raghanti, and P. R. Hof. Human brain evolution writ large and small. In *Progress in Brain Research*, volume 195, pages 237–254. Elsevier, 2012.

[144] A. Sousa, K. Meyer, G. Santpere, F. Gulden, and N. Sestan. Evolution of the human nervous system function, structure, and development. *Cell*, 170(2):226–247, 2017.

[145] M. Ison, R. Quian Quiroga, and I. Fried. Rapid encoding of new memories by individual neurons in the human brain. *Neuron*, 87(1):220–230, 2015.

[146] R. Quian Quiroga, L. Reddy, G. Kreiman, C. Koch, and I. Fried. Invariant visual representation by single neurons in the human brain. *Nature*, 435(7045):1102–1107, 2005.

[147] I. V. Viskontas, R. Q. Quiroga, and I. Fried. Human medial temporal lobe neurons respond preferentially to personally relevant images. *Proceedings of the National Academy of Sciences*, 106(50):21329–21334, 2009.

[148] R. Quian Quiroga. Concept cells: The building blocks of declarative memory functions. *Nature Reviews Neuroscience*, 13(8):587–597, 2012.

[149] M. W. Reimann, M. Nolte, M. Scolamiero, K. Turner, R. Perin, G. Chindemi, P. Dłotko, R. Levi, K. Hess, and H. Markram. Cliques of neurons bound into cavities provide a missing link between structure and function. *Frontiers in Computational Neuroscience*, 11:48, 2017.

[150] F. Rosenblatt. *Principles of Neurodynamics: Perceptrons and the Theory of Brain Mechanisms*. Spartan Books, 1962.

[151] D. O. Hebb. *The Organization of Behavior: A Neuropsychological Theory*. Psychology Press, 2005.

[152] H. Markram, J. Lubke, M. Frotscher, and B. Sakmann. Regulation of synaptic efficacy by coincidence of postsynaptic APs and EPSPs. *Science*, 275(5297):213–215, 1997.

[153] A. Gorban and I. Tyukin. Stochastic separation theorems. *Neural Networks*, 94:255–259, 2017.

[154] D. Amaral and M. Witter. The three-dimensional organization of the hippocampal formation: A review of anatomical data. *Neuroscience*, 31:571–591, 1989.

[155] N. Ishizuka, J. Weber, and D. G. Amaral. Organization of intrahippocampal projections originating from CA3 pyramidal cells in the rat. *Journal of Comparative Neurology*, 295(4):580–623, 1990.

[156] L. Wittner, D. A. Henze, L. Záborszky, and G. Buzsáki. Three-dimensional reconstruction of the axon arbor of a CA3 pyramidal cell recorded and filled in vivo. *Brain Structure and Function*, 212(1):75–83, 2007.

[157] X.-G. Li, P. Somogyi, A. Ylinen, and G. Buzsáki. The hippocampal CA3 network: An in vivo intracellular labeling study. *Journal of Comparative Neurology*, 339(2):181–208, 1994.

[158] N. Benito, A. Fernandez-Ruiz, V. Makarov, J. Makarova, A. Korovaichuk, and O. Herreras. Spatial modules of coherent activity in pathway-specific LFPs in the hippocampus reflect topology and different modes of presynaptic synchronization. *Cerebral Cortex*, 11(7):1738–1752, 2014.

[159] C. Rnnerty and J. Jefferys. Functional connectivity from CA3 to the ipsilateral and contralateral CA1 in the rat dorsal hippocampus. *Neuroscience*, 56(1), 1993.

[160] A. Fernandez-Ruiz, V. Makarov, and O. Herreras. Sustained increase of spontaneous input and spike transfer in the CA3-CA1 pathway following long term potentiation in vivo. *Frontiers in Neural Circuits*, 6:71, 2012.

[161] E. Oja. A simplified neuron model as a principal component analyzer. *Journal of Mathematical Biology*, 15:267–273, 1982.

[162] A. Gorban, I. Tyukin, D. Prokhorov, and K. Sofeikov. Approximation with random bases: Pro et Contra. *Information Sciences*, 364–365:129–145, 2016.

[163] I. Y. Tyukin, A. N. Gorban, K. I. Sofeykov, and I. Romanenko. Knowledge transfer between artificial intelligence systems. *Frontiers in Neurorobotics*, 12, 2018.

[164] B. Fontaine, J. L. Peña, and R. Brette. Spike-threshold adaptation predicted by membrane potential dynamics in vivo. *PLoS Computational Biology*, 10(4):e1003560, 2014.

[165] A. N. Gorban, I. Y. Tyukin, and I. Romanenko. The blessing of dimensionality: Separation theorems in the thermodynamic limit. *IFAC-PapersOnLine*, 49(24):64–69, 2016.

[166] P. C. Kainen and V. Kurková. Quasiorthogonal dimension of Euclidean spaces. *Applied Mathematics Letters*, 6(3):7–10, 1993.

[167] R. Hecht-Nielsen. Context vectors: General purpose approximate meaning representations self-organized from raw data. *Computational Intelligence: Imitating Life*, 3(11):43–56, 1994.

[168] A. Roberts, D. Conte, M. Hull, R. Merrison-Hort, A. K. al Azad, E. Buhl, R. Borisyuk, and S. Soffe. Can simple rules control development of a pioneer vertebrate neuronal network generating behavior? *Journal of Neuroscience*, 34(2):608–621, 2014.

[169] P. Jurica, S. Gepshtein, I. Tyukin, and C. van Leeuwen. Sensory optimization by stochastic tuning. *Psychological Review*, 120(4):798–816, 2013.

[170] A. Gorban, T. Tyukina, E. Smirnova, and L. Pokidysheva. Evolution of adaptation mechanisms: Adaptation energy, stress, and oscillating death. *Journal of Theoretical Biology*, 405:127–139, 2016.